

Ultrasound-CT Registration in Image-Guided Pedicle Screw Placement

João Filipe Fernandes Mocho Ferreira

Thesis to obtain the Master of Science Degree in

Biomedical Engineering

Supervisors: Professor Jorge Manuel Mateus Martins

Dr. Manuel Herculano Carvalho

Examination Committee

Chairperson: Professor Maria Margarida Campos da Silveira

Supervisor: Professor Jorge Manuel Mateus Martins

Members of the Committee: Professor João Carlos Prata dos Reis

May 2019

Preface

The work presented in this thesis was performed at the Surgical Robotics Lab (SRL) of IDMEC, Instituto Superior Técnico (Lisbon, Portugal), during the period February 2018 - May 2019, under the supervision of Prof. Jorge Martins from IST and the co-supervision of Dr. Manuel Herculano from Hospital de Santa Maria.

Declaração

Declaro que o presente documento é um trabalho original da minha autoria e que cumpre todos os requisitos do Código de Conduta e Boas Práticas da Universidade de Lisboa.

Declaration

I declare that this document is an original work of my own authorship and that it fulfills all the requirements of the Code of Conduct and Good Practices of the Universidade de Lisboa.

Abstract

Pedicle screws placement is among the most performed procedures for treating chronic lower back pain and increasing the accuracy of their insertion is crucial. Image-guided surgery is one of the most advanced techniques for inserting pedicle screws in the lumbar spine, presenting better results than traditional approaches. Despite of this accuracy improvement, most image-guided procedures use ionizing radiation for acquiring intraoperative images, which led to studies aimed at substituting the intraoperative imaging by a low cost, real-time and non-ionizing alternative, such as ultrasound imaging.

The present project simulates all necessary steps for performing image-guided pedicle screw placement, using Free-hand 3-D Ultrasound as intraoperative imaging modality. For this, it was created a lumbar spine phantom, which was used as subject to perform a preoperative CT-scan, where segmentation and surgical planning was performed, and to acquire intraoperative US volumes, using an optical measurement system to track an US probe. The point clouds segmented from the CT and US data were then registered using an initial approximation based on fiducial identification and refined by the Iterative Closest Point algorithm, which allowed to compute transformation from the CT referential to the intraoperative coordinate system. A group of five US volumes were acquired from different regions of the phantom and were merged with the CT data, presenting a registration error around 2 mm . After combining the surgical plans and the registration results in a navigation system, it was concluded that, although presenting some limitations, ultrasound could be an alternative for intraoperative imaging in IG surgery.

Keywords: Lumbar Spine; Pedicle Screws; Phantom; Surgical Planning; Image-Guided Surgery; Intraoperative; Ultrasound; Point Cloud; Registration.

Resumo

A colocação de parafusos pediculares é um dos procedimentos mais realizados no tratamento de lombalgia crónica e é crucial aumentar a precisão da sua inserção. A cirurgia guiada por imagem é uma das técnicas mais avançadas para inserção de parafusos pediculares, apresentando melhores resultados que outras abordagens. Apesar dessa melhoria na precisão, a maioria dos procedimentos guiados por imagem utiliza radiação ionizante para adquirir imagens intraoperatórias, levando a estudos que as visam substituir por uma alternativa de imagem em tempo-real, baixo custo e não ionizante, como a ultrassonografia.

O presente projeto simula as etapas necessárias para a colocação de parafusos pediculares, utilizando aquisição manual de ultrassonografia tridimensional como imagem intraoperatória. Para isso, foi criado um fantoma de coluna lombar, que foi sujeito a uma TAC pré-operatória, onde foi realizada a segmentação e o planeamento cirúrgico, e à aquisição intra-operatória de volumes de ultrasons, utilizando um sistema de medição óptica para rastrear a sonda de ultrasons. As nuvens de pontos segmentadas das imagens pré e intra-operatórias foram registadas usando uma aproximação inicial baseada na identificação de pontos únicos e refinada pelo algoritmo ICP, permitindo calcular a transformação entre o referencial da TAC e o intra-operatório. Um grupo de cinco volumes foi adquirido em diferentes regiões do fantoma e foi fundido com os dados da TAC, apresentando um erro de registo de aproximadamente 2 mm . Após combinar os resultados obtidos com o sistema de navegação, concluiu-se que, apesar de apresentar algumas limitações, a ultrassonografia pode ser usada como imagem intra-operatória neste procedimento.

Palavras-chave: Coluna Lombar; Parafusos Pediculares; Fantoma; Planeamento Cirurgico; Cirurgia Guiada por Imagem; Intraoperativo; Ultrasons; Nuvem de Pontos; Registo.

Acknowledgments

Durante a realização desta Tese, muitas foram as pessoas que me ajudaram e apoiaram e, por isso, esta não fica completa sem umas palavras de agradecimento.

Antes de mais, agradeço ao Professor Jorge Martins a oportunidade de trabalhar no Laboratório de Cirurgia Robótica, num tema tão interessante que me fez abrir os meus horizontes e aprender muito sobre diferentes temas, alguns deles pouco abordados ao longo dos últimos 5 anos. Quero também agradecer ao Dr. Herculano pelas reuniões no Hospital de Santa Maria e por todo o apoio prestado durante este trabalho. Agradeço também ao Sr. Raposeiro, pela ajuda e paciência durante a impressão do modelo 3-D.

Agradeço à malta do Laboratório, Miguel, Pawel, Vanessa, Rui, Mariana e João por toda a ajuda e por tornarem o trabalho da Tese mais agradável. Agradeço especialmente à Vanessa, pelos momentos de humor e pela ajuda e horas incontáveis a tentar pôr os softwares a funcionar, e à Mariana Elyseu, pelas dicas e pelo trabalho dela que me ajudaram bastante no início do projeto.

Quero também agradecer aos amigos que a Engenharia Biomédica me deu, por todos os momentos especiais vividos ao longo destes 5 anos, e em especial neste último, pois estavam sempre presentes e sem eles não estaria aqui: Manel, Cate, Miranda, Teresa, Rafa, Marta, Pipo, Dudu, Leitão, Rodrigo, Lina e a minha conterrânea Tânia.

Agradeço à TUIST – Tuna Universitária do Instituto Superior Técnico, por me mostrar que há mais no Técnico que o estudo, por todos os momentos de folia, por me levar de Norte a Sul de Portugal, França e Alemanha e por me ter dado amigos para a Vida. Agradeço especialmente à Geração Tomás, por terem crescido comigo a *“Viajar Sempre a Cantar”*.

E como estes últimos tempos não foram só IST, quero agradecer ao Agrupamento 342-Vialonga, aos meus irmãos Escuteiros e, especialmente, aos Lobitos e Equipa de Animação, que me acompanharam a cada fim de semana e me fazem uma melhor pessoa.

Por último: Muito Obrigado Cristina, Paulinho e Rita! Aos primeiros, por serem os melhores pais do Mundo, por fazerem tudo por mim e por me darem todas as oportunidades para aprender, divertir e crescer; à última, por Tudo, por me acompanhar há anos no bom e no mau, e por me dar na cabeça e me motivar sempre.

Muito obrigado a todos!

Table of Contents

Preface.....	i
Declaração	iii
Declaration	iii
Abstract	v
Resumo.....	vii
Acknowledgments	ix
Table of Contents	xi
List of Figures	xv
List of Tables.....	xxi
List of Acronyms	xxiii
List of Symbols	xxv
1. Introduction	1
1.1. Motivation	1
1.2. Objectives	2
1.3. Thesis Outline.....	3
2. Background	4
2.1. The lumbar spine	4
2.1.1. Anatomy of the lumbar spine.....	4
2.1.2. Lumbar spine diseases.....	5
2.2. State of the Art.....	7
2.2.1. Historical perspective on minimally invasive spine surgery.....	7
2.2.2. Image-Guided spine surgery	9
2.2.3. Registration.....	10
2.2.4. Ultrasound imaging in spine surgery	12
3. Phantom construction.....	13
3.1. Segmentation	13
3.2. 3-D Printing.....	14
3.3. Vertebrae stacking.....	15
3.4. Phantom conclusion	16
4. Methods	17

4.1.	CT-scan	17
4.1.1.	CT segmentation	18
4.1.2.	Surgical Planning - GUI	20
4.1.3.	CT-data post-processing	23
4.2.	Freehand 3-D Ultrasound imaging	23
4.2.1.	Devices	23
4.2.2.	Probe calibration	27
4.2.3.	Acquisition	30
4.2.4.	US segmentation - GUI.....	32
4.3.	Registration	34
4.3.1.	Registration algorithms	35
4.3.2.	Data registration	36
4.4.	Navigation System.....	37
5.	Results	39
5.1.	CT-scan	39
5.1.1.	CT segmentation	39
5.1.2.	Surgical planning	40
5.1.3.	CT-data post-processing	41
5.2.	Freehand 3-D Ultrasound imaging	42
5.2.1.	Calibrations	42
5.2.2.	Acquisitions.....	44
5.2.3.	US segmentation	45
5.3.	Registration	47
5.3.1.	Algorithms testing	47
5.3.2.	Kabsch algorithm	50
5.3.3.	ICP algorithm	59
5.4.	Navigation System.....	67
6.	Discussion.....	69
6.1.	CT-scan	69
6.2.	Freehand 3-D Ultrasound imaging	71
6.2.1.	Calibrations	71
6.2.2.	Acquisitions and segmentation	72
6.3.	Registration	74
6.3.1.	Kabsch algorithm	74
6.3.2.	ICP algorithm	75
6.4.	Navigation System.....	78
7.	Conclusion	79

7.1. Future work.....	80
References	81
8. Appendix.....	86
8.1. Appendix A - Gelatine recipe	86
8.2. Appendix B - ICP RMSE.....	87
8.2.1. Full lumbar spine – medial.....	87
8.2.2. Full lumbar spine – left.....	88
8.2.3. Full lumbar spine – right	89
8.2.4. L3 vertebra – right (1 st)	90
8.2.5. L3 vertebra – right (2 nd).....	92

List of Figures

Figure 1 - Stabilization system composed by pedicle screws and metallic rods. (Image from [3]).....	1
Figure 2 - Pedicle screw.	1
Figure 3 - The lumbar vertebrae bone features (superior view). (Adapted from [7]).....	5
Figure 4 - Detail of the lumbar spine ligaments. (Adapted from http://www.spinesurgery.co.in/anatomy.html)	5
Figure 5 - Herniated disc with nerve root compression. (Adapted from https://mayfieldclinic.com/pe-hldisc.htm)	7
Figure 6 - Person with scoliosis, a deformity in the coronal plane. (Adapted from https://www.vikalpphysio.in/back-pain-clinic/scoliosis/)	7
Figure 7 - Minimally invasive pedicle screw placement as performed by Lowery and Kulkarni. (Adapted from [25])	8
Figure 8 - The Sextant system (Medtronic Sofamor Danek, Memphis, TN, USA) for insertion of stabilizing rod. (Adapted from [26])	8
Figure 9 - Image-guided surgery by Nolte <i>et al.</i> A: Surgical tool with position-tracked markers. B: Detail of the navigation system, with the CT plan and the intraoperative COS matched. (Adapted from [28]).	9
Figure 10 - The O-arm system (Medtronic Navigation, Medtronic Inc, Dublin, Ireland). A: The O-arm imaging device. B: Detail of the tracked reference, allowing automatic registration. (Adapted from [36])	10
Figure 11 - Registration between CT scan COS and operative theatre COS. (Adapted from https://en.wikipedia.org/wiki/CT_scan#/media/File:UPMCEast_CTscan.jpg and https://www.hfmmagazine.com/articles/2090-improving-operating-room-cleaning-efficiency)	11
Figure 12 - A: Preoperative MRI showing the spinal cord (asterisk) squashed into into a very narrow spinal canal (arrow). B: IoUS imaging following laminectomy, showing a satisfactory decompression of the spinal cord. (Adapted from [41]).....	12
Figure 13 - Vertebrae segmentation by manually painting each vertebra.....	13
Figure 14 - 3D Slicer workspace with the completed segmentation (note the spondylolisthesis occurring at L4-L5 level, purple and pink vertebrae).....	14
Figure 15 - 3-D printing. A: MakerBot 3-D printer at Pavilhão de Mecânica III (IST). B: Vertebra printing detail	14
Figure 16 - Printed vertebrae before (A) and after (B) the sanding and the acetone bath (L5 was being printed in A).	15
Figure 17 - Complete spine model. A: Posterior view. B: Lateral view (left).	16

Figure 18 - Lumbar spine phantom	16
Figure 19 – Proposed structure of an US image-guided surgery for pedicle screw placement.....	17
Figure 20 - CT-scan of the Lumbar spine phantom: axial (A), sagittal (B) and coronal (C) slices.	18
Figure 21 – Segmentation after applying the threshold.	19
Figure 22 – Segmentation after applying the island tool.	19
Figure 23 - Segmentation after the manual finishing.	20
Figure 24 - Surgical planning process for placing pedicle screws in L3 vertebra.	21
Figure 25 - Surgical planning process for placing pedicle screws in L3 vertebra (continuation).	22
Figure 26 - CT-derived model processing. A: CT segmentation. B: CT segmentation after column scanning (US reaching regions).	23
Figure 27 - Passive Polaris Spectra System	24
Figure 28 - Polaris passive tools. A: Pointer. B: Tool attached to the US probe.	24
Figure 29 - ProSound 2 US system with the UST-586-5 transducer	25
Figure 30 – Frame grabber with video input (yellow) and USB output.	25
Figure 31 - Freehand 3-D Ultrasound imaging device setup	26
Figure 32 - Freehand 3-D Ultrasound existing COS and transformations between them.	26
Figure 33 - Pointer pivoting.	28
Figure 34 - Probe calibration. Detail of the existing COS and transformations between them.....	28
Figure 35 - Stradwin interface during probe calibration. The tip of the pointer is automatically segmented as the brighter pixel in the US frame.	29
Figure 36 – Axial acquisitions of the entire length of the phantom: medially (A), left (B), right (C).....	31
Figure 37 - Sagittal acquisitions at the level of L3 right side.	31
Figure 38 - US segmentation GUI	32
Figure 39 - US segmentation after applying the median filter.	33
Figure 40 - US segmentation after applying the threshold.....	33
Figure 41 - US segmentation after performing the column scanning.....	34
Figure 42 - Superior and lateral (right) view of T11 vertebra 3D model (axes scales in mm).	39
Figure 43 - Superior and lateral (right) view of T12 vertebra 3D model (axes scales in mm).....	39
Figure 44 - Superior and lateral (right) view of L1 vertebra 3D model (axes scales in mm).....	39
Figure 45 - Superior and lateral (right) view of L2 vertebra 3D model (axes scales in mm).....	39
Figure 46 - Superior and lateral (right) view of L3 vertebra 3D model (axes scales in mm).....	39

Figure 47 - Superior and lateral (right) view of L4 vertebra 3D model (axes scales in mm).....	39
Figure 48 - Superior and lateral (right) view of L5 vertebra 3D model (axes scales in mm).....	40
Figure 49 - Superior, lateral (right), posterior and anterior view of the seven vertebrae 3-D modes (axes scales in mm).....	40
Figure 50 – Posterior view (left, medial and right) of the L2, L3 and L4 vertebrae with each pedicle screw in their planned locations.	40
Figure 51 - Point Cloud of the posteriormost regions of all the vertebrae (Video 3).	41
Figure 52 - Point Cloud of the posteriormost regions of the L3 vertebra (Video 4).....	41
Figure 53 - Calibration result. In this figure, the pointer’s tip is identified based on the Polaris data and not based on image segmentation. A: Tip close to US probe. B: Tip far from the US probe.	43
Figure 54 – Visualization of the US frames of each acquisition group, in the Polaris COS. A: full lumbar spine – left (Video 6). B: full lumbar spine – medial (Video 5). C: full lumbar spine – right (Video 7). D: L3 vertebra – right (1 st) (Video 8). D: L3 vertebra – right (2 nd) (Video 9).....	45
Figure 55 – US-derived PC resulting from the segmentation of the full lumbar spine – medial US acquisition, in the Polaris COS (Video 10).	45
Figure 56 - US-derived PC resulting from the segmentation of the full lumbar spine – left US acquisition, in the Polaris COS (Video 11).	46
Figure 57 - US-derived PC resulting from the segmentation of the full lumbar spine – right US acquisition, in the Polaris COS (Video 12).	46
Figure 58 - US-derived PC resulting from the segmentation of the L3 vertebra – right (1 st) US acquisition, in the Polaris COS (Video 13).	47
Figure 59 - US-derived PC resulting from the segmentation of the L3 vertebra – right (2 nd) US acquisition, in the Polaris COS (Video 14).	47
Figure 60 - Control PC (vertices of the L3 3-D model).	48
Figure 61 - Original PC (below) and transformed PC (above).	48
Figure 62 - Result of running the ICP algorithm without initial approximation.	49
Figure 63 - Final registration method. A: Acquisition of three points in the original PC. B: Acquisition of approximately matching points in the transformed PC. C: Initial approximation which resulted from the Kabsch algorithm. D: Final alignment, after the refinement with the ICP algorithm.	49
Figure 64 – Selection of the pair-points in CT-derived PC and in the full lumbar spine – medial US PC.	50
Figure 65 – Superposition of the full lumbar spine – medial US PC after the initial transformation (in semi-transparent red) with the CT-derived PC (Video 15).	51
Figure 66 - Selection of the pair-points in CT-derived PC and in the full lumbar spine – left US PC. ..	52

Figure 67 - Superposition of the full lumbar spine – left US PC after the initial transformation (in semi-transparent red) with the CT-derived PC (Video 16).	53
Figure 68 - Selection of the pair-points in CT-derived PC and in the full lumbar spine – right US PC. 54	
Figure 69 - Superposition of the full lumbar spine – right US PC after the initial transformation (in semi-transparent red) with the CT-derived PC (Video 17).	55
Figure 70 - Selection of the pair-points in CT-derived L3 PC and in the L3 vertebra – right (1 st) US PC.	56
Figure 71 - Superposition of the L3 vertebra – right (1 st) US PC after the initial transformation (in semi-transparent red) with the CT-derived L3 PC (Video 18).	57
Figure 72 - Selection of the pair-points in CT-derived L3 PC and in the L3 vertebra – right (2 nd) US PC.	58
Figure 73 - Superposition of the L3 vertebra – right (2 nd) US PC after the initial transformation (in semi-transparent red) with the CT-derived L3 PC (Video 19).	59
Figure 74 - Superposition of the full lumbar spine – medial US PC after the final transformation (in semi-transparent red) with the CT-derived PC (Video 20).	60
Figure 75 - Superposition of the full lumbar spine – left US PC after the initial transformation (in semi-transparent red) with the CT-derived PC (Video 21).	61
Figure 76 - Superposition of the full lumbar spine – right US PC after the initial transformation (in semi-transparent red) with the CT-derived PC (Video 22).	62
Figure 77 - Superposition of the L3 vertebra – right (1 st) US PC after the final transformation (in semi-transparent red), computed with the CT-derived L3 PC as reference, and the CT-derived L3 PC (Video 23).	63
Figure 78 - Superposition of the L3 vertebra – right (1 st) US PC after the final transformation (in semi-transparent red), computed with the complete CT-derived L3 PC as reference, and the complete CT-derived PC (Video 24).	64
Figure 79 - Superposition of the L3 vertebra – right (1 st) US PC after the final transformation (in semi-transparent red), computed with the complete CT-derived L3 PC as reference, and the CT-derived L3 PC (detail of the previous figure) (Video 25).	64
Figure 80 - Superposition of the L3 vertebra – right (2 nd) US PC after the final transformation (in semi-transparent red), computed with the CT-derived L3 PC as reference, and the CT-derived L3 PC (Video 26).	65
Figure 81 - Superposition of the L3 vertebra – right (2 nd) US PC after the final transformation (in semi-transparent red), computed with the complete CT-derived L3 PC as reference, and the complete CT-derived PC (Video 27).	66

Figure 82 - Superposition of the L3 vertebra – right (2 nd) US PC after the final transformation (in semi-transparent red), computed with the complete CT-derived L3 PC as reference, and the CT-derived L3 PC (detail of the previous figure) (Video 28).	66
Figure 83 - Navigation system's interface with the CT-derived PC and the surgical plans.....	67
Figure 84 – Polaris Pointer in the extremity of the left transverse process of L2. A: Navigation System. B: Lumbar Spine Phantom.	67
Figure 85 - Polaris Pointer in the extremity of the left transverse process of L3. A: Navigation System. B: Lumbar Spine Phantom.	68
Figure 86 - Polaris Pointer surgical plan for left L2 pedicle screw. A: Navigation System. B and C: Lumbar Spine Phantom.....	68
Figure 87 – CT-scan of a real patient's lumbar spine: axial (A), sagittal (B) and coronal (C) slices.....	70
Figure 88 - Intersections of one pedicle screw with the CT slices. Detail of the Surgical Planning (Figure 25).	70
Figure 89 - Differences in the angle α between the pointer and the direction perpendicular to the US propagation. The smaller α , the more perceptible is the pointer tip in the US image.	72
Figure 90 - US frame of a real patient's vertebra with its main features highlighted.....	73

List of Tables

Table 1 – Coordinates of the insertion points and directions for the planned pedicle screws.....	40
Table 2 – Results of the pointer pivoting step and corresponding error.	42
Table 3 – Results of the probe calibration step and corresponding error.	43
Table 4 – Coordinates of the pair-points (fiducials) selected for the initial approximation between the full lumbar spine – medial US PC and the CT PC.....	51
Table 5 - Coordinates of the pair-points (fiducials) selected for the initial approximation between the full lumbar spine – left US PC and the CT PC.	52
Table 6 - Coordinates of the pair-points (fiducials) selected for the initial approximation between the full lumbar spine – right US PC and the CT PC.	54
Table 7 – Coordinates of the pair-points (fiducials) selected for the initial approximation between the L3 vertebra – right (1 st) US PC and the CT PC.	56
Table 8 - Coordinates of the pair-points (fiducials) selected for the initial approximation between the L3 vertebra – right (2 nd) US PC and the CT PC.	58
Table 9 - RMSE for each ICP iteration in the registration between the full lumbar spine - medial PC and the CT-derived PC.....	87
Table 10 - RMSE for each ICP iteration in the registration between the full lumbar spine - left PC and the CT-derived PC.....	88
Table 11 - RMSE for each ICP iteration in the registration between the full lumbar spine - right PC and the CT-derived PC.....	89
Table 12 - RMSE for each ICP iteration in the registration between the L3 vertebra – right (1 st) PC and the CT-derived L3 PC.....	90
Table 13 - RMSE for each ICP iteration in the registration between the L3 vertebra – right (1 st) PC and the complete CT-derived PC.	91
Table 14 - RMSE for each ICP iteration in the registration between the L3 vertebra – right (2 nd) PC and the CT-derived L3 PC.....	92
Table 15 - RMSE for each ICP iteration in the registration between the L3 vertebra – right (2 nd) PC and the complete CT-derived PC.	93

List of Acronyms

2-D	Two-Dimensional
3-D	Three-Dimensional
ABS	Acrylonitrile Butadiene Styrene
COS	Coordinate System
CT	Computed Tomography
DICOM	Digital Imaging and Communications in Medicine
ICP	Iterative Closest Point
IG	Image-Guided
ioUS	Intraoperative Ultrasound
IVD	Intervertebral Discs
LBP	Lower Back Pain
LS	Lumbar Spine
MRI	Magnetic Resonance Imaging
PC	Point Cloud
PLIF	Posterior Lumbar Interbody Fusion
RMSE	Root Mean Square Error
ROI	Region of Interest
SVD	Singular Value Decomposition
US	Ultrasound

List of Symbols

S_u	Scale in the x direction
S_v	Scale in the y direction
t_x	Translation in x axis
t_y	Translation in y axis
t_z	Translation in z axis
α	Azimuth – rotation around z axis
β	Elevation – rotation around y axis
γ	Roll – rotation around x axis

1. Introduction

1.1. Motivation

Nowadays, lower back pain (LBP) is a condition with a great impact in general well-being and its prevalence has been increasing [1]. Although it can be caused by different diseases or accidents, chronic LBP is often caused by more complex conditions, such as intravertebral discs disorders or deformity. Patients suffering from chronic LBP showing no signs of improvement after nonsurgical procedures may be considered to a lumbar spine surgery [2].

Most lumbar spine surgeries performed worldwide, as nerve decompression, intervertebral fusion or deformity correction, use stabilization mechanisms to fixate the spine in its defined position, give support and prevent relative motion between different spine segments. This stabilization mechanisms are composed of pedicular screws and metallic rods, as shown in Figure 1 [3].

Pedicle screws, presented in Figure 2, are considered the “state of the art” for the treatment of spine deformities [3]. They are placed through the pedicle region of the vertebrae by a posterior approach and allow to rigidly attach the metallic rods to the spine segments that the surgeon wants to stabilize, guiding the vertebrae to their new position or simply fixating them in their current location.



Figure 1 - Stabilization system composed by pedicle screws and metallic rods. (Image from [3])



Figure 2 - Pedicle screw.

Since pedicle screws began to be used, the surgical procedures to insert them have been changing, based on the new techniques which have been developed, such as minimally invasive surgeries and image-guided procedures. Image-guided (IG) placement of pedicle screws arise recently with the advent of powerful computer systems capable of real-time tracking surgical instruments in conjunction

with preoperative and intraoperative medical images. This technique allowed to increase the accuracy and security of the procedures with pedicle screws [4].

In an IG surgery for inserting pedicle screws it is crucial to acquire some intraoperative volumetric images, that can be merged with the preoperative plans by registering the different imaging data and which must be concordant with the intraoperative referential or coordinate system (COS). The surgical instruments are also tracked in this intraoperative COS, allowing the surgeon to have real-time feedback of the positions of the tools in a navigation system. The more recent IG setups commercially available make use of 3-D fluoroscopy, CT or MRI to acquire their intraoperative images. Although this imaging modalities present good image quality and great detail of the spine region, they present some disadvantages like the emission of ionizing radiation (except for MRI), their high cost and the reduced mobility.

These factors led to studies aimed at replacing the currently used intraoperative imaging methods with a non-ionizing, low-cost, mobile and real-time imaging technique, such as Ultrasounds (US) [5].

The work presented in this thesis represents a step further for performing IG surgeries for placing pedicle screws using low cost, non-ionizing intraoperative imaging. For this project we acquired US volume data to obtain the location of the spine during surgery in the intraoperative referential, which after registration with the preoperative CT data, allowed to track the surgical tools relative to the same referential using a navigation system, assisting the surgeon to perform pedicle screw placement as planned in the preoperative data.

1.2. Objectives

The main objective of the proposed project was to simulate an image-guided surgery for inserting pedicle screws in the lumbar spine, using Freehand 3-D Ultrasound imaging as the intraoperative imaging modality and performing registration between the preoperative CT data with the surgical plans and the intraoperative data. To achieve this goal, we divided it in simpler objectives:

- The construction of a lumbar spine phantom, which played the role of our patient, allowing to perform the different stages of the surgery;
- The acquisition of preoperative CT data, which allowed to obtain the 3-D models of each vertebrae and perform the surgical plans;
- The acquisition of intraoperative Freehand 3-D Ultrasound volumes, which allowed to know the intraoperative position of the lumbar spine phantom in the surgical theatre;
- The registration of the pre and intraoperative data, which allowed to compute the pedicle screw plans, with their insertion points and orientations, in the surgical theatre referential;
- The development of a simple navigation system, which allowed to visualize in real-time the surgical tools and their relative position to the lumbar spine model and the surgical plans.

1.3. Thesis Outline

This thesis is divided in seven chapters: “Introduction”, “Background”, “Phantom construction”, “Methods”, “Results”, “Discussion” and “Conclusion”.

Chapter “Introduction” presents the relevance of this project and its main objectives.

Chapter “Background” presents a brief anatomical description of the lumbar spine and its main diseases. It is also presented an introduction to minimally invasive surgery, image-guided surgery, registration and ultrasound concepts and their state of the art regarding lumbar surgery. In general, this chapter’s purpose is that the reader becomes acquainted with the topics necessary to understand the developed work.

Chapter “Phantom construction” presents the steps for constructing the lumbar spine phantom, a model created to test the presented work, replacing a real patient. The construction of the phantom is not included in the methods because it is not part of an IG surgery.

Chapter “Methods” presents every step done to perform our IG surgery using intraoperative US imaging, from the acquisition of the preoperative CT-data of the lumbar spine phantom to the application of a navigation system to obtain real-time visual feed-back of the surgery tools and the phantom. This chapter’s structure is based on a real procedure’s chronological events.

Chapter “Results” presents the main results of each step performed to accomplish this project’s goal and the associated errors of each method stage.

Chapter “Discussion” presents a more detailed description and the discussion of the obtained results and their main errors. It also presents the discussion about the difficulties faced in each step of this work and the possible origin of the main errors obtained.

Chapter “Conclusion” presents an overall review of the presented work, comparing it with its main objectives. It also provides some suggestions on how to improve this work in the future.

2. Background

This chapter presents some background notions, such as the anatomy of the lumbar spine and the state of the art in spine surgery, which are essential to understand the developed project.

2.1. The lumbar spine

The vertebral column, also known as spine, consists of a series of irregular bones, the vertebrae, stacked one on top of each other, separated by intervertebral discs (IVD) between their bodies and which are bound together by ligaments. The vertebrae are divided in 5 groups: 7 cervical vertebrae (C1-C7), 12 thoracic vertebrae (T1-T12), 5 lumbar vertebrae (L1-L5) and the sacrum (S1-S5) and the coccyx, which are formed respectively by 5 and 4 fused vertebrae. Within each group, the vertebrae are similar in shape and orientation [6].

Each group has different functions regarding its location, but in general they provide support to the human body, allowing to stand upright and to move, while protecting the spinal cord from injury and hold some adjacent structures, such as the rib cage or the muscles of the back [7].

2.1.1. Anatomy of the lumbar spine

The lumbar spine (LS) comprises the 5 lumbar vertebrae. These vertebrae are the stoutest and strongest vertebrae due to their function of supporting body weight. They present three main features: the body, the vertebral arch and the processes, as seen in Figure 3.

- The body, the anteriormost portion of the vertebrae, is a kidney-shaped structure with almost parallel upper and lower surfaces and is responsible for structure and weight-bearing.
- The vertebral arch is formed by the pedicles, two short and thick processes, which project backwards to unite with the laminae. The laminae are the flat structures that end medially in the spinous process. The hole between the vertebral body and the arch is the vertebral foramen, through which the spinal cord passes.
- Seven processes extend from the vertebral arch. From the junction of the laminae, the spinous process extends backwards and from the junction of each lamina and a pedicle, the transverse processes project laterally and slightly backwards on each side. The function of these three processes is to serve as muscle attachment surfaces. The other four processes are responsible for forming the joints between adjacent vertebrae. From the root of each transverse process, the articular processes project superiorly and inferiorly, ending in the facets, smooth articulating surfaces covered in hyaline cartilage that face posteromedially on the superior process and anterolaterally on the inferior process.

Each vertebra is separated from the adjacent ones by the IVD, which are composed by the anulus fibrosus, an outer ring of fibrocartilage and the nucleus pulposus, a pulpy, gel-like interior. Although IVD form strong joints, they still allow a great range of movement and absorb vertical shock [6], [7].

The lumbar vertebrae are also linked and stabilized by a group of ligaments, present in Figure 4, which restrict excessive movement, preventing injuries. The most important are:

- Ligamentum Flavum, which connects the upper portions of the laminae to the lower portion of the laminae of the vertebrae above;
- The Anterior Longitudinal Ligament, which connects the anterior portion of the bodies of consecutive vertebrae;
- The Posterior Longitudinal Ligament, which connects the posterior portion of the bodies of consecutive vertebrae;
- The Intertransverse Ligament, which connects the transverse processes of adjacent vertebrae;
- The Interspinous Ligament, which connects the spinous processes of adjacent vertebrae;
- The Supraspinous Ligament, which connects the peaks of the spinous processes, posterior to the interspinous ligament;
- The Capsular Ligament, connecting the articular processes of adjacent vertebrae, evolving articular facet joints [6]–[8].

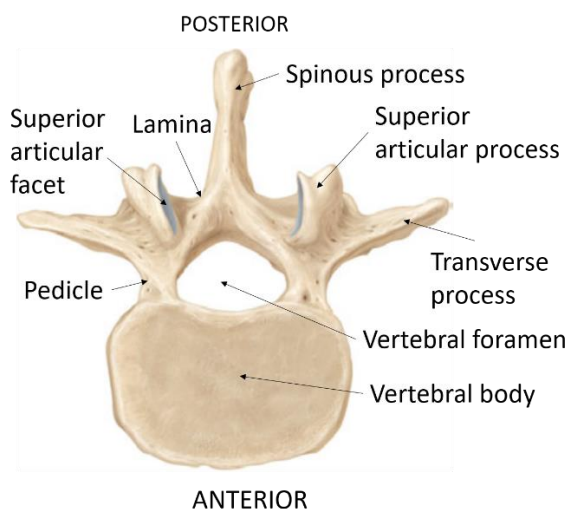


Figure 3 - The lumbar vertebrae bone features (superior view). (Adapted from [7])

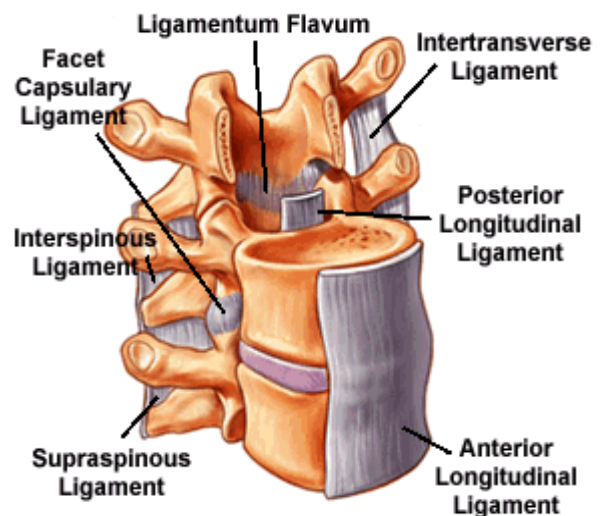


Figure 4 - Detail of the lumbar spine ligaments. (Adapted from <http://www.spinesurgery.co.in/anatomy.html>)

2.1.2. Lumbar spine diseases

Lower Back Pain (LBP) is a common condition, with impact in daily life and general well-being, which can be acute, sub-acute or chronic [9]. LBP, estimated by the 2010 Global Burden of Disease Study

among the top 10 diseases and injuries that account for the highest number of DALYs worldwide [1], causes more global disability than any other condition, with its prevalence increasing due to the ageing population [9], [10]. Despite these facts, LBP is not a disease, but a group of symptoms, which can be associated to different diseases or injuries affecting the LS.

The single most common cause for LBP is muscle strain and/or ligament sprain, which can occur after an excessive load lifting, sudden movements, bad posture over time or sports injuries [11]. However, these conditions are related to acute or sub-acute pain, and their treatment is usually simple, with the administration of anti-inflammatory medicines, muscle relaxants and non-invasive procedures [12].

Chronic LBP, which usually has a more complex cause, typically involves some IVD disorder, problems in the joints and/or irritated nerve roots. The main diseases associated with chronic LBP are [2], [12], [13]:

- Lumbar Herniated Disc – nucleus pulposus breaks through the anulus fibrosus, causing inflammation and compressing nearby nerve roots, as shown in Figure 5;
- Degenerative Disc Disease – caused by the loss of hydration in the IVD over time, degrading its capacity of resisting forces, which are transferred to the disc wall that cause pain and may lead to herniation;
- Facet Joint dysfunction – caused by degenerated cartilage in the articular region by wear, due to constant motion, leading to inflammation and pain;
- Spinal Stenosis – narrowing of the spinal canal, compressing the nerve roots;
- Spondylolisthesis – occurs when one vertebra slips over the adjacent one, usually associated with instability or deformity of the facet joints;
- Deformity – such as scoliosis, present in Figure 6 (coronal plane) or kyphosis (sagittal plane), which may cause pain if it leads to breakdown of the IVD, facet joints or to nerve compression;
- Trauma – acute fractures or dislocations may cause pain.

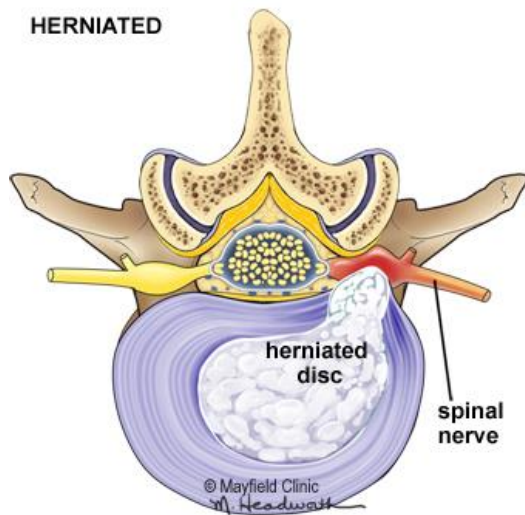


Figure 5 - Herniated disc with nerve root compression. (Adapted from <https://mayfieldclinic.com/pe-hldisc.htm>)

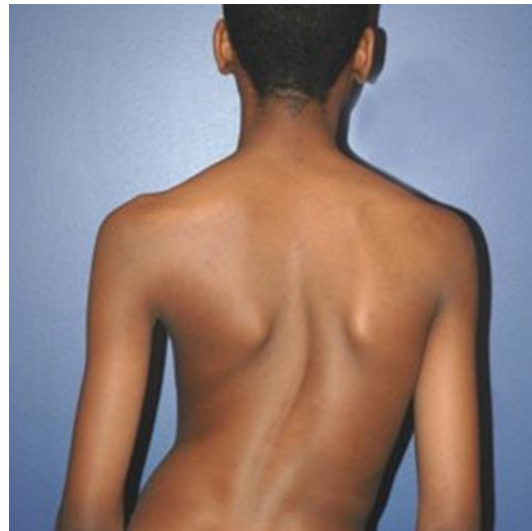


Figure 6 - Person with scoliosis, a deformity in the coronal plane. (Adapted from <https://www.vikalpphysio.in/back-pain-clinic/scoliosis/>)

If chronic LBP shows no signs of improvement after nonsurgical treatment, it may be considered a lumbar spine surgery. The most common procedures are the Decompression Surgery, which aims to remove portions of a vertebra – Laminectomy – or of the IVD – Discectomy – that are compressing nearby nerve roots and the Lumbar Spinal Fusion, where the IVD between two or more adjacent vertebrae are removed and substituted by bone graft and an IVD replacement, promoting the fusion of consecutive vertebral bodies and stabilizing that region [2].

2.2. State of the Art

Spine surgery has evolved throughout history. This section briefly summarizes its development, the appearing and increasing use of minimally invasive techniques, and the introduction of image-guided (IG) procedures, allowing better intraoperative navigation in the spine. It will be focused on pedicle screw placement procedures and the use of intraoperative Ultrasound (ioUS) images. This section also describes the registration methods, essential in any surgical navigation system.

2.2.1. Historical perspective on minimally invasive spine surgery

Although the first evidence known of a spinal surgery was performed and described by ancient Egyptians around 1500 [14], Hippocrates is considered the father of spine surgery, due to his writings and the treatment principles he proposed [15]. There are some reports of spine surgeries being made during Middle Ages, like the one performed by Paulus of Aegina [16] or those described by Şerefeddin

Sabuncuoğlu in his atlas [17]. In more recent years, Oppenheim and Krause performed the first lumbar laminectomy and discectomy, as reported in 1909 [18].

Initially, spinal surgeries were performed by an open surgery approach, but with technological advancements, last century has witnessed the development of minimally invasive techniques. Its use has been growing, due to their better outcomes, mainly associated with reduced tissue trauma, less blood loss or faster recovery, when compared with a more traditional operation.

In 1939, Love reported the first minimal invasive interlaminar technique for treating a protruded IVD [19] and, in 1975, Hijikata *et al.* reported the use of arthroscopic techniques to perform the first percutaneous nucleotomy for posterolateral lumbar disc herniations [20]. Yasargil and Caspar introduced the microsurgical treatment of herniated IVD by using an operating microscope in the spine, both in 1977 [21], [22].

After the first posterior lumbar interbody fusion (PLIF), to treat spondylolisthesis and degenerative disc disease, was reported in 1953 by Cloward [23], new minimal approaches have been studied to improve this procedure, as well as new ways of immobilizing vertebrae to fusion, and in 1995, Mathews *et al.* introduced the first pedicle screws to assist interbody fusion, using subcutaneous plates to connect them [24]. A similar procedure was described by Lowery and Kulkarni in 1999, shown in Figure 7, but utilizing a rod to stabilize the screws and, consequentially, the lumbar spine [25] and which presented an high successful fusion rate. New instrumentation continued to appear, and in 2002, Foley and Gupta presented the Sextant (Medtronic Sofamor Danek, Memphis, TN, USA), present in Figure 8, a system to fixate the pedicle screw rod percutaneously [26]. After the work of Foley introducing the Sextant, several other minimally invasive systems to fixate the lumbar spine were developed, as the ATAVI (Endius, Plainville, MA, USA), Aperture (Depuy Spine, Raynham, MA, USA), and Pathfinder (Spinal Concepts; Austin, TX, USA) systems [27].

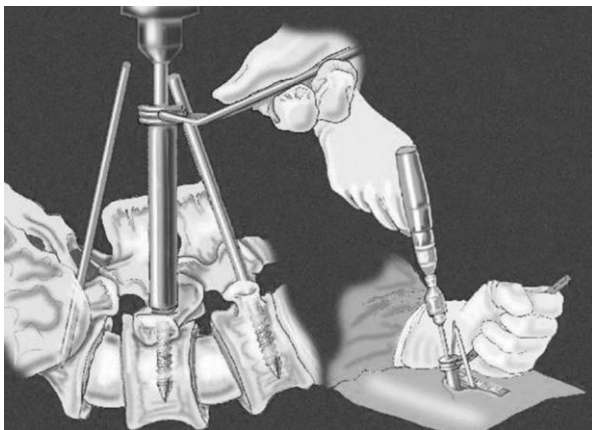


Figure 7 - Minimally invasive pedicle screw placement as performed by Lowery and Kulkarni. (Adapted from [25])

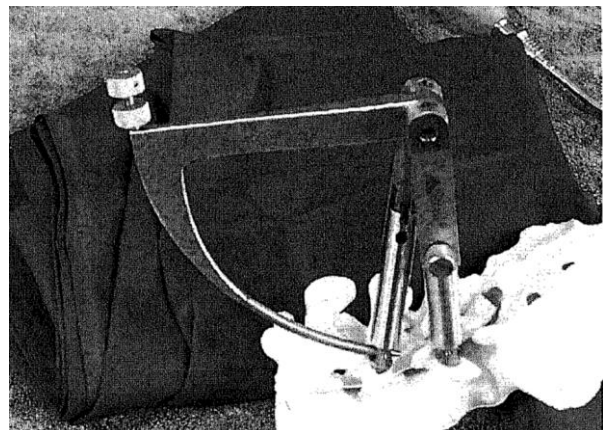


Figure 8 - The Sextant system (Medtronic Sofamor Danek, Memphis, TN, USA) for insertion of stabilizing rod. (Adapted from [26])

2.2.2. Image-Guided spine surgery

Parallel to the development of new minimally invasive techniques and tools, the use of new medical imaging techniques, such as three-dimensional (3-D) image reconstruction, able to support those procedures started, allowing a better navigation inside the spine and a better understanding of the accuracy of the surgeries. In the early 1990's, new powerful computer systems allowing real time image processing and instrument-tracking techniques permitted address the issue of accuracy of surgeries in new ways, resulting in the first successful application of an IG system for pedicle screw placement, in the lumbar spine, in 1995 [28]. This method, shown in Figure 9, introduced by Nolte *et al.*, used pre-operative CT or MRI images to plan the trajectory of the surgery and an instrument-tracking system to observe in real-time the position of the surgical tools in the spine. This was possible by knowing the transformation between the acquired images and the intraoperative real physical position of the vertebrae, i.e. by registering the two different coordinate systems, as will be explained in subsection 2.2.3.

After Nolte's work, various IG surgeries methods have been studied, with some differences in terms of the imaging techniques utilized or the registration performed [4], being the CT matching [29]–[31], 2-D fluoroscopy [32], [33] and 3-D fluoroscopy [34], [35] the most used.

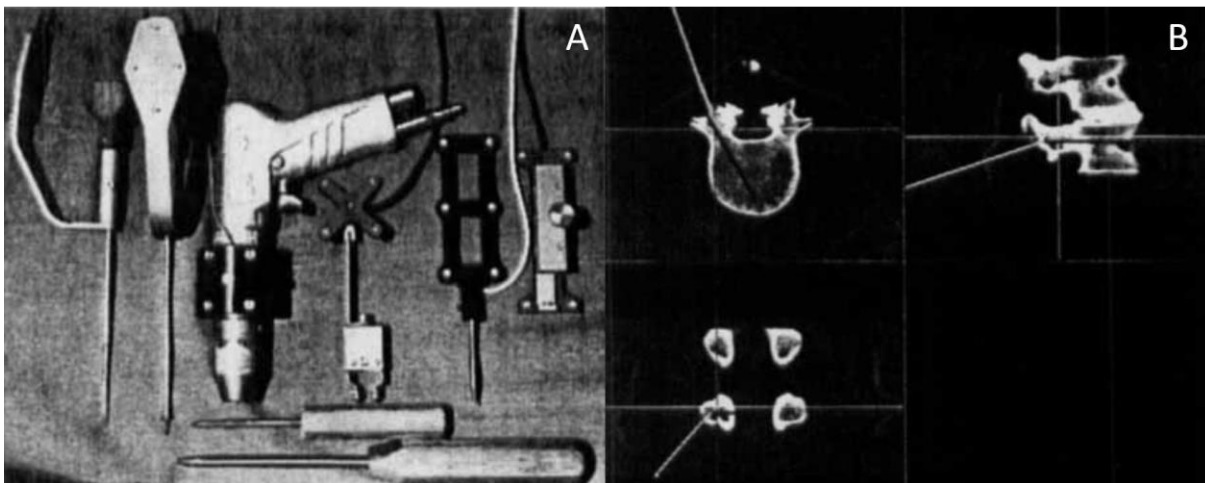


Figure 9 - Image-guided surgery by Nolte *et al.* A: Surgical tool with position-tracked markers. B: Detail of the navigation system, with the CT plan and the intraoperative COS matched. (Adapted from [28])

These studies led to the development of commercially available IG navigation systems, such as the O-arm (Medtronic Navigation, Medtronic Inc, Dublin, Ireland) with the Stealth Station Navigation system (Medtronic Navigation, Medtronic Inc, Dublin, Ireland), present in Figure 10, which are able to provide real-time tracking of the surgical tools while they are maneuvered by the surgeon [36]. Like most currently used systems, O-arm, which is coupled to the Stealth Station Navigation system utilizes intraoperative CT scan acquired while the patient is in surgical position, along with a reference rigidly attached to a bone structure near the intervention site, in the form of a spinous process clamp or pin, which allows registration and the navigation system software to track all the instruments within the surgical field relative to the rigid reference. More recently, the Airo ® (Brainlab AG, Feldkirchen,

Germany) system, a portable, helical CT scanner capable of soft tissue imaging has been used in spine surgery [37], with similar features and outcomes as the O-arm system [38].

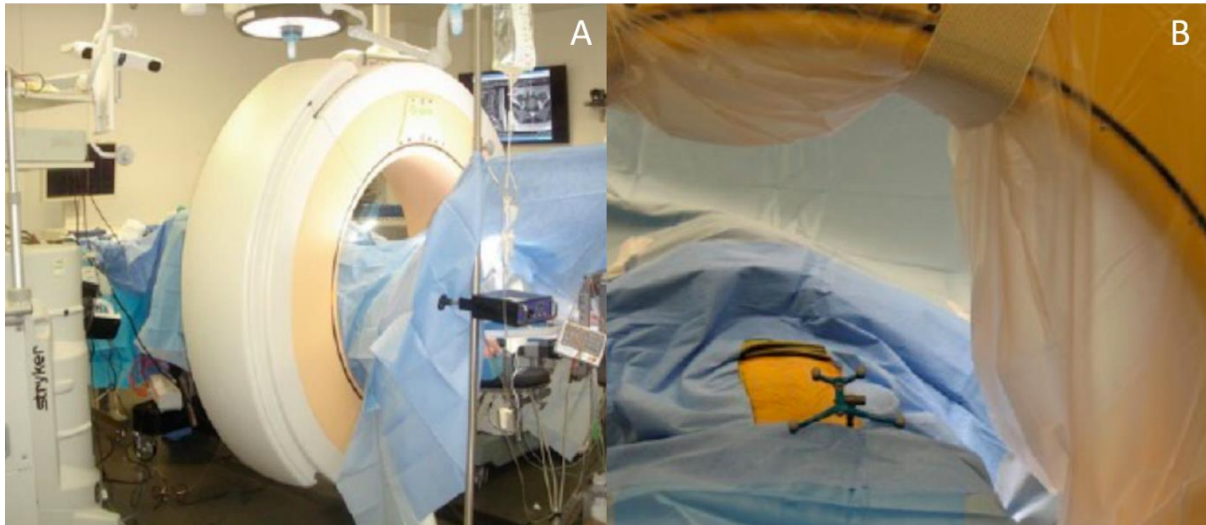


Figure 10 - The O-arm system (Medtronic Navigation, Medtronic Inc, Dublin, Ireland). A: The O-arm imaging device. B: Detail of the tracked reference, allowing automatic registration. (Adapted from [36])

The IG navigation systems for spine surgery presented have important advantages, which are 3-fold [36]:

- increased accuracy of pedicle screw placement;
- minimally invasive applications (small incision, minimal retraction, dissection, bleeding, and infection)
- decreased radiation exposure to the operator, when compared to traditional fluoroscopically assisted techniques

However, despite the decrease in exposure to ionizing radiation compared to other methods, this remains an important factor against the use of CT or fluoroscopy-based IG systems, being necessary an alternative non-ionizing image acquisition method that can substitute X-rays in these procedures, like Ultrasound imaging.

2.2.3.Registration

The registration process, which consists in finding the rigid transformation between different coordinate systems (COS), present in Figure 11, e.g. CT images and intraoperative physical position, is the cornerstone of any navigation system. There are different registration algorithms, depending on the type of image data used or the way virtual and physical reality is matched, but the ones mainly used in spine surgery can be differentiated into active intraoperative registration and automated registration [4].

Active intraoperative registration can be performed by identifying some anatomical landmarks, known as fiducials, in the preoperative CT or MRI and their matching pair-points intraoperatively, by using a position-tracked pointer. At least three non-collinear pair-points must be identified to perform the registration. Also, these points must be far from each other and be located in different levels to provide an optimal spatial resolution [4]. Nolte *et al.* [28] used a registration method similar to this.

On other hand, active intraoperative registration can also be performed by identifying the vertebral surface contours, using the same kind of position-tracked pointer, resulting in a point cloud which is then matched to a 3-D reconstruction of the CT or MRI preoperative data [4]. Usually, pair-points and surface matching methods can be combined, increasing the accuracy of the matching process, although pair-points matching alone do not compromise the accuracy of navigation and is likely to result in decreased operating time if the points are chosen correctly [39].

Besides the tracked-pointer mentioned, vertebral landmarks and surface contours can be identified by other methods, like intraoperative real time position-tracked images, such as Ultrasound tracked snapshots. This method will be explained in detail throughout the next chapters, as it was the method used to perform the registration in this project.

Automated registration is used in more recent systems, such as the O-arm system, mentioned in the previous sub-section, where fluoroscopic images are acquired intraoperatively. The COS matching is automatic due to the traceable markers that equip the fluoroscope, and the reference that is rigidly attached to a spinous process near the vertebra which will be operated. This reference is identified by the fluoroscope and the navigation system performs the registration automatically. The principal disadvantage of automated registration is related to the great increase of the navigational error if the reference relative position to the spine changes, result of accidental manipulation [4].



Figure 11 - Registration between CT scan COS and operative theatre COS. (Adapted from https://en.wikipedia.org/wiki/CT_scan#/media/File:UPMCEast_CTscan.jpg and <https://www.hfmmagazine.com/articles/2090-improving-operating-room-cleaning-efficiency>)

2.2.4. Ultrasound imaging in spine surgery

Ultrasound imaging (US), or ultrasonography, is an imaging modality that uses non-ionizing, high frequency sound waves to acquire real time images of the body internal structures. Ultrasound waves are emitted by a transducer and, based on the different acoustic impedances of the internal organs, they reflect with different amplitudes at different depths. The time it takes for the wave to reflect and the amplitudes measured allow the ultrasound machine to compute a 2-D image [40], known as B-scan .

During the second half of last century, US application widespread in many medical specialties as an important diagnostic tool [41]. In 1982, Dohrmann and Rubin reported the use of intraoperative US (ioUS) imaging of the spinal cord [42], as shown in Figure 12, one of the first articles on this technique, which still remains the principal use of ioUS in spine surgery [38].

Regarding pedicle screw placement and IG procedures, ioUS imaging has been studied as an alternative to ionizing intraoperative imaging methods, such as CT and fluoroscopy. This is possible using a position-tracked US transducer, which allow to compute the acquired US images in the COS of the operation room. This method, known as Freehand 3-D Ultrasound imaging [43], creates a 3-D US data that can be matched with the preoperative CT scan or MRI, with the surgical plans and screw trajectory, after identifying some vertebral fiducials or surface contours, like explained in the previous sub-section. Brendel *et al.* proposed this approach in 2002, matching the 3-D reconstruction of the vertebral surface of a preoperative CT scan with a set of tracked ioUS [44] and more recently, in 2013, Tamas *et al.* reported the successful registration of tracked ioUS snapshots to CT data, identifying a group of pair-points fiducials in both the US images and the CT reconstruction [5]. After comparing the US-derived with the CT-derived surgical plans, they concluded that this approach is feasible and may allow accurate non-ionizing IG pedicle screw placement, after further studies and improvements.

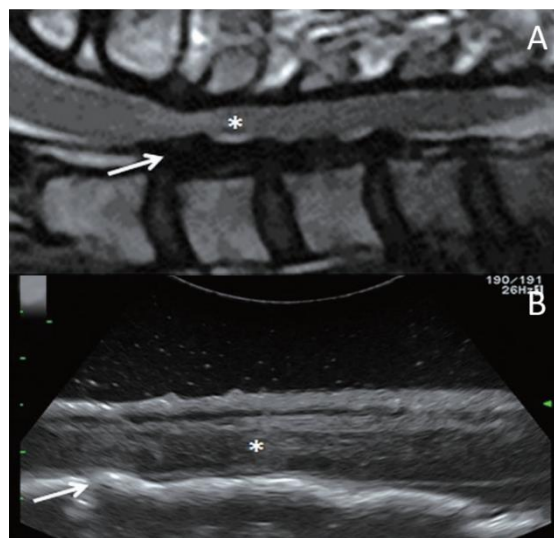


Figure 12 - A: Preoperative MRI showing the spinal cord (asterisk) squashed into into a very narrow spinal canal (arrow). B: IoUS imaging following laminectomy, showing a satisfactory decompression of the spinal cord. (Adapted from [41])

3. Phantom construction

This chapter presents the creation of the lumbar spine phantom, used as the testing subject throughout the entire project, fulfilling the role of a patient undergoing lumbar surgery.

Before the implementation of any practical work in this project, it was necessary to create a testing subject which allowed to experiment the workflow of an image-guided surgical procedure for pedicle screws placement in the lumbar spine.

This subject consisted in a 3-D model of the lumbar region (T11-12 + L1-5 vertebrae), based on a real CT scan of an adult female. This individual suffered from spondylolisthesis at the L4-L5 level (L4 vertebrae slipping over L5).

3.1. Segmentation

To create a printable 3-D model of a real lumbar spine, first one needs to highlight in the CT scan the regions which correspond to each vertebra. This step, known as segmentation, was performed manually, by identifying the pixels belonging to each vertebra in each CT slice, like shown in Figure 13. This task was performed manually to ensure that the model was as close as possible to the spine of the real subject.

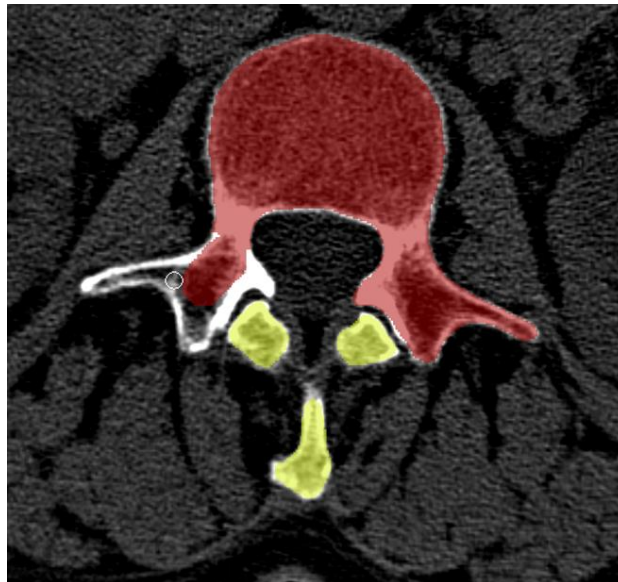


Figure 13 - Vertebrae segmentation by manually painting each vertebra

Segmentation was performed in 3D Slicer (<http://www.slicer.org>), shown in Figure 14, an open source software platform for medical image informatics, image processing, and three-dimensional

visualization [45], using its Segment Editor module, which provides useful segmentation tools and visualization options.

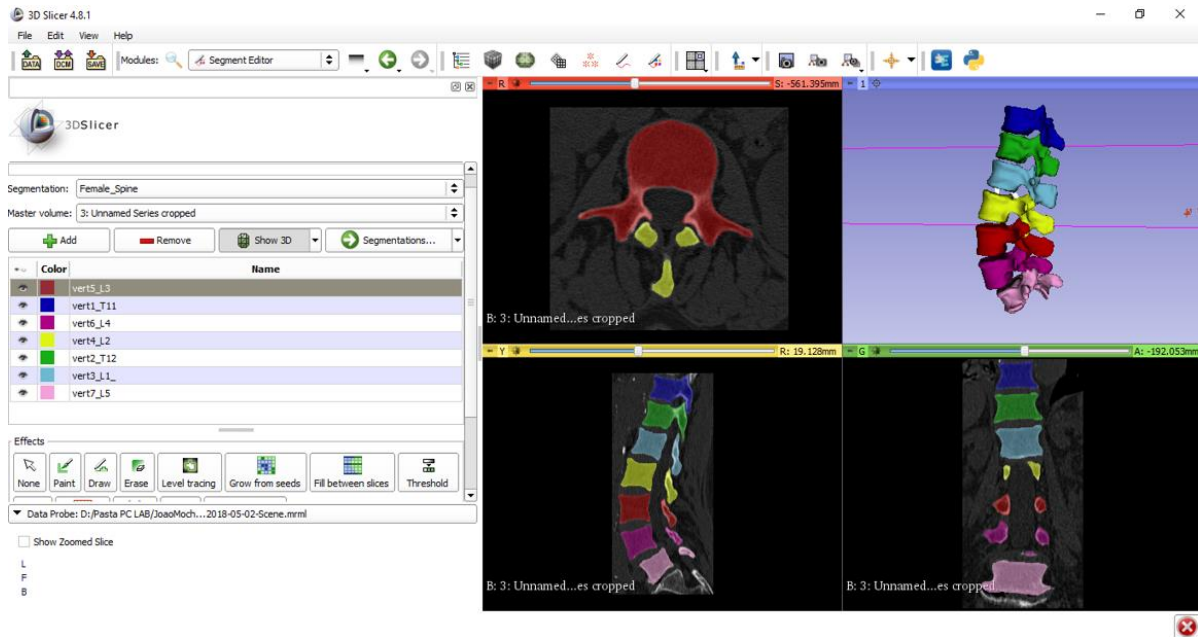


Figure 14 - 3D Slicer workspace with the completed segmentation (note the spondylolisthesis occurring at L4-L5 level, purple and pink vertebrae)

After the segmentation process, a 3-D model of each vertebra was exported as an *.stl* file, which describes the vertices, surfaces and surface normals of the object.

3.2. 3-D Printing

After the segmentation, each vertebra was 3-D printed in a MakerBot' The Replicator (MakerBot Industries, Brooklyn, NY, USA) 3-D printer, using acrylonitrile butadiene styrene (ABS), a tough, light and easy to mold thermoplastic polymer, commonly used in printing filaments, as shown in Figure 15.

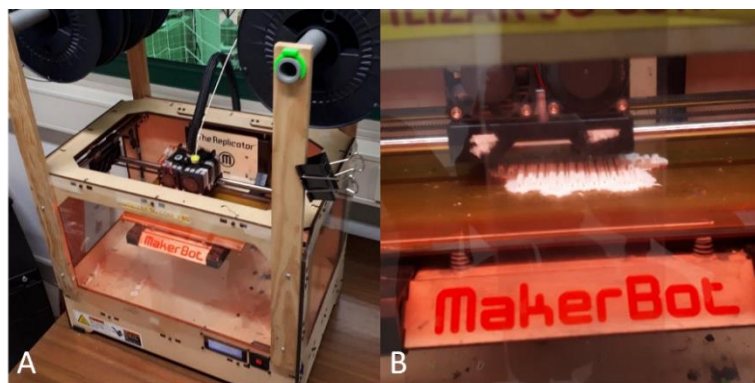


Figure 15 - 3-D printing. A: MakerBot 3-D printer at Pavilhão de Mecânica III (IST). B: Vertebra printing detail

Each vertebra took about 3 hours to be printed, and after removing some material artifacts, that the printer appends to the object to help the printing process, and sanding, they were dipped in acetone, which softened the rough surfaces of the vertebrae and give them a shiny finish (Figure 16).

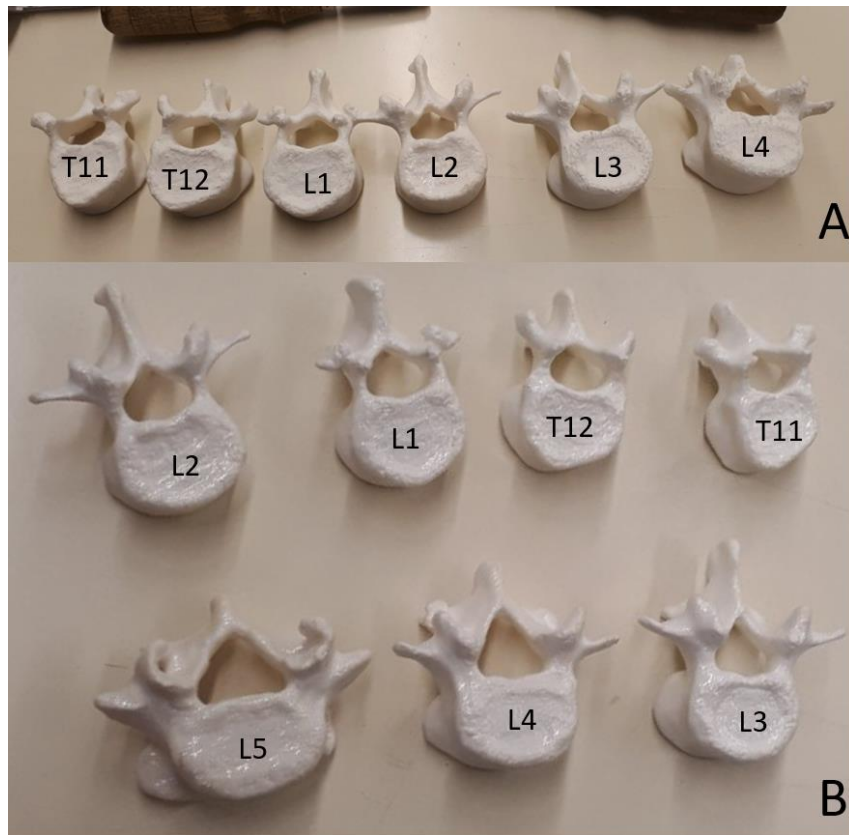


Figure 16 - Printed vertebrae before (A) and after (B) the sanding and the acetone bath (L5 was being printed in A).

3.3. Vertebrae stacking

The next step after the conclusion of each vertebra (bone part of the spine), was to stack them up, creating some soft parts as the intervertebral discs (IVD) and some ligaments.

The IVD were created by placing layers of flexible silicone between the vertebral bodies of adjacent vertebrae. This method allowed the spine model to have some flexibility, like a real lumbar spine, and was made in close relation with the CT data, so that the intervertebral spacing and the spine curvature was as close as possible as the original CT scan.

After the IVD, the ligaments were added, providing more stability while still allowing intervertebral mobility. The only ligaments added were the capsular ligaments, created by inserting a sponge layer between the articular facets of adjacent vertebrae and wrapping the articular processes in a thin layer of silicone.

The spine model was then concluded by inserting a plastic ringed tube in the vertebral foramen from T11 down to L5, to mimic the spinal cord, as shown in Figure 17.

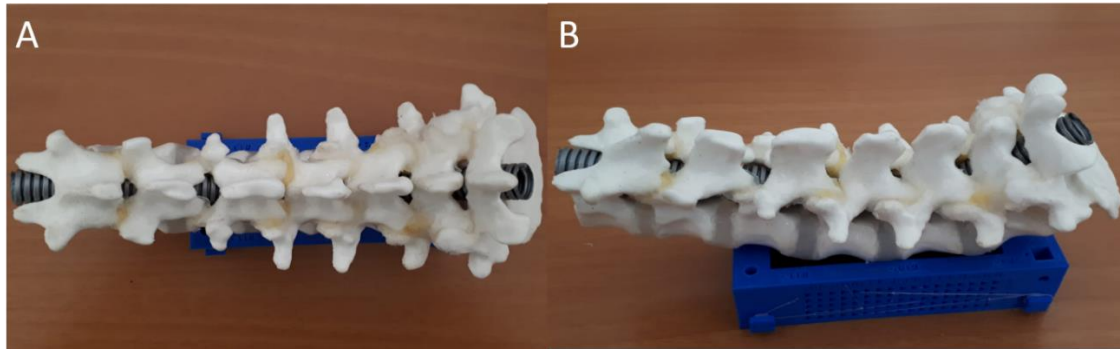


Figure 17 - Complete spine model. A: Posterior view. B: Lateral view (left).

3.4. Phantom conclusion

The last step in the construction of the phantom is to introduce the lumbar model into a material that imitates the rest of the human body structures in that region, namely the skin and the muscles, which presents similar density as them, while also giving it some stability, flexibility and that allow the use of imaging techniques necessary for the realization of the project. The chosen material was a mixture of gelatin, liquid glycerin and water, which was cooked according to the recipe in Appendix A - Gelatine recipe.

The lumbar spine model was placed in a plastic box, with the bottom lined with high density styrofoam, and was then covered with the hot gelatin mixture up to the box surface. The model was placed so that the tops of spinous processes were on average only 1 cm under the surface of the gel.

After staying in the fridge overnight, the mixture solidified, presenting a stronger texture than regular gelatin, similar to human tissues, and allowing CT and ultrasound imaging to be performed to the model, as shown in Figure 18.



Figure 18 - Lumbar spine phantom

4. Methods

Figure 19 shows the possible structure of an ultrasound image-guided surgery for pedicle screw insertion. The patient starts by performing a CT-scan from which a 3-D model of its lumbar spine is created. Then the physician determines the spine injury or disease, the affected vertebrae and plans the trajectory for the pedicle screws placement. Intraoperatively, the physician starts by acquiring the tracked ultrasound data, creating a new 3-D model of the lumbar spine based on the intraoperative US data. The two 3-D models, CT-derived and US-derived, are merged using a registration algorithm, allowing the navigation system to show the CT-planned trajectories in the intraoperative coordinate system (COS).

This chapter presents a detailed explanation of the methods used in each step of this workflow, based on the structure of the surgical procedure presented.

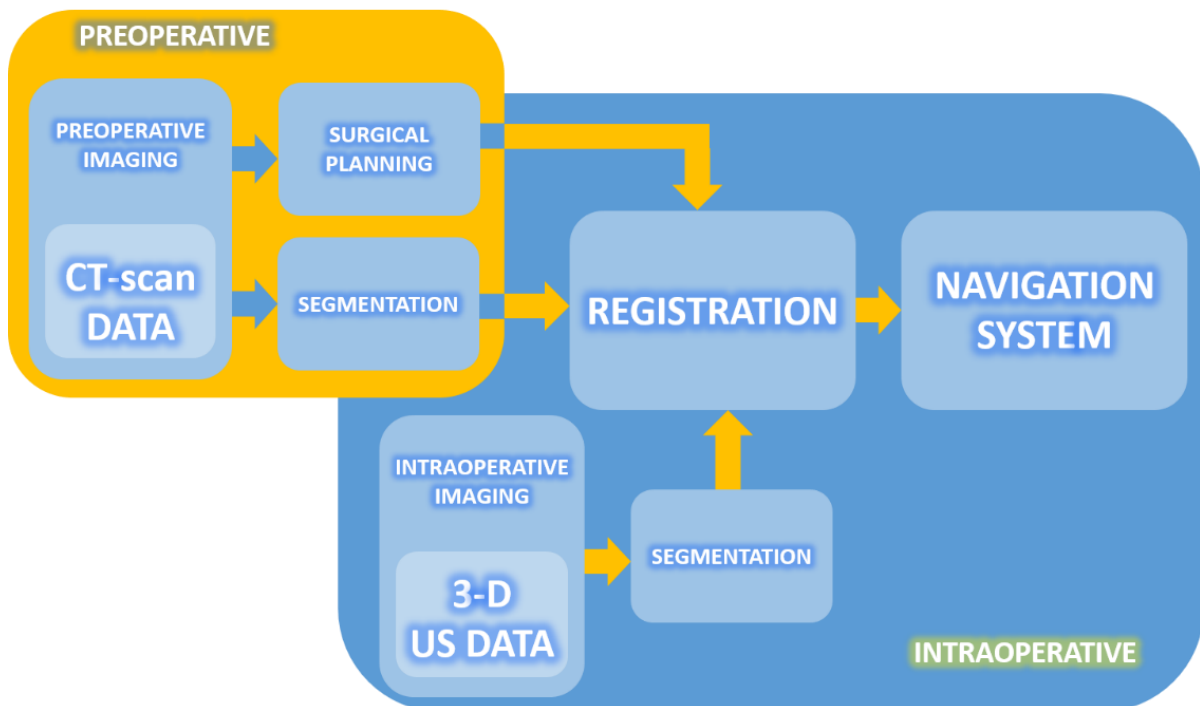


Figure 19 – Proposed structure of an US image-guided surgery for pedicle screw placement.

4.1. CT-scan

The first step of our IG procedure was to perform a CT-scan to the lumbar spine phantom at Hospital de Santa Maria, in a Philips Brilliance CT 64-slice (Koninklijke Philips N.V., Amsterdam, Netherlands). In a CT-scan, a defined number of equally spaced axial slices are acquired using X-ray radiation, allowing the reconstruction of volumetric data. This CT-scan was then exported in a Digital Imaging and

Communications in Medicine (DICOM) format. The DICOM file contained a 768x768x266 3-D matrix, where each element corresponds to a voxel (a 3D pixel) with fixed height, weight and depth in *mm*. The value of each voxel corresponds to the opacity to X-rays of the material that voxel represents, measured in Hounsfield units. Along with the voxels, the DICOM file includes meta-data with useful information, such as the voxels sizes in mm, the distance between adjacent axial slices, the CT-scan coordinate system (COS), the date and time of the CT-scan and other information about the CT device and the CT-scan parameters.

Figure 20 shows the computed tomography images, where it is possible to observe a good contrast between the different materials, although these present some differences from a CT of a real human body, as will be discussed in 6.1. All the 266 axial slices of the CT-scan can also be seen in Video 1 of the Thesis web page [46].

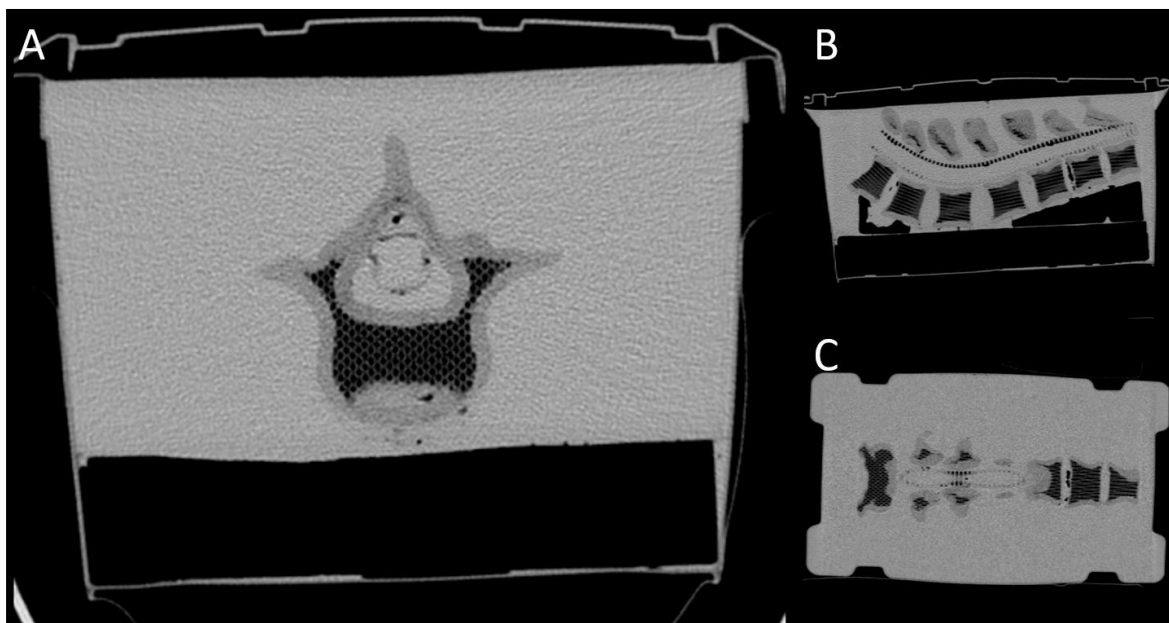


Figure 20 - CT-scan of the Lumbar spine phantom: axial (A), sagittal (B) and coronal (C) slices.

4.1.1. CT segmentation

The segmentation process was performed in 3D Slicer (<http://www.slicer.org>) as the segmentation for the phantom creation, but using a different, quicker method. This was possible because the phantom CT data was simpler than the real female subject data, due to the absence of internal organs, and had a greater contrast between different materials.

4.1.1.1. Thresholding

We started by applying a threshold to the CT data, choosing a minimum and maximum limit and considering that voxels whose intensity lie between that range should be classified as part of the phantom vertebrae (Figure 21).

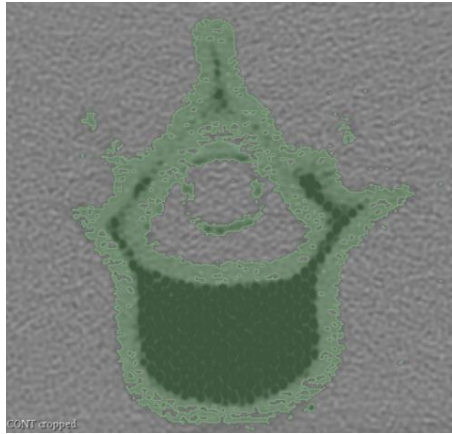


Figure 21 – Segmentation after applying the threshold.

4.1.1.2. Island tool

In the threshold step, some voxels corresponding to gelatin were misclassified as vertebrae, and it was necessary to erase those outliers. Using the Island tool in 3D Slicer, all the voxels classified as vertebrae which are not connected to the main segment are erased (Figure 22).

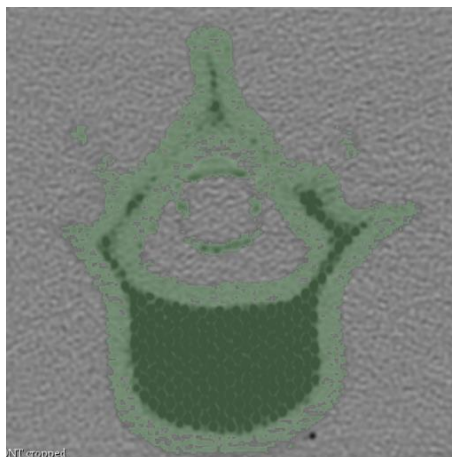


Figure 22 – Segmentation after applying the island tool.

4.1.1.3. Manual finishing

The last step of the segmentation process was to manually erase some voxels that still were misclassified, even after the two previous semi-automatic steps, because they mainly represented the plastic ringed tube, which was made in a similar material as the phantom's vertebrae and was touching them. It was also necessary to manually fill some voxels that were not highlighted, smoothing the contours of the segmentation, and identify the interfaces between adjacent vertebrae, to separate them in different models (Figure 23).

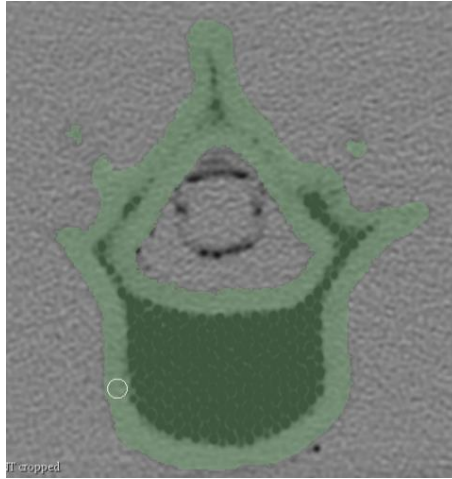


Figure 23 - Segmentation after the manual finishing.

The segmentation process resulted in seven vertebrae models (T11-12 and L1-5), which were again exported as an .STL file.

4.1.2. Surgical Planning - GUI

To perform the surgical planning, a graphical user interface (GUI) was created in MATLAB®. This GUI allowed to open the DICOM files to visualize the CT data, load the vertebrae 3-D models and visualize them in the CT-scan COS. Then, it allows to graphically choose the insertion point of the pedicle screw and its orientation while the user visualizes the intersections between the screws and the CT slices.

The location and orientation of the pedicle screws were chosen according to medical orientation, with the insertion in a region slightly inferior to the intersection between the transverse process and the superior articular process, in the posterior projection of the pedicles. The orientation was chosen so that the screw passes through the pedicle as close as possible to its center.

For this work, we planned the insertion of pedicle screws in the L2, L3 and L4 vertebrae. This vertebrae were chosen because they present the closest shape to a typical lumbar vertebra.

Figure 24 and Figure 25 show the process of planning the placement of pedicle screws in the L3 vertebra, using the created GUI. This process can also be seen in Video 2 [46]. The steps for the

planning, as shown in these figures, are: DICOM loading (A, B, C), segmentation loading (D, E, F), choosing the vertebra (G), choosing the insertion point and direction for the screw for the right screw (H, I, J), loading the screw model (K, L), visualizing the intersection between the screw and the CT slices and correcting the screw orientation (M), repeating the process for the left screw (N) and save the plans (O, P,Q).

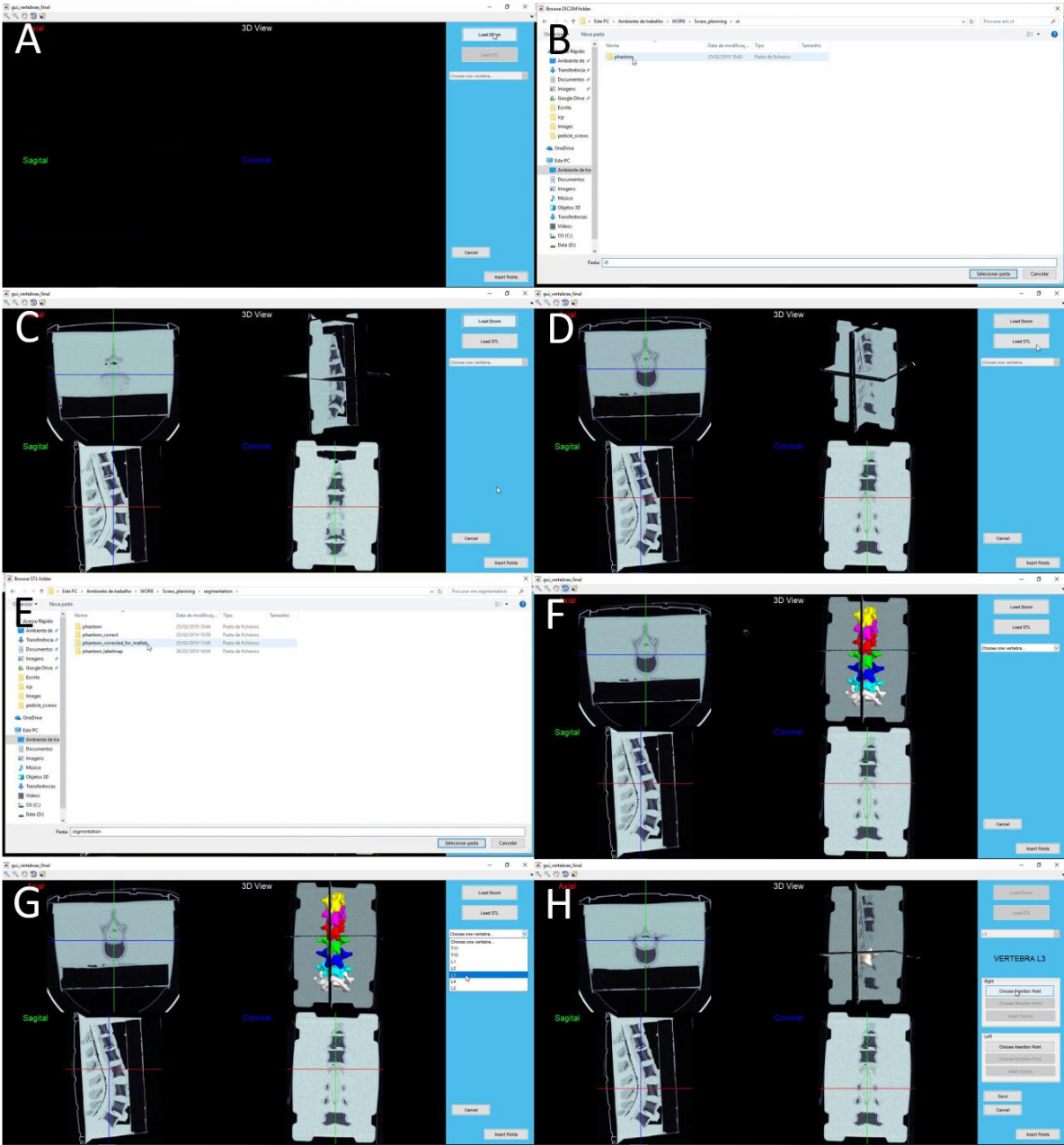


Figure 24 - Surgical planning process for placing pedicle screws in L3 vertebra.

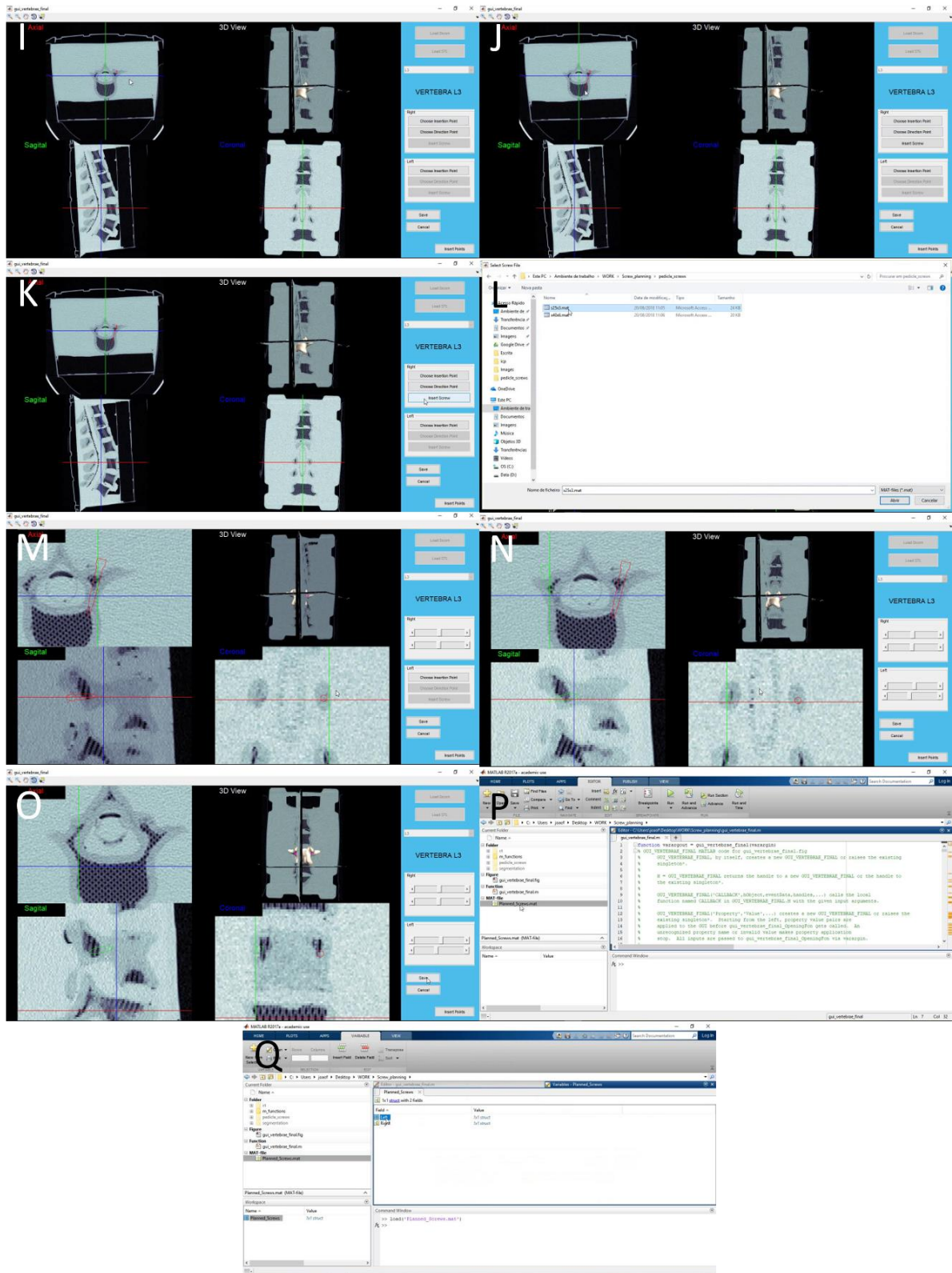


Figure 25 - Surgical planning process for placing pedicle screws in L3 vertebra (continuation).

4.1.3. CT-data post-processing

As will be presented in section 4.3, the registration methods used in this work can merge two sets of points – Point Clouds (PC) – one derived from the CT-scan and the other derived from the US-data. Since the US-data was acquired in the back, from a posterior approach, the US-derived PC corresponds only to the posterior regions of the lumbar spine. Having this in consideration, only the same parts of the vertebrae must be the CT-derived PC, allowing to increase the registration performance and accuracy. To identify these regions, we scanned the columns of each slice of the segmented CT, highlighting the first pixel of the segmentation, which correspond to the posteriormost portions, as shown in Figure 26.

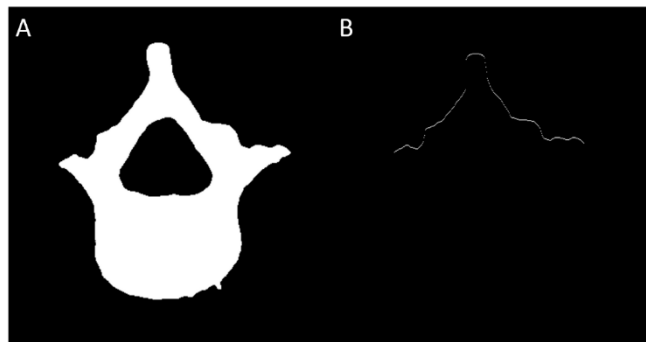


Figure 26 - CT-derived model processing. A: CT segmentation. B: CT segmentation after column scanning (US reaching regions).

Using this method, two CT-derived PC were created. One with the points corresponding to all the vertebrae and one with only the points corresponding to the L3 vertebrae.

4.2. Freehand 3-D Ultrasound imaging

The freehand 3-D Ultrasound imaging, one of the key steps in this project, allows to compute a 3-D volume based on a US scan. This is possible by recording a large set of 2-D US frames while the US probe's location in the intraoperative COS is being tracked, allowing to match the US data with its corresponding position in the intraoperative space. This section presents the detailed explanation of this method, from the devices used, the calibration process, to the acquisition of the US data and its segmentation.

4.2.1. Devices

4.2.1.1. Passive Polaris Spectra System

Passive Polaris Spectra System (Northern Digital Incorporated, Waterloo, Ontario, Canada), shown in Figure 27, is a mobile system equipped with a pair of infrared sensors that are able to “track the 3D position and orientation of active or passive markers attached to surgical tools with advanced optical measurement technology that delivers exceptional accuracy and reliability” [47] within a field of view.



Figure 27 - Passive Polaris Spectra System

Passive markers, the only markers used in this project, are infrared reflecting spheres that must always be facing the Polaris system without obstacles, so their position can be tracked. They can be rigidly attached to tools, in groups of three or more, laid in different geometries, so that Polaris can keep track of different tools simultaneously, without confusing them.

To perform the 3-D US imaging calibration and acquisition, we only used two tracked tools, shown in Figure 28. One was rigidly attached to the US probe and the other was used as a pointer, essential for the calibration process.

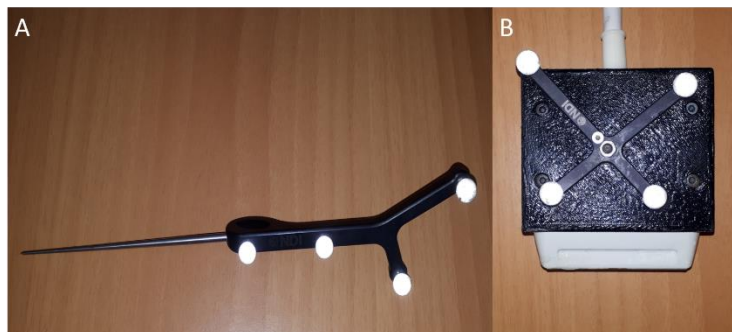


Figure 28 - Polaris passive tools. A: Pointer. B: Tool attached to the US probe.

4.2.1.2. ProSound 2 US system

The Ultrasound system used in this project was a ProSound 2 (Hitachi Aloka, Mitaka, Tokyo, Japan), present in Figure 29, available in the Surgical Robotics Lab (SRL) at Pavilhão de Mecânica III (IST). Connected to the ProSound 2, the UST-586-5 transducer, from the same manufacturer, was the responsible for the emission of the US waves of 3.75-7.5 MHz and the detection of their eco, allowing the acquisition of 2-D linear US images in any spatial orientation.

To attach the Polaris tool to the US probe we used a 3-D printed cover, to avoid damaging the probe.



Figure 29 - ProSound 2 US system with the UST-586-5 transducer

4.2.1.3. Computer with Stradwin

The calibration and acquisition procedures were made in a desktop running Stradwin (<http://mi.eng.cam.ac.uk/~rwp/stradwin>), an experimental, research software and a “tool for freehand 3D ultrasound calibration, acquisition, measurement and visualization” [48] which was compatible with the position tracking system and the US system available.

Since the ProSound 2 US system lacked a digital output for the US images, a frame grabber had to be used. A frame grabber, shown in Figure 30, is a device whose input is an analogical video signal, as presented in the US system screen, and that outputs digital images via USB to the computer. In other words, it is a device that takes screenshots of the US system at a specific frame rate, converts the analogical images to digital and transmits them to Stradwin.



Figure 30 – Frame grabber with video input (yellow) and USB output.

4.2.1.4. Final setup

In Figure 31 it is presented the final device setup used to acquire the US images and compute a 3D US-based volume.



Figure 31 - Freehand 3-D Ultrasound imaging device setup

Through the details presented in Figure 32, it is possible to understand all the different existing COS in the acquisition of the 3-D Ultrasound volumes in this project: the Polaris system COS (Polaris) which represents the intraoperative COS, the US probe COS (probeUS) and the US frame COS (frameUS) and all the transformations between each COS.

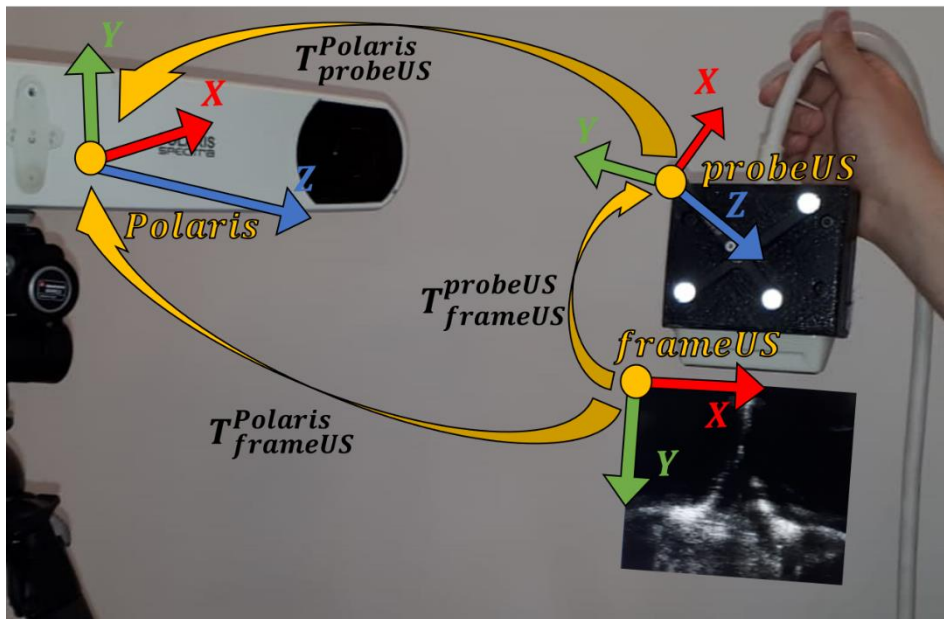


Figure 32 - Freehand 3-D Ultrasound existing COS and transformations between them.

The transformation from COS B to COS A is represented by a 4x4 matrix T_B^A where:

$$T_B^A = \begin{bmatrix} R_B^A & \vec{t}_B^A \\ 0 & 0 & 0 & 1 \end{bmatrix} \quad (1)$$

R_B^A is the 3x3 rotation matrix between the two COS and \vec{t}_B^A is the 3x1 translation vector from the origin of COS B to the origin of COS A.

To compute the 3D US-derived volume it is imperative to know the intraoperative position of each pixel of an US image, in other words, it is necessary to know the transformation between the frameUS COS and the Polaris COS, $T_{frameUS}^{Polaris}$. Since the Polaris system can only track the tool attached to the probe and not the image acquired by it, $T_{frameUS}^{Polaris}$ is indirectly computed by

$$T_{frameUS}^{Polaris} = T_{probeUS}^{Polaris} * T_{frameUS}^{probeUS} \quad (2)$$

where $T_{probeUS}^{Polaris}$ is known by the Polaris system and $T_{frameUS}^{probeUS}$ must be calculated in a process known as Probe calibration.

4.2.2. Probe calibration

As mentioned in the previous subsection, probe calibration allows to compute the transformation between the US probe and the US acquired image. There have been several studies about this topic, but the usual approach is to scan a phantom, an object whose dimensions are known, that place constraints on the eight calibration parameters necessary to fully define the transformation matrix: two image scales (S_u and S_v , the x scale and y scale, respectively), three translations (t_x , t_y and t_z , in the x, y and z directions, respectively, defining the translation vector $\vec{t}_{frameUS}^{probeUS}$) and three rotations (α , β and γ , about the z, y and x axes, respectively, defining the rotation matrix $R_{frameUS}^{probeUS}$) [49].

Many different phantoms can be used to perform the probe calibration, which include a simple plane [50], a 2-D alignment phantom [51], Z-fiducial phantom [52] and wire phantoms [53], that place the constraints needed to solve the calibration parameters iteratively or algebraically.

The Stradwin software, used for the US part of this project, includes a probe calibration feature that uses the tip of the Polaris Pointer tool as a calibration phantom, avoiding the need of printing a complex phantom, while allowing to calibrate with an error similar to the state of the art Z-fiducial phantom [49].

Before starting the calibration process, and since the Polaris system can only track the pointer tool and not its tip, we needed also to compute the position of the tip in the pointer COS, performing a method called pivoting.

4.2.2.1. Pointer pivoting

Pointer pivoting, shown in Figure 33, consists in finding the translation of the tip of the pointer in the coordinate system of the pointer tool. To perform this step the tip must be pinned to a stationary point, while the pointer tool is rotated in a cone shape around the tip, in an angle between 30 and 60 degrees from the vertical axis. After several position acquisitions (around 100 for best convergence),

the Stradwin software computes the offset of the pointer tip, by trying to calculate a point equidistant to all the pointer tool positions acquired by the Polaris system.

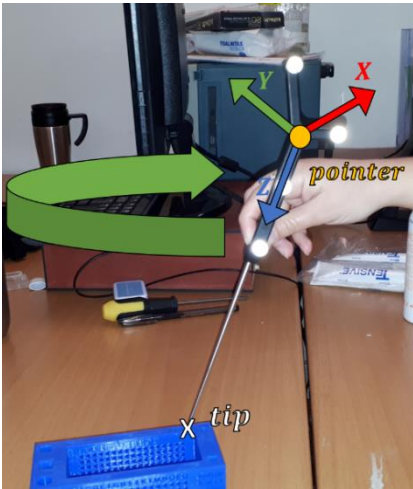


Figure 33 - Pointer pivoting.

4.2.2.2. Calibration

After the pivoting step, probe calibration could be performed. Figure 34 shows the device setup used in the probe calibration process, as well as the COS and transformations involved in this process. The US images in this task were acquired in a water bath with a known temperature, granting a material in which the US waves can propagate. Knowing the water’s temperature allows Stradwin to make a necessary and automatic calibration correction, due to the differences in sound velocity in water at different temperatures and its velocity inside body tissue.

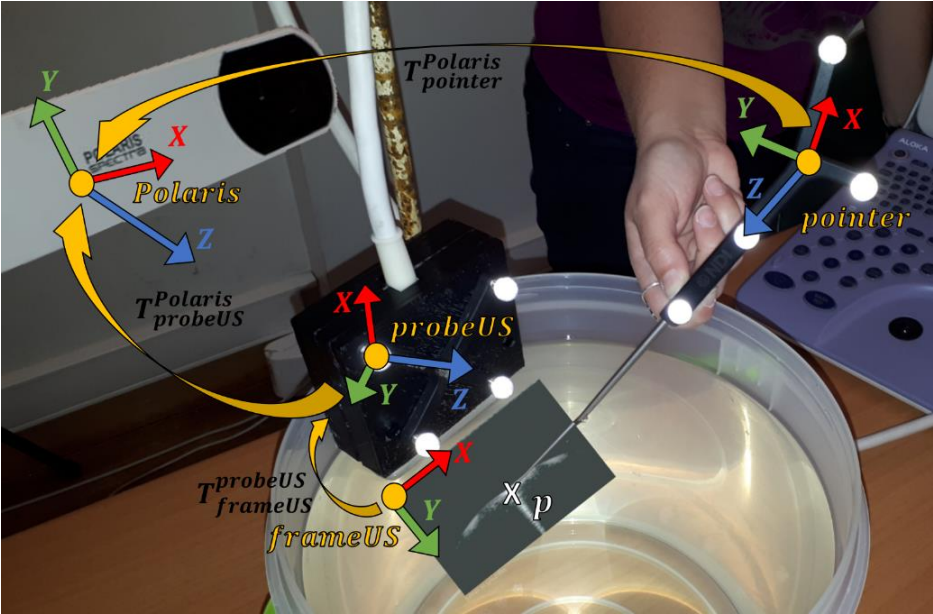


Figure 34 - Probe calibration. Detail of the existing COS and transformations between them.

During the probe calibration, we scanned a set of points p_i with the US system. Those points result from placing the pointer's tip in the B-mode plane, creating a bright spot in the US images, which are automatically segmented by Stradwin, as shown in Figure 35.

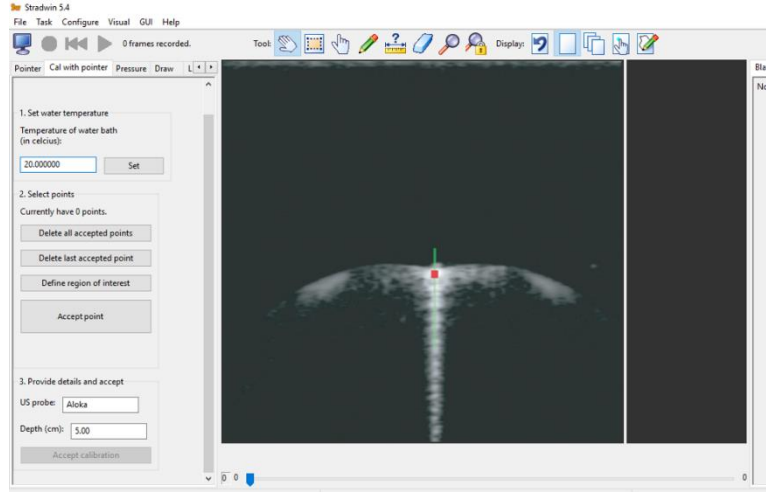


Figure 35 - Stradwin interface during probe calibration. The tip of the pointer is automatically segmented as the brighter pixel in the US frame.

This segmentation returns $p_i^{frameUS'} = (u_i, v_i, 0)^T$, where u_i and v_i are the column and row indices of each point p_i in the US frame. These points, in pixels, are converted to metric units by a scaling factor

$$T_{scale} = \begin{bmatrix} s_u & 0 & 0 \\ 0 & s_v & 0 \\ 0 & 0 & 0 \end{bmatrix} \quad (3)$$

where s_u and s_v are the scaling factors in millimeters per pixel, to compute the segmented points in the frameUS COS, $p_i^{frameUS}$. These points can then be computed in the Polaris COS by

$$p_i^{Polaris} = T_{probeUS_i}^{Polaris} * T_{frameUS}^{probeUS} * T_{scale} * p_i^{frameUS'} \quad (4)$$

where $T_{probeUS_i}^{Polaris}$ is the transformation between the probeUS COS and Polaris COS at the moment of the acquisition of p_i and is given by the Polaris system, $p_i^{frameUS'}$ results from the automatic US image segmentation performed by the Stradwin software, and $T_{frameUS}^{probeUS}$ and T_{scale} are unknown.

In other hand, since the segmented points came from the pointer's tip, and therefore their 3-D location is the same, there is another way of computing them in the Polaris COS, which is given by

$$p_i^{Polaris} = T_{pointer_i}^{Polaris} * p^{pointer} \quad (5)$$

where $T_{pointer_i}^{Polaris}$ is the transformation between the pointer COS and Polaris COS at the moment of the acquisition of p_i and is given by the Polaris system and $p^{pointer}$ is the constant offset of the tip in the pointer COS and results from the pointer pivoting.

Equating (4) and (5), we get

$$T_{pointer_i}^{Polaris} * p^{pointer} = T_{probeUS_i}^{Polaris} * T_{frameUS}^{probeUS} * T_{scale} * p_i^{frameUS'} \quad (6)$$

which, after locating a minimum of three noncollinear p_i , allow to perform the probe calibration by minimizing

$$\min \sum_i \left| T_{probeUS_i}^{Polaris} * T_{frameUS}^{probeUS} * T_{scale} * p_i^{frameUS'} - T_{pointer_i}^{Polaris} * p^{pointer} \right| \quad (7)$$

where $||$ denotes the Euclidean norm on \mathbb{R}^3 . Stradwin automatically minimizes the previous equation using the iterative Levenberg-Marquardt algorithm, computing $T_{frameUS}^{probeUS}$ and T_{scale} [48],[53].

The calibration parameters were computed and saved after the acquisition of ten points scattered in all the US image, in order to obtain a good convergence in all the B-scan area.

The parameters computed by this probe calibration method work only for one specific US image depth, as the pixel to millimeters scale changes based on the acquired depth. So, it is important to recalibrate every time this US setting is changed.

4.2.3.Acquisition

After performing the probe calibration process, we started the acquisitions by scanning the surface of our lumbar spine phantom. To ensure an efficient propagation of the US waves, we placed a conductor gel in the tip of the probe, eliminating the air between the probe and the phantom and decreasing the acoustic impedance. The conductor gel used was the Quick-Eco Gel® (LESSA - AB MEDICA GROUP, S.A., Barberà del Vallès, Barcelona, Spain).

A group of five US volumes were acquired in this project: three scans of the entire length of the phantom with the US probe acquiring axial frames and two scans of the L3 vertebra with the US probe acquiring perpendicular to the axial plane and performing a slightly radial movement. The first scan was acquired medially, with the center of the US probe aligned with the vertebrae' spinous processes. The second and third scans were acquired with the center of the US probe aligned with the left articular processes and right articular processes, respectively, as seen in Figure 36.

The two L3 scans were acquired in the right side of the vertebra, as seen in Figure 37. These single vertebra acquisitions were performed with the objective of performing registration using just one

vertebral model, because although each vertebra is a single rigid body, they perform movements relative to each other, and this problem can only be overcome by registering a single vertebra.

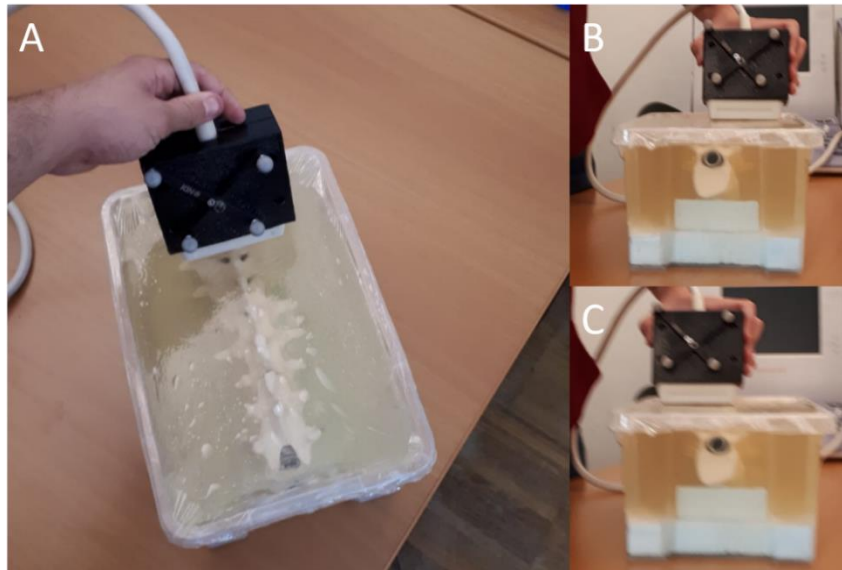


Figure 36 – Axial acquisitions of the entire length of the phantom: medially (A), left (B), right (C).

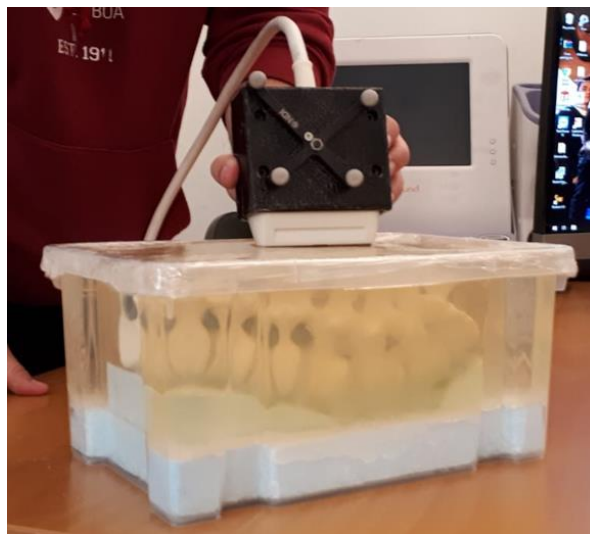


Figure 37 - Sagittal acquisitions at the level of L3 right side.

All the US acquisitions were performed with the same US settings, an image depth of 50 mm, US waves of 7.5 MHz and a gain of 64.

4.2.3.1. Output files

Finishing each acquisition, the 3-D US data is saved. Stradwin allows to export the US frames and the information about the COS transformations in different formats, but the chosen ones were .JPEG, to save each US frame, and .SW, a Stradwin base format, which is essentially a text format with all the

information regarding the calibration parameters, the number of frames recorded, the recording time or the transformations for each image.

4.2.4. US segmentation - GUI

After the acquisition of the intraoperative US volumes, it was necessary to extract useful information from them, that could be used to match with the CT-based points, and so it was necessary to perform segmentation of the US data.

For the segmentation of the acquired US images, another MATLAB® GUI was created. This GUI, shown in Figure 38, allowed to load the .SW file and each of the .JPEG US frames, to define the segmentation region of interest (ROI) and the initial and final frames and to perform the segmentation.

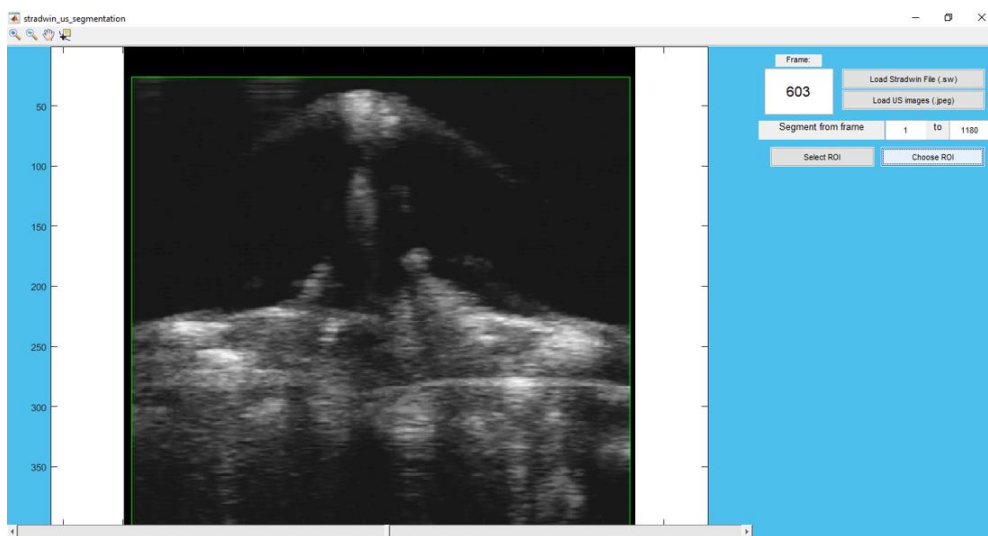


Figure 38 - US segmentation GUI

4.2.4.1. Filtering

Since US imaging is characterized by the presence of noise, the segmentation process starts by applying a filter to the US frames. The filter used was a median filter [55] with a 5x5 kernel, which computes each pixel of the filtered image as the median value of the pixels in a 5x5 window centered in that same pixel. This filter was chosen because it allows to reduce the high frequency noise but without distorting too much the contours of the objects, unlike a gaussian lowpass filter (Figure 39).

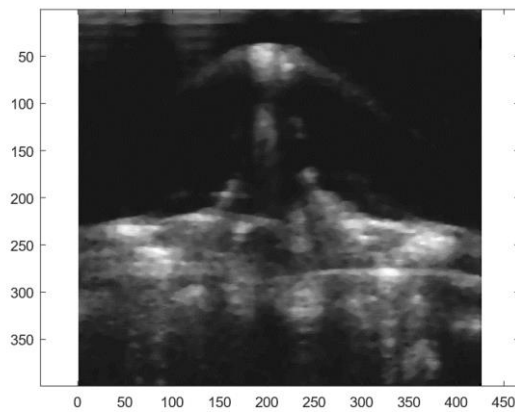


Figure 39 - US segmentation after applying the median filter.

4.2.4.2. Thresholding

After filtering the data, the contours of the vertebrae must be highlighted, identifying the highest intensity pixels of the US frames. These regions correspond to the borders of the vertebrae, because in US imaging B-Mode the abrupt differences in acoustic impedance between the gelatin and the ABS polymer of the vertebrae model are translated in brightness. Setting a threshold, we were able to highlight all the pixels above a user-defined intensity value, which correspond to real gelatin-vertebra interface (Figure 40).

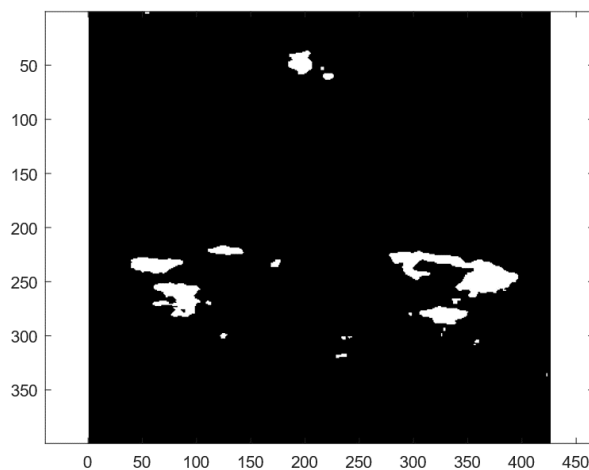


Figure 40 - US segmentation after applying the threshold.

4.2.4.3. Column scanning

To conclude the segmentation process, it was performed a scan of the columns of all the US frames' ROI, to identify the posteriormost pixels, since we only cared for the posterior surface of the vertebrae (Figure 41).

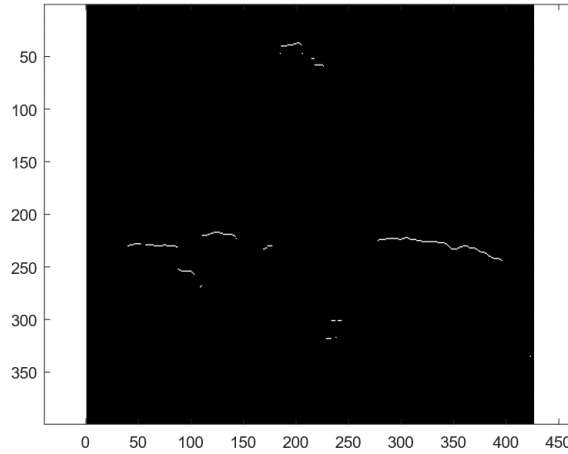


Figure 41 - US segmentation after performing the column scanning.

4.2.4.4. Transformation

After completing the US image segmentation, which resulted in a set of highlighted pixels in each US frame, these points were transformed to the Polaris COS by applying the scale factors, the transformation matrix computed in probe calibration step $T_{frameUS}^{probeUS}$ and the transformation matrix of the US probe at the time that each frame was recorded $T_{probeUS_i}^{Polaris}$, according to equation (4). This step resulted in a Point Cloud (PC) with the US-derived lumbar spine model, which could then be matched with the CT-derived PC.

4.3. Registration

After acquiring the preoperative and intraoperative images of the lumbar spine, the data derived from the two imaging modalities must be merged, through finding the transformation between the CT COS and the Polaris COS. The registration is the central piece of any image-guided (IG) procedure and allows to compute the preoperative surgical plans in the intraoperative COS, guiding the surgeon to the desired trajectories.

4.3.1. Registration algorithms

As seen in chapter 2.2.3, there are different registration methods, depending on the type of data, applications and available devices. In this project, as our objective was to match a US-derived Point Cloud (PC) with a CT-derived PC, we used a combination of active registration methods, the pair-points and surface matching.

The first step of our registration methodology was to manually identify a set of vertebral landmarks (fiducials) in the two types of correspondent PC, which were matched using Kabsch algorithm. The result of this step was then used as the initial estimation to perform the surface matching step, for which we used the Iterative Closest Point (ICP) algorithm. All the registration process was computed using MATLAB® built-in functions and other functions available in MathWorks® File Exchange, namely the Kabsch algorithm, by Ehud Schreiber [56].

4.3.1.1. Kabsch algorithm

Proposed in 1976 by Wolfgang Kabsch [57], the algorithm commonly known by the name of its author consists in a method for finding the transformation which best relates two sets of vectors. To apply this algorithm there must be correspondence between each vector from the first set with each vector from the second set. Since there is correspondence between each vector set, the translation part of the transformation comes down to the difference between their centroids, leaving only the rotation part to be computed.

Being P and Q two sets of vectors, represented as $N \times 3$ matrices, where each row corresponds to the coordinates of each vector in \mathbb{R}^3 ,

$$P = \begin{pmatrix} x'_1 & y'_1 & z'_1 \\ x'_2 & y'_2 & z'_2 \\ \vdots & \vdots & \vdots \\ x'_n & y'_n & z'_n \end{pmatrix} \quad Q = \begin{pmatrix} x_1 & y_1 & z_1 \\ x_2 & y_2 & z_2 \\ \vdots & \vdots & \vdots \\ x_n & y_n & z_n \end{pmatrix} \quad (8)$$

the steps for computing the rotation matrix which rotates P into Q are:

1. Calculating the cross-covariance matrix H .

$$H = P^T Q \quad (9)$$

2. Calculating the singular value decomposition (SVD) of H .

$$H = USV^T \quad (10)$$

3. Computing the rotation matrix R .

$$R = V \begin{bmatrix} 1 & 0 & 0 \\ 0 & 1 & 0 \\ 0 & 0 & \det(VU^T) \end{bmatrix} U^T \quad (11)$$

4.3.1.2. Iterative Closest Point algorithm

Unlike Kabsch algorithm, the ICP algorithm, introduced in 1992 by Paul Besl and Neil McKay [58], is employed to relate two sets of points without the need of a correspondence between each point, which means that the two data sets may not even have the same number of points. ICP computes the transformation which best relates two PC by iteratively minimizing the root mean square of the metric distance between the points of the two data sets. ICP usually converges to a local minimum which may not correspond to the ideal transformation that align one PC to another, so it is very important to give the algorithm a good initial transformation. In this project, the initial transformation which must be refined by the ICP algorithm was the result from the Kabsch algorithm.

Being Q a fixed PC with M points – $Q = \{\vec{q}_1, \vec{q}_2, \dots, \vec{q}_M\}$, $\vec{q}_m \in \mathbb{R}^3$ – commonly known as reference, and P another PC with N points – $P = \{\vec{p}_1, \vec{p}_2, \dots, \vec{p}_N\}$, $\vec{p}_n \in \mathbb{R}^3$) – known as source, that must be transformed to best match the reference, the steps for computing the transformation matrix which aligns P into Q are:

1. Calculating for each point of P the closest point in Q , matching each \vec{p}_n with its closest \vec{q}_m .
2. Computing the transformation T – combination of a 3x3 rotation matrix R and a translation vector \vec{t} – which minimizes the sum of the squared distance between each pair of matching points,

$$\min \sum_{n=1}^N |T * \vec{p}_n - \vec{q}_m|^2 = \min \sum_{n=1}^N |R * \vec{p}_n + \vec{t} - \vec{q}_m|^2 \quad (12)$$

using a Least Squares approach.

3. Transform the source data set P with the computed transformation T ,

$$P_{i+1} = T_i P_i = R_i P_i + \vec{t}_i \quad (13)$$

4. Verify the stopping criteria, which can be a maximum number of iterations or the difference between consecutive computed transformations, T_i and T_{i+1} .
5. Iterate all the process, in case the stopping criteria was not met.

4.3.2. Data registration

Registration of our data started after visualizing each of the two corresponding PC in a MATLAB® 3D plot and manually selecting three non-collinear pairs of matching points in these plots, three points in the CT-derived PC and three points in the US-derived PC. This step is completely user dependent, since the correct identification of matching fiducials in the CT data and US data depend only in the user skill. To improve matching points selection, these fiducials were chosen in easy to identify vertebral structures, such as the transverse and the spinous processes.

These points were then registered using the Kabsch algorithm, resulting in the transformation matrix $T_{Polaris}^{CT^*}$, which best aligns the fiducials identified in the US-derived PC with the ones identified in the CT-derived PC. Multiplying the computed matrix by the US data, we are transforming the US-derived PC from the Polaris COS to a first approximation of the CT COS, denoted by CT* COS.

After computing the new positions of the US-derived PC, these were registered with the CT-derived PC using the ICP algorithm as explained previously, resulting in a last transformation $T_{CT^*}^{CT}$ which refines the alignment of the US data in the CT data.

The result of the registration process is the transformation $T_{Polaris}^{CT}$, which sets the correspondence between the CT COS and the Polaris COS

$$T_{Polaris}^{CT} = T_{CT^*}^{CT} * T_{Polaris}^{CT^*} \quad (14)$$

4.4. Navigation System

The navigation system is the culmination of the presented work, where all the gathered data and the computed transformations are merged to display real-time visual guidance to the surgeon who is performing the insertion of the pedicle screws.

The navigation system created for this project is a simple MATLAB® graphical user interface (GUI), which allows to display the lumbar spine, the surgical plans and the Polaris tools in the intraoperative COS – the Polaris COS. For this, it receives as inputs the CT-derived PC, the surgical plans performed in the CT COS, which include the insertion points and orientations for every pedicle screw we want to place, and the transformation matrix from the Polaris COS to the CT COS – $T_{Polaris}^{CT}$, as computed in the registration process.

After loading these data, it computes the transformation matrix from the CT COS and the Polaris COS, for displaying the CT-derived PC and the surgical plans in the Polaris COS. This transformation is the inverse of the matrix which transforms from the Polaris COS to the CT COS,

$$T_{CT}^{Polaris} = (T_{Polaris}^{CT})^{-1} \quad (15)$$

Using $T_{CT}^{Polaris}$, the CT-derived PC and the surgical plans are displayed in the Polaris COS.

To assist the surgery, each pedicle screw plan is exhibited as a red cone with the vertex in its insertion point. The cone's axis of symmetry is aligned with the planned orientation vector.

Then, it is possible to initialize the real-time visualization of the surgical tools. The navigation system communicates with the Polaris system and gets the information about the tools positions and orientations. Although it is possible to track any instrument that has a group of Polaris markers attached, the presented navigation system only tracks the Polaris pointer.

When the connection with the Polaris system is achieved, the navigation system displays in real-time the pointer's position and orientation in the Polaris COS. The pointer referential is exhibited as a red dot and the pointer itself is a blue line.

To help the surgeon reach the desired pedicle screw's placement, each one of the cones of the surgical plans turn from red to green when the Polaris pointer's tip is inside the correspondent cone and it is aligned with its axis of symmetry.

5. Results

This chapter presents all the results obtained throughout each step of the developed methodology, with the same structure it was presented in the previous section. Starting with the results of the segmentation of the lumbar phantom CT-scan, through the surgical planning performed in the CT, the US calibrations, the different acquisitions of US volumes and, finally, the results of the registration. To help visualizing the results of this work, a web page was created with some videos of them [46].

5.1. CT-scan

5.1.1. CT segmentation

The segmentation of the phantom CT-scan resulted in seven 3D models, corresponding to the vertebrae T11, T12, L1, L2, L3, L4 and L5, which are presented in Figure 42 to Figure 49.

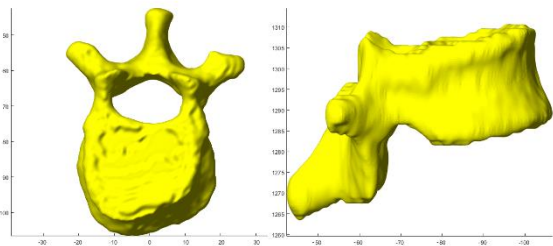


Figure 42 - Superior and lateral (right) view of T11 vertebra 3D model (axes scales in mm).

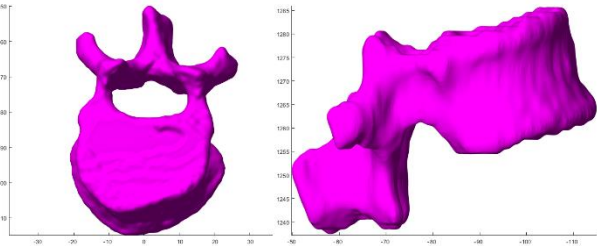


Figure 43 - Superior and lateral (right) view of T12 vertebra 3D model (axes scales in mm).

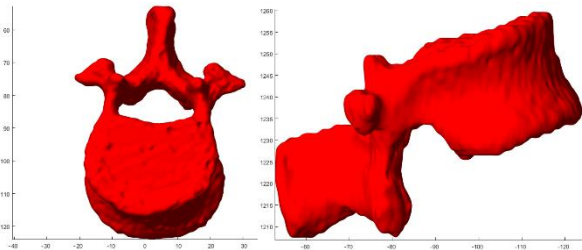


Figure 44 - Superior and lateral (right) view of L1 vertebra 3D model (axes scales in mm).

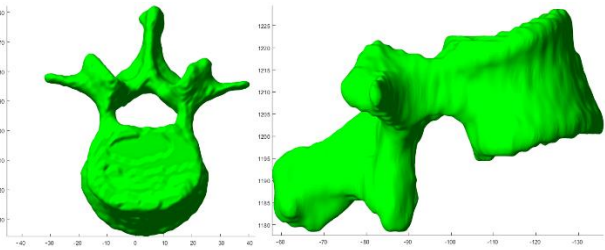


Figure 45 - Superior and lateral (right) view of L2 vertebra 3D model (axes scales in mm).

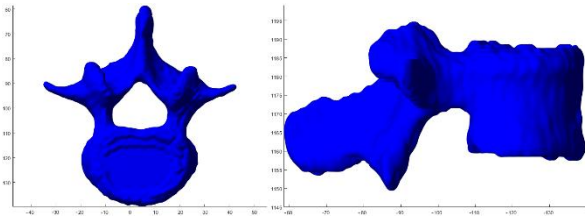


Figure 46 - Superior and lateral (right) view of L3 vertebra 3D model (axes scales in mm).

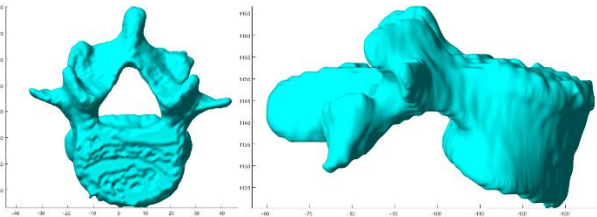


Figure 47 - Superior and lateral (right) view of L4 vertebra 3D model (axes scales in mm).

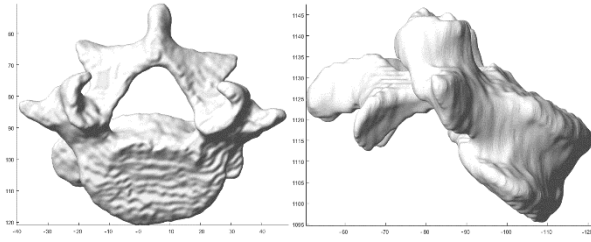


Figure 48 - Superior and lateral (right) view of L5 vertebra 3D model (axes scales in mm).

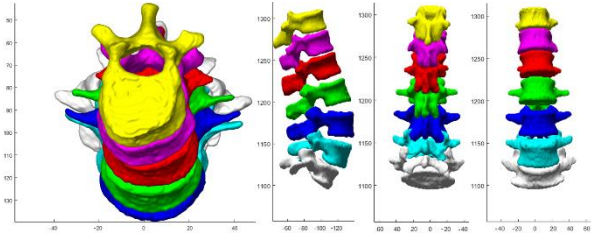


Figure 49 - Superior, lateral (right), posterior and anterior view of the seven vertebrae 3-D modes (axes scales in mm).

The models shown in these figures are represented in the CT-scan COS, since the location of each vertex of the 3-D models is computed in this coordinate system during the segmentation process, using the information contained in the DICOM file metadata.

5.1.2. Surgical planning

After performing the CT segmentation, the positions and orientations for placing the pedicle screws in the L2, L3 and L4 vertebrae were planned in the MATLAB® GUI, as explained in subsection 4.1.2. Table 1 shows the coordinates of the insertion points and the directions, given by unit vectors, which were planned for each screw, in the COS of the CT-scan, and a previsualization of the planning is present in Figure 50.

Table 1 – Coordinates of the insertion points and directions for the planned pedicle screws.

Vertebra	LEFT		RIGHT	
	Insertion Point (mm)	Direction	Insertion Point (mm)	Direction
L2	(20.41 , -82.97 , 1206.07)	(-0.236 , -0.924 , 0.300)	(-13.22 , -81.26 , 1207.07)	(0.213 , -0.943 , 0.257)
L3	(23.26 , -90.38 , 1181.07)	(-0.266 , -0.964 , 0)	(-14.93 , -89.24 , 1178.07)	(0.248 , -0.969 , 0)
L4	(25.54 , -89.81 , 1153.07)	(-0.293 , -0.939 , -0.179)	(-17.21 , -88.67 , 1150.07)	(0.261 , -0.963 , -0.061)

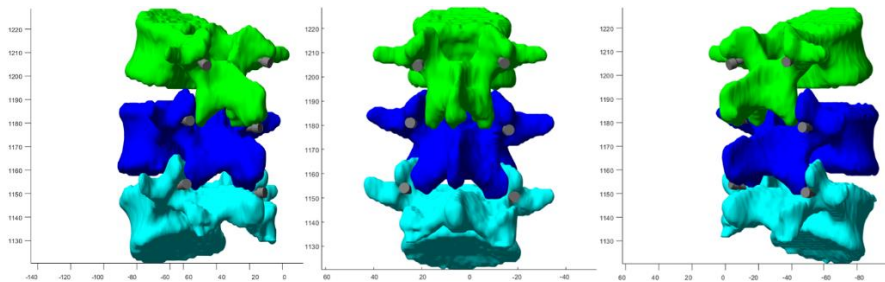


Figure 50 – Posterior view (left, medial and right) of the L2, L3 and L4 vertebrae with each pedicle screw in their planned locations.

5.1.3. CT-data post-processing

The two point clouds extracted from the CT-data are presented in Figure 51 and Figure 52. These PC resulted from scanning the columns of the segmented CT-scan and were then used in the registration process, to merge with the US-derived PC. These PC can also be seen in Video 3 and Video 4 [46].

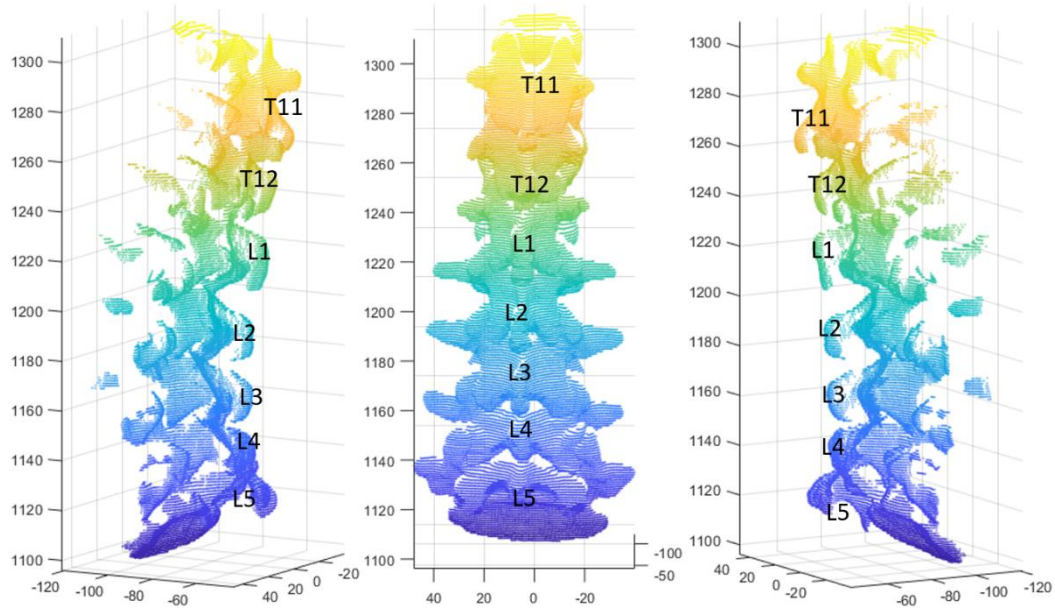


Figure 51 - Point Cloud of the posteriormost regions of all the vertebrae (Video 3).

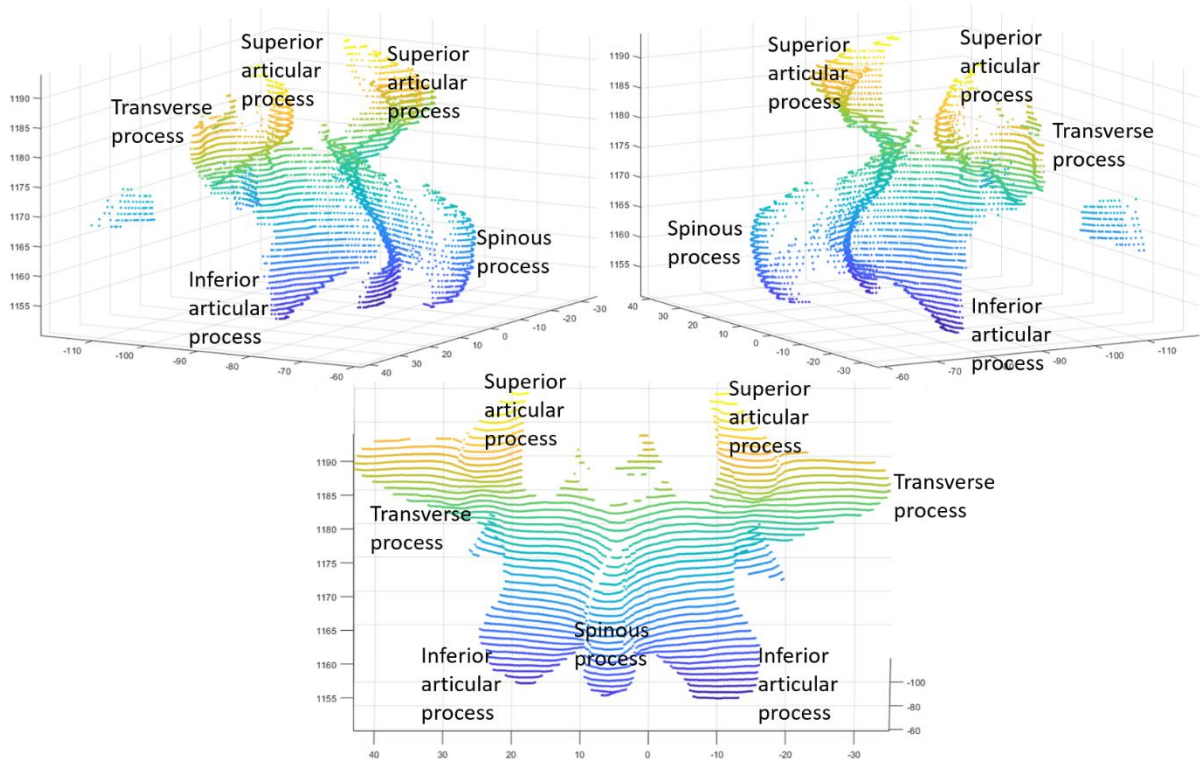


Figure 52 - Point Cloud of the posteriormost regions of the L3 vertebra (Video 4).

5.2. Freehand 3-D Ultrasound imaging

5.2.1. Calibrations

In this subsection, the results of the performed calibrations are presented. The pointer pivoting was repeated five times and the result with the smallest Root Mean Square Error (RMSE) was used to perform the probe calibration. This task was also repeated five times and, again, the result with the smallest RMSE was used to perform the Freehand 3-D Ultrasound imaging acquisitions. The results and the associated RMSE were presented in Stradwin software interface after completing each calibration.

5.2.1.1. Pointer pivoting

Table 2 presents the results of the tip position, in the Pointer ROS and the respective error of each pointer tip calibration. The highlighted result was the one used to perform the next calibration step.

Table 2 – Results of the pointer pivoting step and corresponding error.

<i>Pointer pivoting</i>	<i>Tip position (mm)</i>	<i>RMSE (mm)</i>
1	(-17.60 , 1.11 , -156.29)	0.61
2	(-17.33 , 1.49 , -156.81)	0.56
3	(-17.45 , 1.26 , -156.44)	0.52
4	(-17.27 , 1.07 , -157.30)	0.37
5	(-17.11 , 1.53 , -159.54)	0.47

5.2.1.2. Probe calibration.

Table 3 presents the results of each probe calibration parameter - s_u , s_v , t_x , t_y , t_z , α , β and γ -, the error in each coordinate axis and the RMSE for each probe calibration performed. The highlighted result was the one used to perform all the US acquisitions. All the probe calibration process was performed with US image depth of 50 mm.

Table 3 – Results of the probe calibration step and corresponding error.

Probe calibration	CALIBRATION PARAMETERS								Error			
	S_u (mm/ pixel)	S_v (mm/ pixel)	t_x (mm)	t_y (mm)	t_z (mm)	α (°)	β (°)	γ (°)	x (mm)	y (mm)	z (mm)	RMS (mm)
1	0.122	0.116	-33.56	-21.10	-34.27	-92.63	-45.39	265.03	0.39	0.42	0.73	0.57
2	0.119	0.112	-35.72	-20.58	-37.03	-90.91	-43.75	267.13	0.22	0.38	0.81	0.48
3	0.126	0.120	-34.19	-21.06	-36.62	-91.70	-43.34	268.28	0.23	0.31	0.65	0.44
4	0.130	0.122	-34.84	-23.20	-36.44	-95.86	-41.69	266.67	0.28	0.32	0.77	0.54
5	0.125	0.129	-36.11	-24.77	-35.65	-93.12	-42.55	268.48	0.24	0.45	0.64	0.49

Figure 53 shows a qualitative result of the best probe calibration achieved, where Stradwin was able to identify the pointer's tip purely based on the Polaris data and the probe calibration, without any kind of tip segmentation. The presented images were shot from the Stradwin interface, and show the differences in the calibration convergence when the tip is closer to the US probe (A) and when it is more distant B. These differences will be explained in the next chapter.

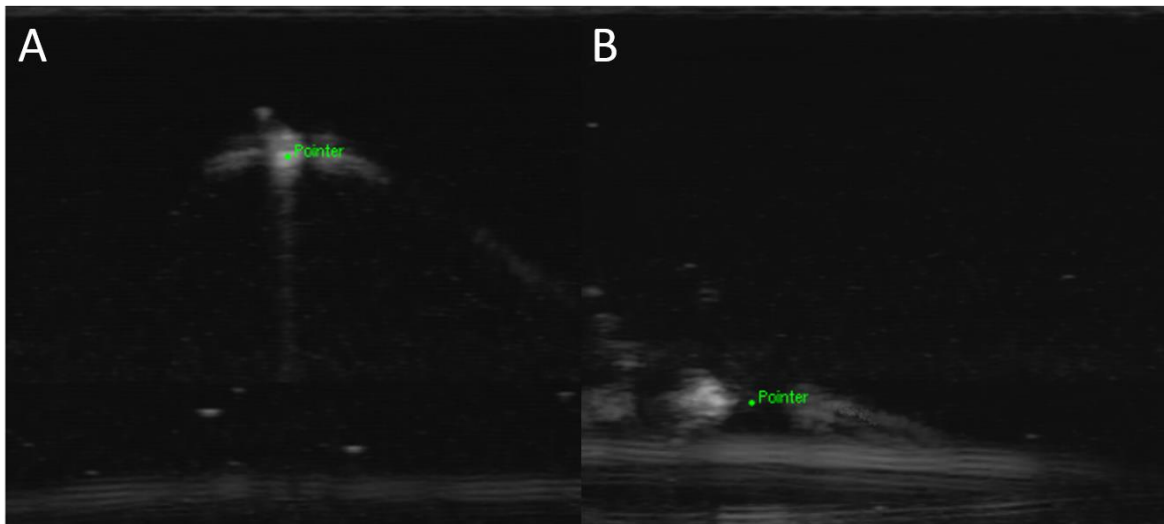


Figure 53 - Calibration result. In this figure, the pointer's tip is identified based on the Polaris data and not based on image segmentation. A: Tip close to US probe. B: Tip far from the US probe.

Using the parameters of the calibration with the smallest RMSE, the transformation matrix from the frameUS COS to the probeUS COS, $T_{frameUS}^{probeUS}$, was calculated as

$$T_{frameUS}^{probeUS} = \begin{bmatrix} R_z(\alpha) * R_y(\beta) * R_x(\gamma) & t_x \\ 0 & t_y \\ 0 & t_z \\ 0 & 1 \end{bmatrix} \quad (16)$$

where $R_z(\alpha)$, $R_y(\beta)$ and $R_x(\gamma)$ are the rotation matrices around the z axis by α degrees, y axis by β degrees and x axis by γ degrees, computed as

$$R_z(\alpha) = \begin{bmatrix} \cos \alpha & -\sin \alpha & 0 \\ \sin \alpha & \cos \alpha & 0 \\ 0 & 0 & 1 \end{bmatrix}, R_y(\beta) = \begin{bmatrix} \cos \beta & 0 & \sin \beta \\ 0 & 1 & 0 \\ -\sin \beta & 0 & \cos \beta \end{bmatrix}, R_x(\gamma) = \begin{bmatrix} 1 & 0 & 0 \\ 0 & \cos \gamma & -\sin \gamma \\ 0 & \sin \gamma & \cos \gamma \end{bmatrix} \quad (17)$$

being the resulting matrix

$$T_{frameUS}^{probeUS} = \begin{bmatrix} -0.0216 & -0.0504 & 0.9985 & -34.19 \\ -0.7270 & -0.6848 & -0.0502 & -21.06 \\ 0.6863 & -0.7270 & -0.0218 & -36.62 \\ 0 & 0 & 0 & 1 \end{bmatrix} \quad (18)$$

5.2.2. Acquisitions

Figure 54 presents the results of the five acquisitions made, through a graphical representation of the 3-D US volumes, which were constructed by computing and placing each acquired US frame in the Polaris COS, using the transformations recorded in the Stradwin software output files.

In the first 3-D US acquisition, acquired with the US probe align with the axial plane, from here referred to as full lumbar spine – medial, we acquired 1180 frames, during 57.55 seconds, with a mean acquisition frequency of 20.50 *frames/s*.

In the second one, from here referred to as full lumbar spine – left, we acquired 1165 frames, during 46.72 seconds, with a mean acquisition frequency of 24.94 *frames/s*.

In the third one, from here referred to as full lumbar spine – right, we acquired 1045 frames, during 42.40 seconds and with a mean acquisition frequency of 24.65 *frames/s*.

In the fourth 3-D US acquisition, the first acquisition performed with the probe aligned perpendicular to the axial plane and a slightly radial movement at the right posterior region of the L3 vertebra, from here referred to as L3 vertebra – right (1st), we acquired 759 frames, during 30.40 seconds and with a mean acquisition frequency of 24.97 *frames/s*.

In the last acquisition, from here referred to as L3 vertebra – right (2nd), we acquired 924 frames, during 36.91 seconds and with a mean acquisition frequency of 25.03 *frames/s*.

In every acquisition, the recorded frames had a width of 426 pixels and a height of 399 pixels.

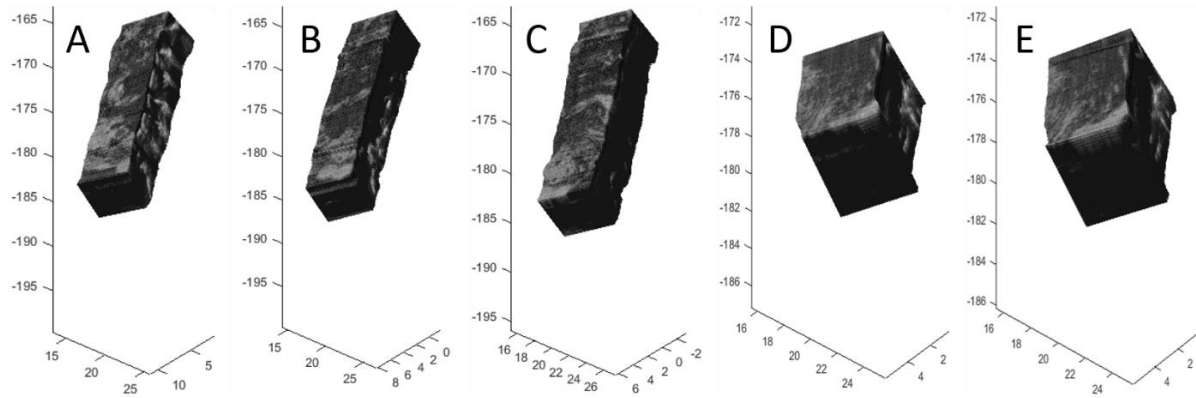


Figure 54 – Visualization of the US frames of each acquisition group, in the Polaris COS. A: full lumbar spine – left (Video 6). B: full lumbar spine – medial (Video 5). C: full lumbar spine – right (Video 7). D: L3 vertebra – right (1st) (Video 8). E: L3 vertebra – right (2nd) (Video 9).

The acquired frames can also be seen from Video 5 to Video 9 [46].

5.2.3. US segmentation

Each acquisition was segmented with the MATLAB® GUI as explained in the previous chapter. The threshold value used to perform the segmentation of all the acquired volumes was 0.35.

The US-derived PC resulting from the segmentation of each US acquisition are presented in this subsection, from Figure 55 to Figure 59. To help visualization, the name of each vertebra was added to the images containing more than one vertebra, near their spinous process. In the segmentation of the two acquisitions of L3, each main feature of the vertebra is identified. The US-derived PC can also be seen from Video 10 to Video 14, respectively [46].

5.2.3.1. Full lumbar spine – medial

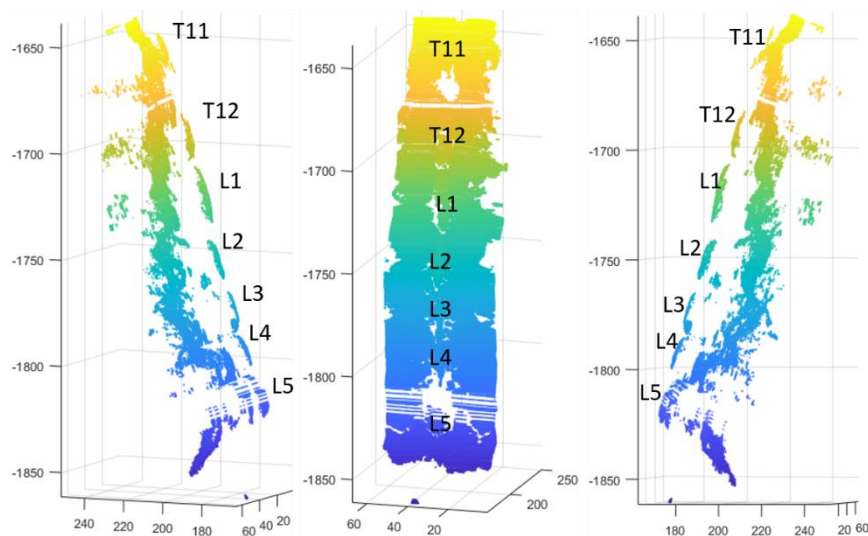


Figure 55 – US-derived PC resulting from the segmentation of the full lumbar spine – medial US acquisition, in the Polaris COS (Video 10).

5.2.3.2. Full lumbar spine – left

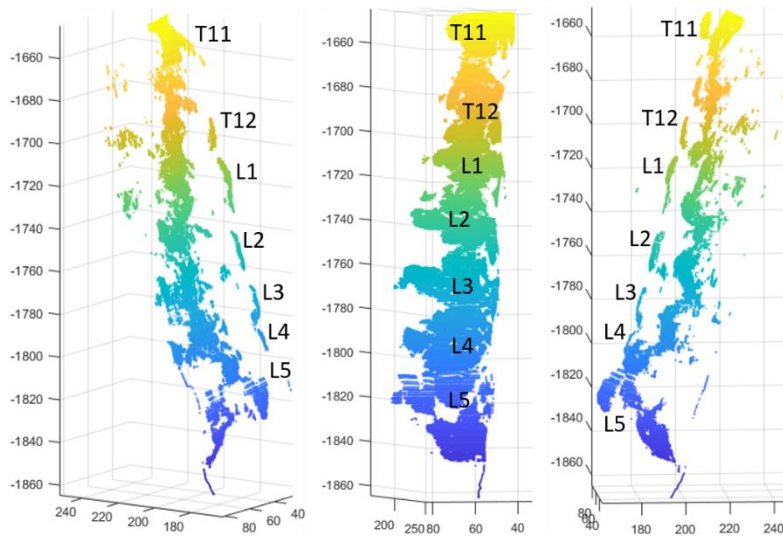


Figure 56 - US-derived PC resulting from the segmentation of the full lumbar spine – left US acquisition, in the Polaris COS (Video 11).

5.2.3.3. Full lumbar spine – right

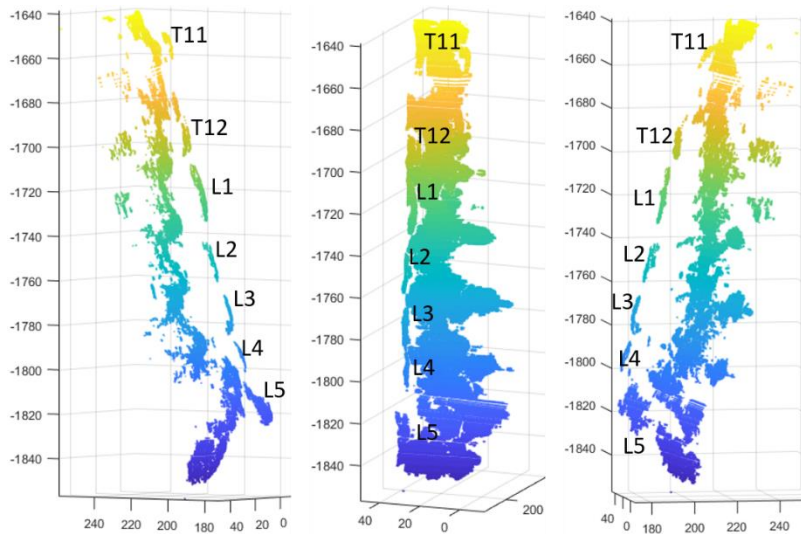


Figure 57 - US-derived PC resulting from the segmentation of the full lumbar spine – right US acquisition, in the Polaris COS (Video 12).

5.2.3.4. L3 vertebra – right (1st)

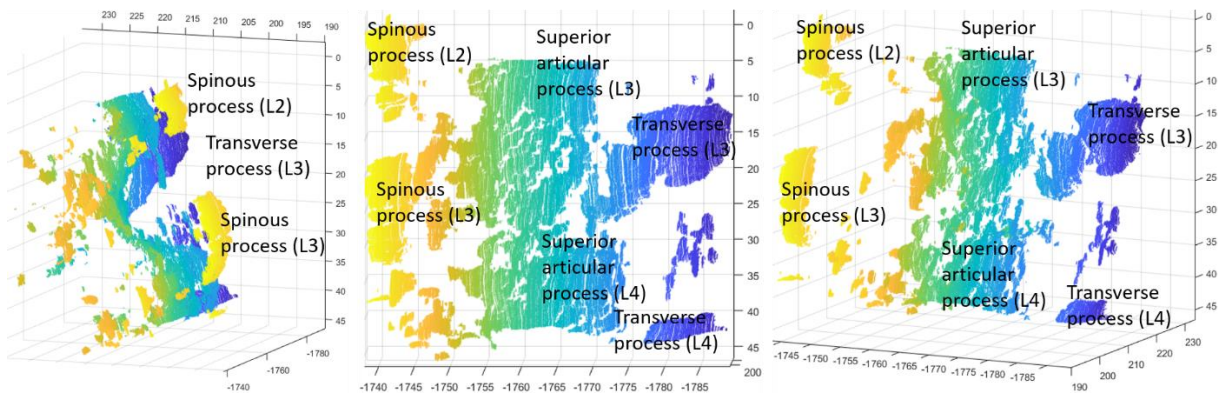


Figure 58 - US-derived PC resulting from the segmentation of the L3 vertebra – right (1st) US acquisition, in the Polaris COS (Video 13).

5.2.3.5. L3 vertebra – right (2nd)

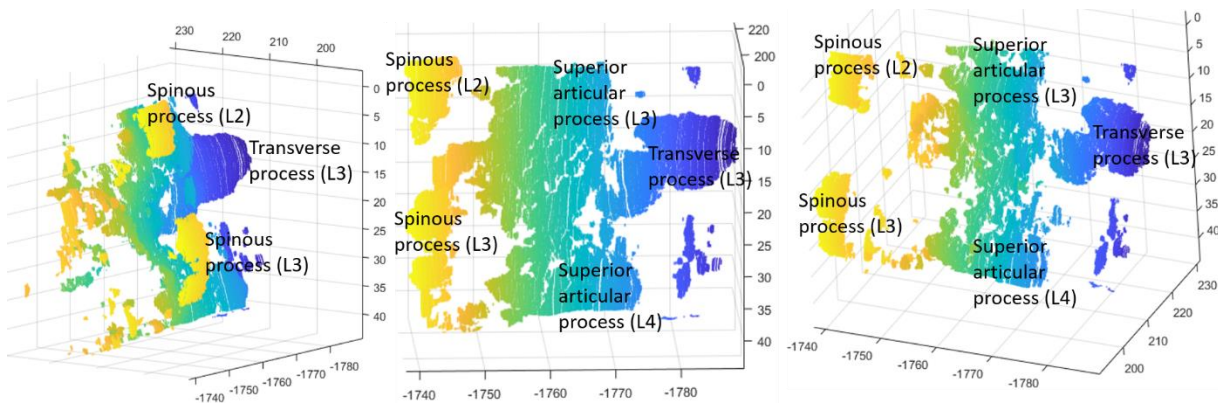


Figure 59 - US-derived PC resulting from the segmentation of the L3 vertebra – right (2nd) US acquisition, in the Polaris COS (Video 14).

5.3. Registration

5.3.1. Algorithms testing

The algorithms presented were tested with a control PC, shown in Figure 60, to verify if it was possible to use them to successfully align the same PC in two different positions and rotations, before using those algorithms to perform the registration of the surgical data. This step was also useful to show how the ICP algorithm may converge to a local minimum which may not be the best solution possible, if it is not given a good initial approximation. The control PC used corresponded to the vertices of the 3-D model of L3 vertebra, which was presented in section 5.1.

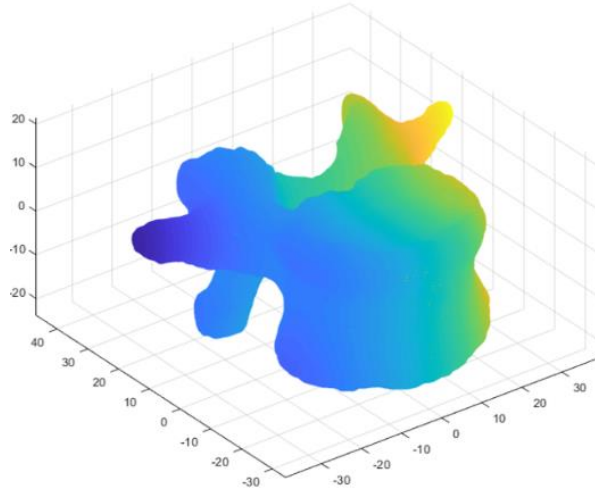


Figure 60 - Control PC (vertices of the L3 3-D model).

The control PC was firstly transformed by applying a rotation of 45° around the x-axis, followed by a rotation of 60° around the y-axis, a rotation of 30° around the z-axis and a translation by $\{40, 30, 80\}$ mm, as presented in Figure 61.

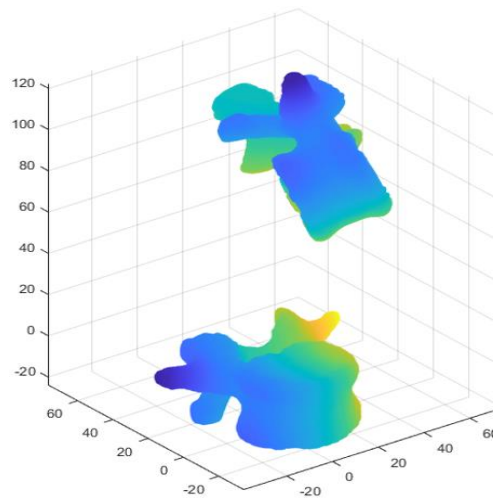


Figure 61 - Original PC (below) and transformed PC (above).

Running the ICP algorithm with the present data resulted in a convergence to a wrong solution, where the PC were still misaligned, has shown in Figure 62.

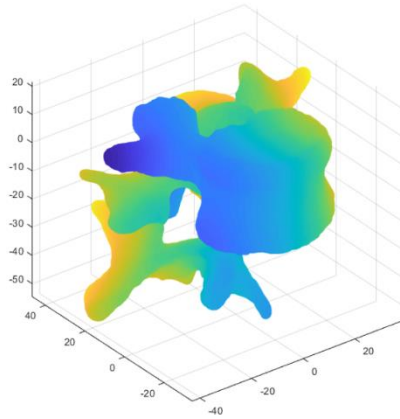


Figure 62 - Result of running the ICP algorithm without initial approximation.

To improve the solution, the two algorithms were used. Primarily, three matching and easy to identify points were selected in each of the L3 PC, the original and the transformed. After this, Kabsch algorithm was used to align those three pairs of points, resulting in an initial approximation between the two PC, which was then improved by the ICP algorithm. Figure 63 shows each step of this method, which resulted in the perfect alignment of the transformed PC with the original.

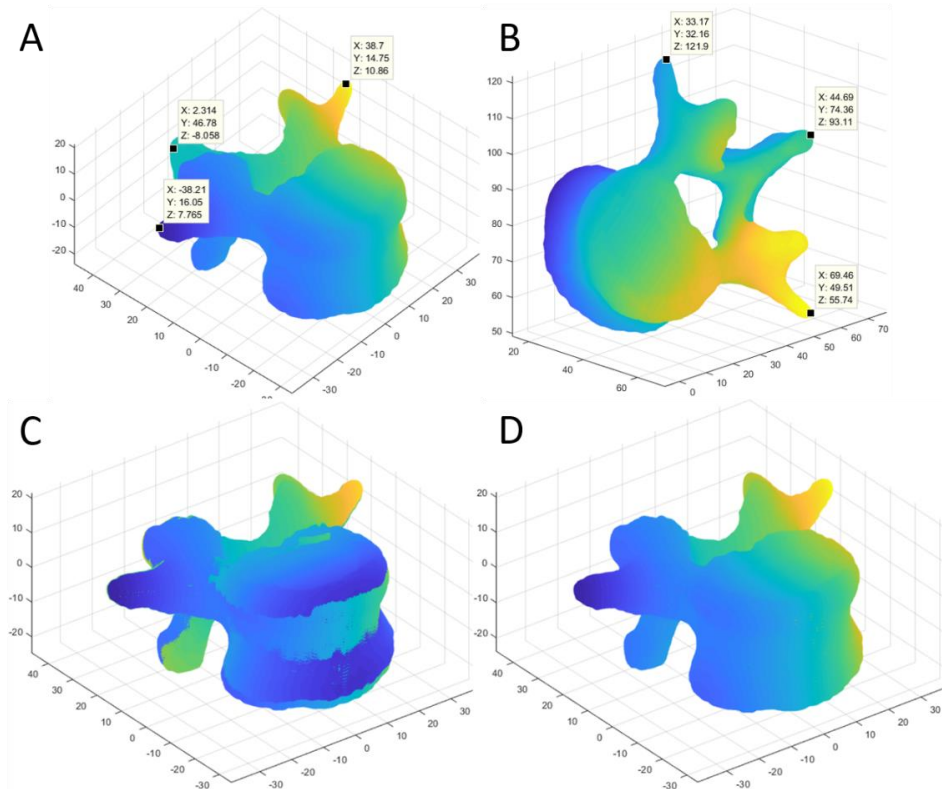


Figure 63 - Final registration method. A: Acquisition of three points in the original PC. B: Acquisition of approximately matching points in the transformed PC. C: Initial approximation which resulted from the Kabsch algorithm. D: Final alignment, after the refinement with the ICP algorithm.

5.3.2. Kabsch algorithm

After performing the segmentation of the US volumes, obtaining the different US-derived PC, these sets of points were merged with the CT-derived data using the registration methods presented in the previous chapter, starting by applying the Kabsch algorithm to compute an initial transformation between the CT and US COS.

In this subsection, the results of the selection of the matching pair-points in the CT-derived and US-derived PC for each dataset are presented in Figure 64, Figure 66, Figure 68, Figure 70, Figure 72 and Table 4, Table 5, Table 6, Table 7, Table 8. The transformation matrices computed by Kabsch algorithm to merge the selected fiducials and their corresponding errors are also presented.

Figure 65, Figure 67, Figure 69, Figure 71 and Figure 73 show the CT-derived PC and the result of applying the computed transformation to each of the US-derived PC. The results of the Kabsch algorithm can also be seen from Video 15 to Video 19, respectively [46].

5.3.2.1. Full lumbar spine – medial

The fiducials which allowed to perform an initial approximation between the full lumbar spine – medial US PC and the CT-derived PC were chosen in the spinous process of L1 and L3 and in the right superior articular process of L3.

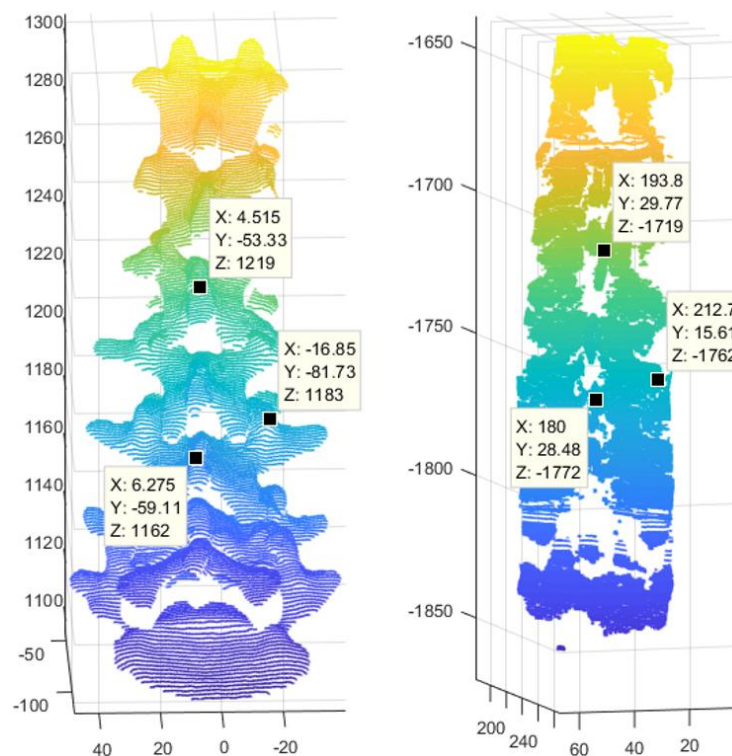


Figure 64 – Selection of the pair-points in CT-derived PC and in the full lumbar spine – medial US PC.

Table 4 – Coordinates of the pair-points (fiducials) selected for the initial approximation between the full lumbar spine – medial US PC and the CT PC.

<i>Fiducial</i>	Position in CT (<i>mm</i>)	Position in US (<i>mm</i>)
1	(-16.85 , -81.73 , 1183.07)	(212.71 , 15.61 , -1762.32)
2	(4.52 , -53.33 , 1219.07)	(193.84 , 29.77 , -1718.69)
3	(6.27 , -59.11 , 1162.07)	(180.04 , 28.48 , -1772.45)

The transformation which best matches the selected points was

$$T_{Polaris}^{CT*} = \begin{bmatrix} -0.310 & 0.950 & 0.033 & 92.566 \\ -0.888 & -0.302 & 0.348 & 724.901 \\ 0.340 & 0.079 & 0.937 & 2760.621 \\ 0 & 0 & 0 & 1 \end{bmatrix}$$

and the RMS of the distance between the transformed pair-points was

$$RMSE = 0.9982 \text{ mm}$$

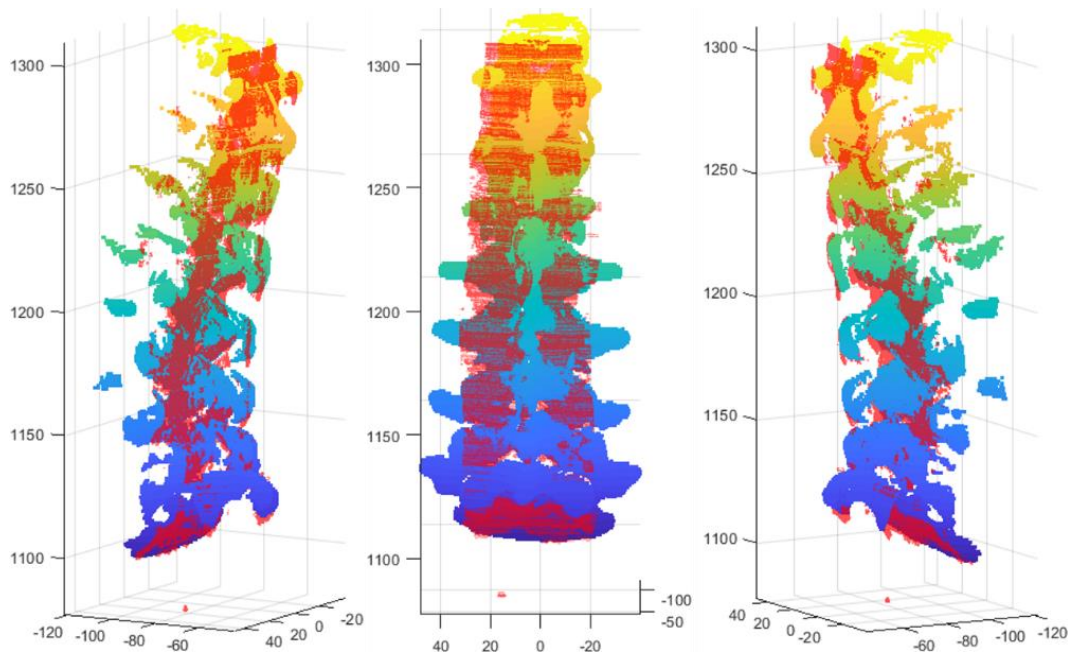


Figure 65 – Superposition of the full lumbar spine – medial US PC after the initial transformation (in semi-transparent red) with the CT-derived PC (Video 15).

5.3.2.2. Full lumbar spine – left

The fiducials which allowed to perform an initial approximation between the full lumbar spine – left US PC and the CT-derived PC were chosen in the spinous process of L1 and L3 and in the left transverse process of L3.

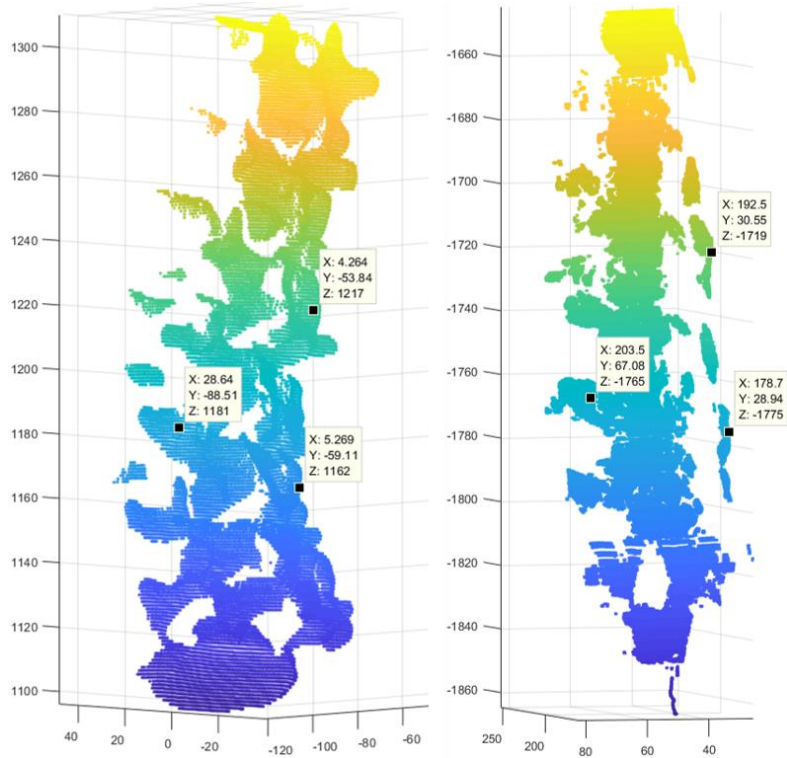


Figure 66 - Selection of the pair-points in CT-derived PC and in the full lumbar spine – left US PC.

Table 5 - Coordinates of the pair-points (fiducials) selected for the initial approximation between the full lumbar spine – left US PC and the CT PC.

<i>Fiducial</i>	Position in CT (mm)	Position in US (mm)
1	(29.65 , -89.52 , 1180.07)	(203.46 , 67.08 , -1765.28)
2	(3.76 , -53.08 , 1219.07)	(192.55 , 30.55 , -1719.50)
3	(6.78 , -58.86 , 1164.07)	(1.78.70 , 28.94 , -1775.22)

The transformation which best matches the selected points was

$$T_{Polaris}^{CT^*} = \begin{bmatrix} -0.404 & 0.913 & 0.050 & 139.931 \\ -0.869 & -0.401 & 0.292 & 627.678 \\ 0.286 & 0.075 & 0.955 & 2804.477 \\ 0 & 0 & 0 & 1 \end{bmatrix}$$

and the RMS of the distance between the transformed pair-points was

$$RMSE = 2.2104 \text{ mm}$$

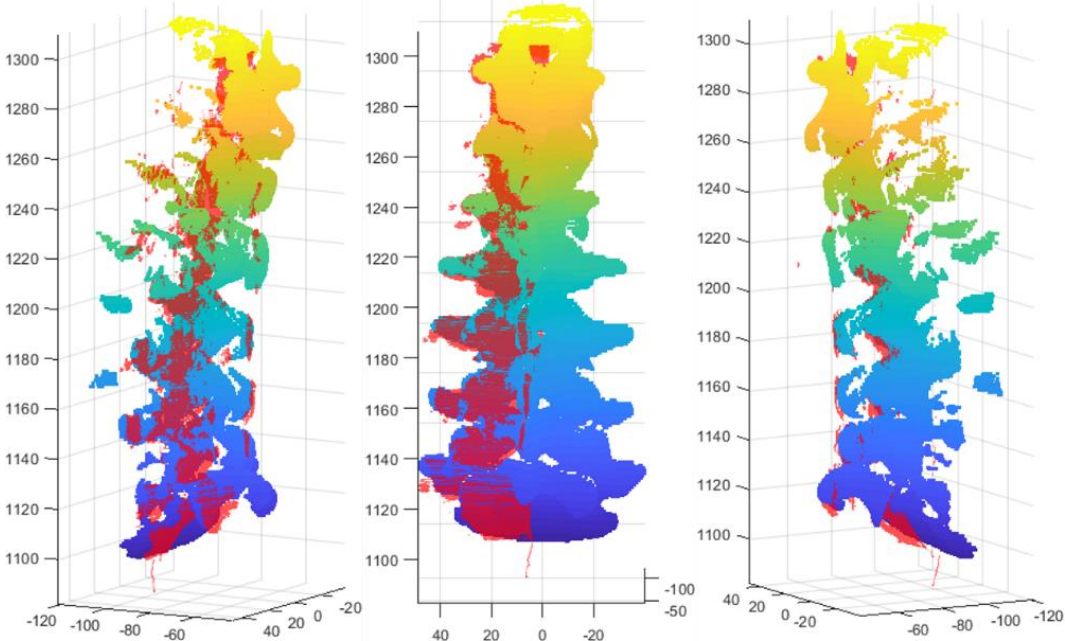


Figure 67 - Superposition of the full lumbar spine – left US PC after the initial transformation (in semi-transparent red) with the CT-derived PC (Video 16).

5.3.2.3. Full lumbar spine – right

The fiducials which allowed to perform an initial approximation between the full lumbar spine – right US PC and the CT-derived PC were chosen in the spinous process of L1 and L3 and in the right transverse process of L3.

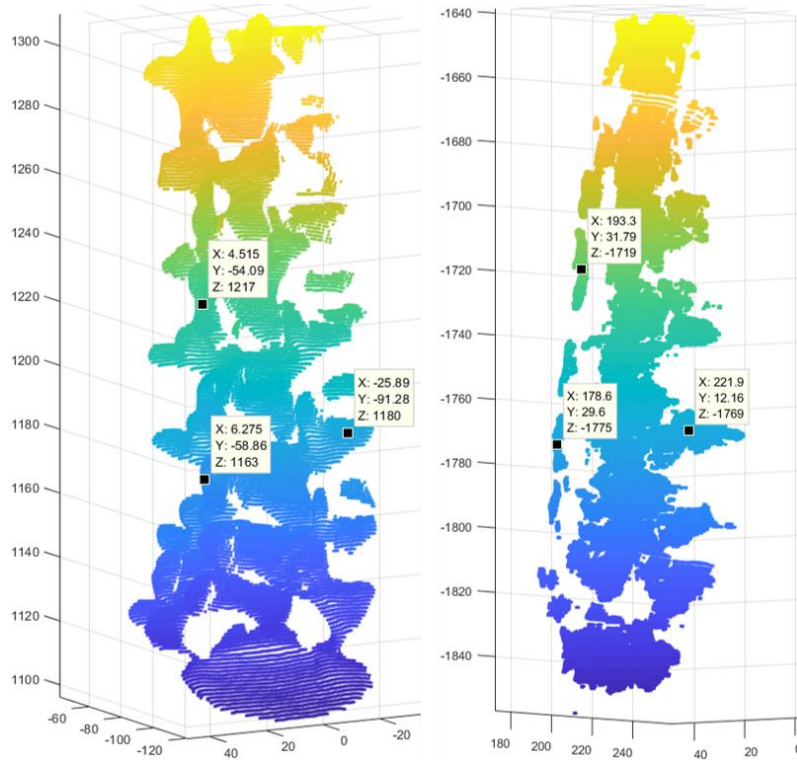


Figure 68 - Selection of the pair-points in CT-derived PC and in the full lumbar spine – right US PC.

Table 6 - Coordinates of the pair-points (fiducials) selected for the initial approximation between the full lumbar spine – right US PC and the CT PC.

<i>Fiducial</i>	Position in CT (mm)	Position in US (mm)
1	(-25.89 , -91.28 , 1180.07)	(221.88 , 12.16 , -1768.79)
2	(4.52 , -54.09 , 1217.07)	(193.29 , 31.79 , -1719.41)
3	(6.27 , -58.86 , 1163.07)	(178.63 , 29.60 , -1774.59)

The transformation which best matches the selected points was

$$T_{Polaris}^{CT*} = \begin{bmatrix} -0.331 & 0.943 & 0.025 & 80.726 \\ -0.882 & -0.318 & 0.347 & 722.323 \\ 0.335 & 0.093 & 0.938 & 2763.17 \\ 0 & 0 & 0 & 1 \end{bmatrix}$$

and the RMS of the distance between the transformed pair-points was

$$RMSE = 1.5392 \text{ mm}$$

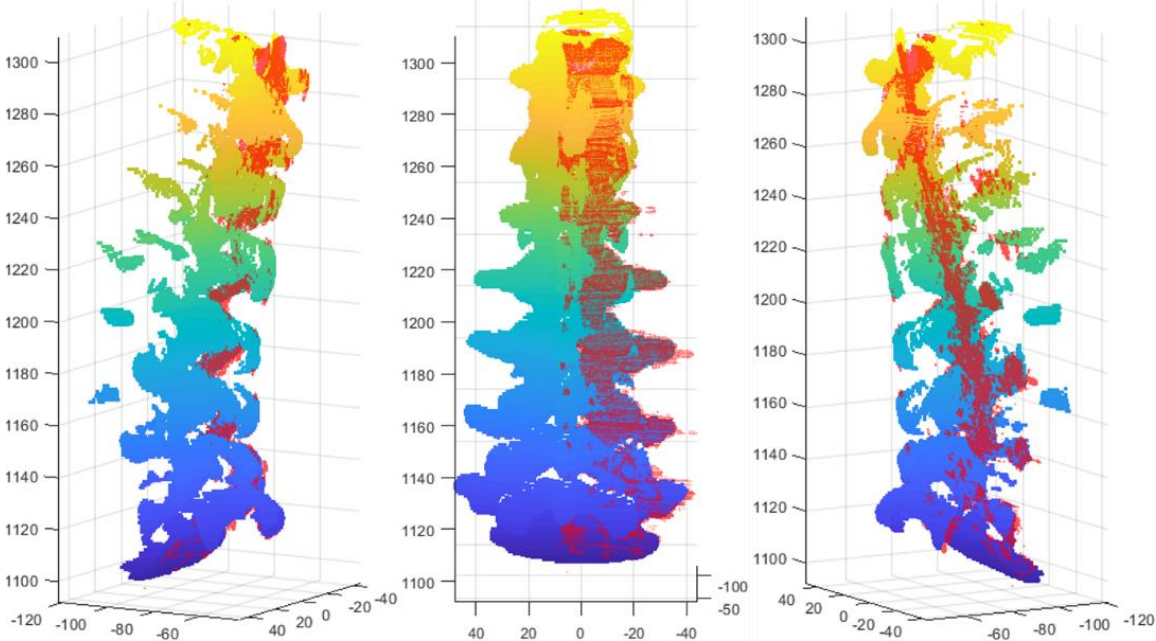


Figure 69 - Superposition of the full lumbar spine – right US PC after the initial transformation (in semi-transparent red) with the CT-derived PC (Video 17).

5.3.2.4. L3 vertebra – right (1st)

The fiducials which allowed to perform an initial approximation between the L3 vertebra – right (1st) US PC and the CT-derived L3 PC were chosen in the spinous, right superior articular and right transverse processes.

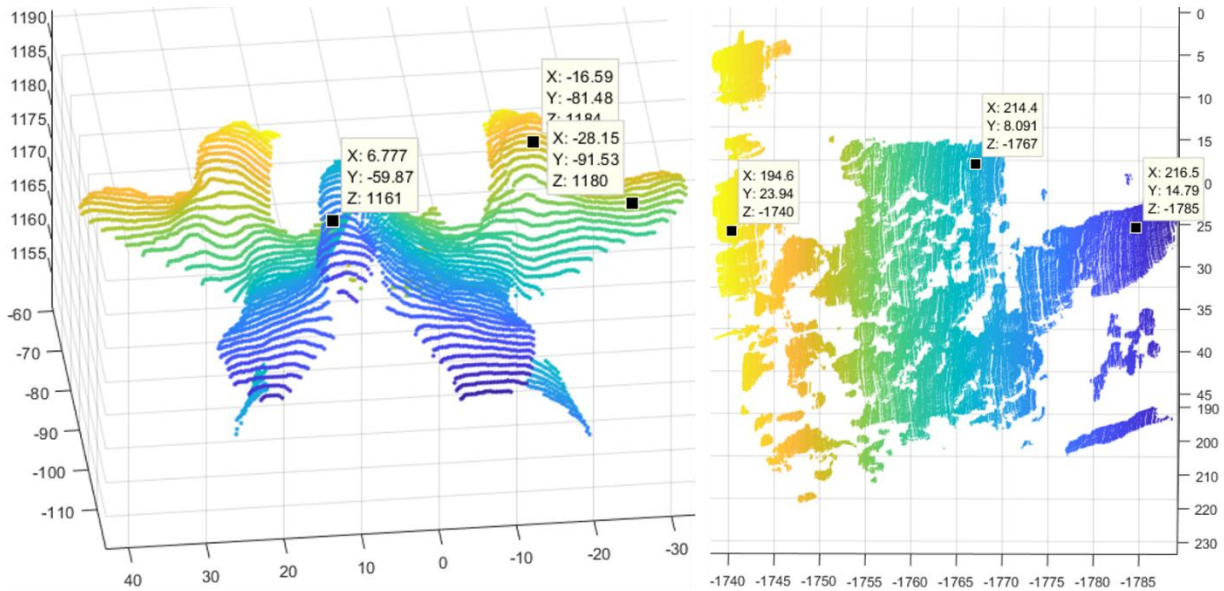


Figure 70 - Selection of the pair-points in CT-derived L3 PC and in the L3 vertebra – right (1st) US PC.

Table 7 – Coordinates of the pair-points (fiducials) selected for the initial approximation between the L3 vertebra – right (1st) US PC and the CT PC.

<i>Fiducial</i>	Position in CT (mm)	Position in US (mm)
1	(-28.15 , -91.53 , 1180.07)	(216.46 , 14.79 , -1784.63)
2	(-16.59 , -81.48 , 1184.07)	(214.41 , 8.09 , -1766.97)
3	(6.78 , -59.87 , 1161.07)	(194.61 , 23.94 , -1740.10)

The transformation which best matches the selected points was

$$T_{Polaris}^{CT*} = \begin{bmatrix} 0.347 & 0.231 & 0.909 & 1514.69 \\ -0.790 & -0.450 & 0.416 & 828.00 \\ 0.505 & -0.863 & 0.026 & 1129.31 \\ 0 & 0 & 0 & 1 \end{bmatrix}$$

and the RMSE of the distance between the transformed pair-points was

$$RMSE = 1.4931 \text{ mm}$$

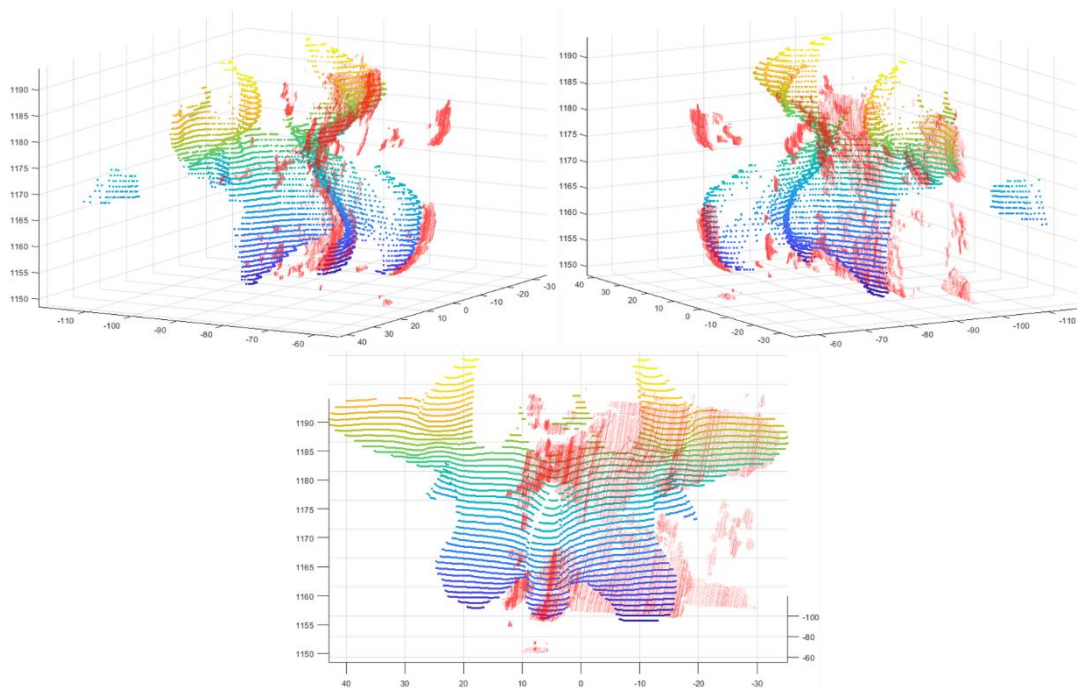


Figure 71 - Superposition of the L3 vertebra – right (1st) US PC after the initial transformation (in semi-transparent red) with the CT-derived L3 PC (Video 18).

5.3.2.5. L3 vertebra – right (2nd)

Just like the anterior case, the fiducials which allowed to perform an initial approximation between the L3 vertebra – right (2nd) US PC and the CT-derived L3 PC were chosen in the spinous, right superior articular and right transverse processes.

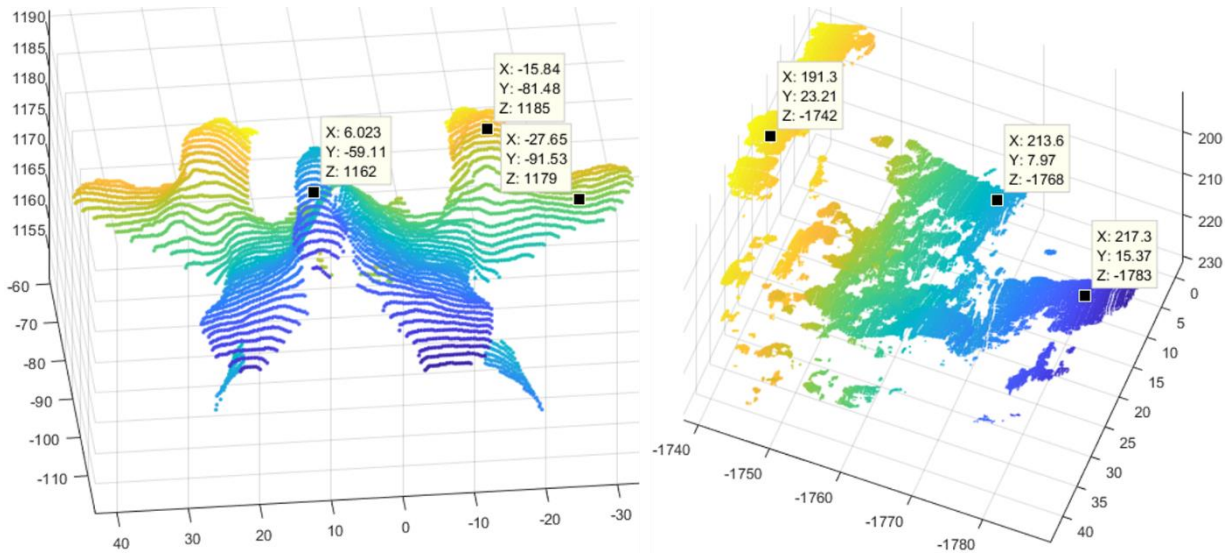


Figure 72 - Selection of the pair-points in CT-derived L3 PC and in the L3 vertebra – right (2nd) US PC.

Table 8 - Coordinates of the pair-points (fiducials) selected for the initial approximation between the L3 vertebra – right (2nd) US PC and the CT PC.

<i>Fiducial</i>	Position in CT (mm)	Position in US (mm)
1	(-27.65 , -91.53 , 1179.07)	(217.34 , 15.37 , -1782.86)
2	(-15.84 , -81.48 , 1185.07)	(213.64 , 7.97 , -1767.59)
3	(6.02 , -59.11 , 1162.07)	(191.26 , 23.21 , -1741.73)

The transformation which best matches the selected points was

$$T_{Polaris}^{CT*} = \begin{bmatrix} 0.264 & 0.151 & 0.953 & 1611.254 \\ -0.873 & -0.383 & 0.302 & 642.594 \\ 0.410 & -0.912 & 0.031 & 1158.821 \\ 0 & 0 & 0 & 1 \end{bmatrix}$$

and the RMS of the distance between the transformed pair-points was

$$RMSE = 0.5853 \text{ mm}$$

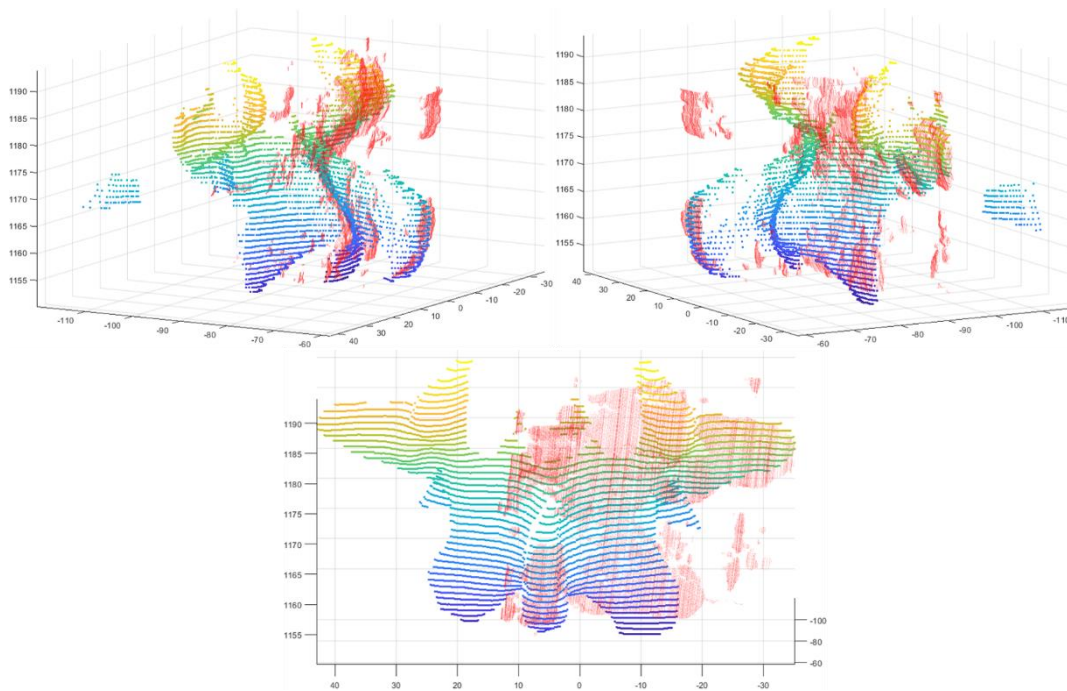


Figure 73 - Superposition of the L3 vertebra – right (2nd) US PC after the initial transformation (in semi-transparent red) with the CT-derived L3 PC (Video 19).

5.3.3. ICP algorithm

In this subsection, the results of applying the ICP algorithm between each different US-derived PC and the CT-derived PC, to refine the initial approximation, and their respective errors are presented.

Unlike the Kabsch algorithm, ICP was applied to all the points of each US-derived PC, with an increase of the computational and time cost comparing to the first algorithm. The stopping criteria chosen was the number of iterations, and so the algorithm ran for 15 iterations before outputting the transformation which best aligns the US-derived PC to the CT-derived PC.

For each of the L3 vertebra – right PC, the ICP algorithm was used in two experiments. In one experiment, the US-derived PC were merged using only the CT-derived PC of the L3 vertebra (shown in Figure 52) as reference. In the other experiment, the US-derived PC were merged using the CT-derived PC of the full lumbar spine (shown in Figure 51) as reference.

From Figure 74 to Figure 82 it is presented the CT-derived PC and all the different US-derived PC, after applying the resulting transformations of this registration step. The RMSE for each iteration of the ICP, computed as the RMS of the Euclidean distances between the closest points of each PC, is presented in Appendix B - ICP RMSE. The results of the ICP algorithm can also be seen from Video 20 to Video 28 [46].

5.3.3.1. Full lumbar spine – medial

The resulting matrix after 15 iterations of running the ICP algorithm was

$$T_{CT^*}^{CT} = \begin{bmatrix} 0.999 & 0.036 & -0.022 & 27.722 \\ -0.036 & 0.999 & -0.005 & 4.962 \\ 0.022 & 0.006 & 1 & 1.891 \\ 0 & 0 & 0 & 1 \end{bmatrix}$$

and the final RMS of the distance between each point of the transformed US-derived PC and its closest point of the CT-derived PC was

$$RMSE = 2.2067 \text{ mm}$$

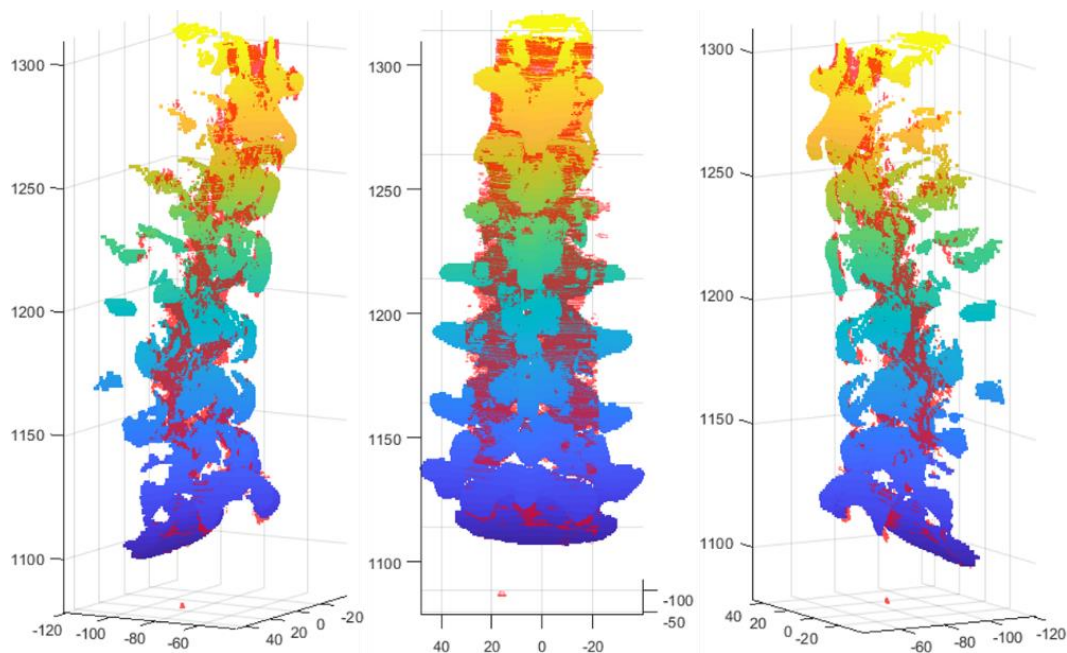


Figure 74 - Superposition of the full lumbar spine – medial US PC after the final transformation (in semi-transparent red) with the CT-derived PC (Video 20).

5.3.3.2. Full lumbar spine – left

The resulting matrix after 15 iterations of running the ICP algorithm was

$$T_{CT^*}^{CT} = \begin{bmatrix} 1 & -0.012 & -0.023 & 26.487 \\ 0.012 & 0.999 & 0.038 & -46.654 \\ 0.022 & -0.038 & 0.999 & -1.448 \\ 0 & 0 & 0 & 1 \end{bmatrix}$$

and the final RMS of the distance between each point of the transformed US-derived PC and its closest point of the CT-derived PC was

$$RMSE = 1.9867 \text{ mm}$$

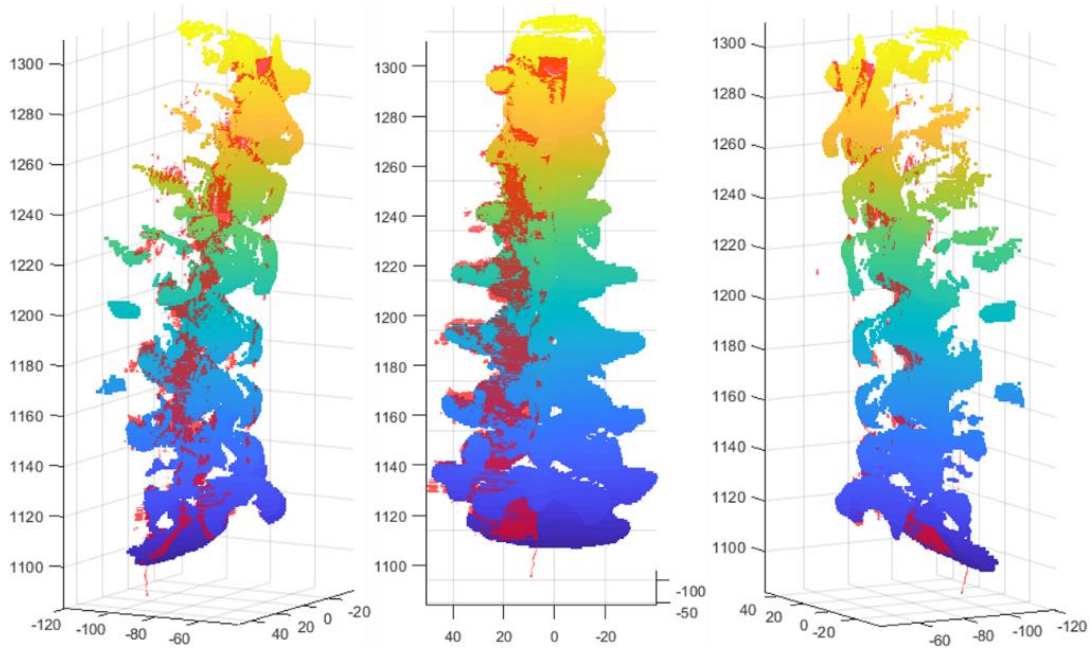


Figure 75 - Superposition of the full lumbar spine – left US PC after the initial transformation (in semi-transparent red) with the CT-derived PC (Video 21).

5.3.3.3. Full lumbar spine – right

The resulting matrix after 15 iterations of running the ICP algorithm was

$$T_{CT}^{CT*} = \begin{bmatrix} 1 & -0.011 & 0.001 & -1.670 \\ 0.011 & 1 & -0.014 & 16.154 \\ 0.001 & 0.014 & 1 & 1.167 \\ 0 & 0 & 0 & 1 \end{bmatrix}$$

and the final RMS of the distance between each point of the transformed US-derived PC and its closest point of the CT-derived PC was

$$RMSE = 1.9175 \text{ mm}$$

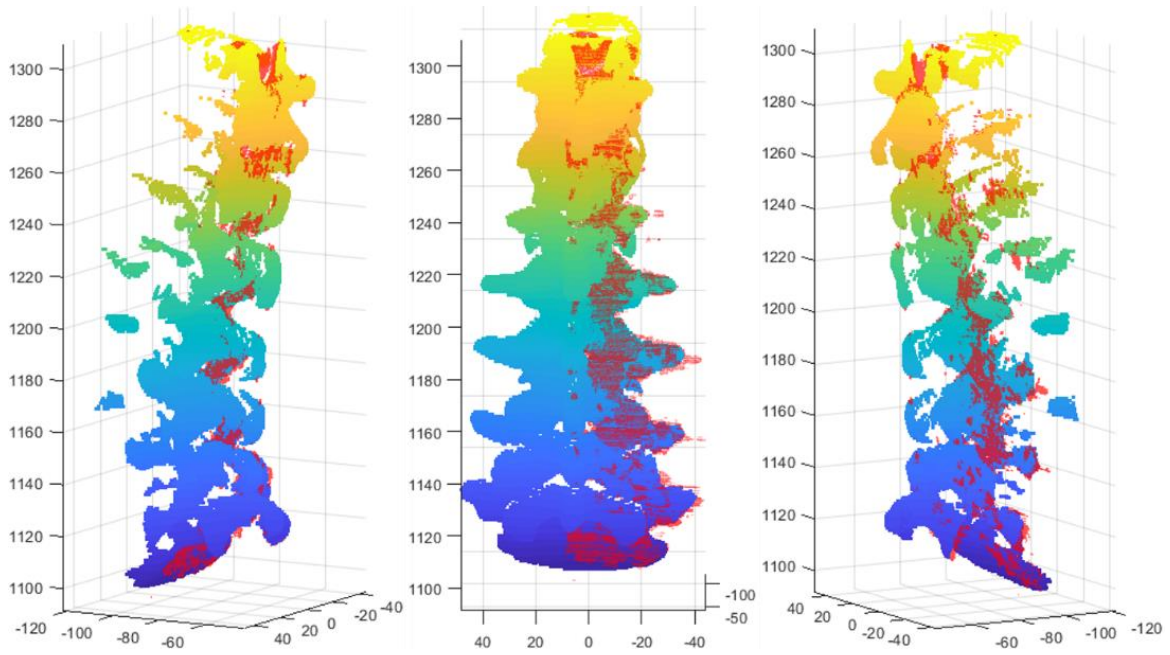


Figure 76 - Superposition of the full lumbar spine – right US PC after the initial transformation (in semi-transparent red) with the CT-derived PC (Video 22).

5.3.3.4. L3 vertebra – right (1st)

The resulting matrix after 15 iterations of running the ICP algorithm with the L3 CT-derived PC was

$$T_{CT}^{CT*} = \begin{bmatrix} 0.996 & 0.063 & 0.056 & -59.005 \\ -0.068 & 0.993 & 0.096 & -114.445 \\ -0.050 & -0.100 & 0.994 & -3.929 \\ 0 & 0 & 0 & 1 \end{bmatrix}$$

and the final RMS of the distance between each point of the transformed US-derived PC and its closest point of the CT-derived PC was

$$RMSE = 5.2870 \text{ mm}$$

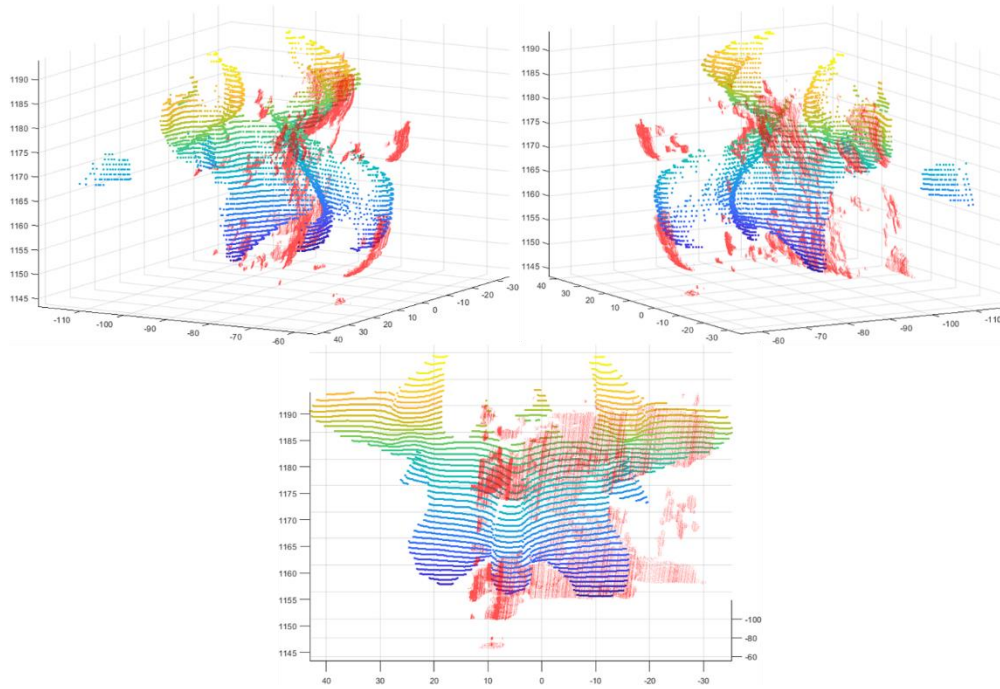


Figure 77 - Superposition of the L3 vertebra – right (1st US PC after the final transformation (in semi-transparent red), computed with the CT-derived L3 PC as reference, and the CT-derived L3 PC (Video 23).

The resulting matrix after 15 iterations of running the ICP algorithm with the full lumbar CT-derived PC was

$$T_{CT}^{CT*} = \begin{bmatrix} 0.990 & 0.059 & 0.131 & -147.631 \\ -0.039 & 0.988 & -0.148 & 171.785 \\ -0.138 & 0.141 & 0.980 & 33.842 \\ 0 & 0 & 0 & 1 \end{bmatrix}$$

and the final RMS of the distance between each point of the transformed US-derived PC and its closest point of the CT-derived PC was

$$RMSE = 2.5279 \text{ mm}$$

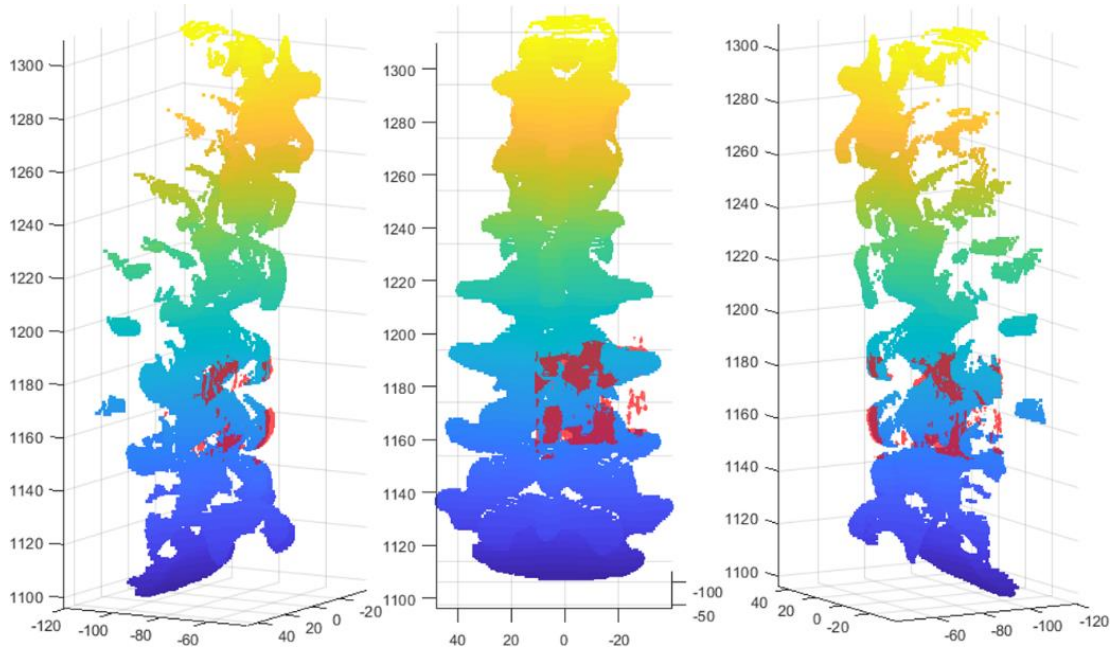


Figure 78 - Superposition of the L3 vertebra – right (1st) US PC after the final transformation (in semi-transparent red), computed with the complete CT-derived L3 PC as reference, and the complete CT-derived PC (Video 24).

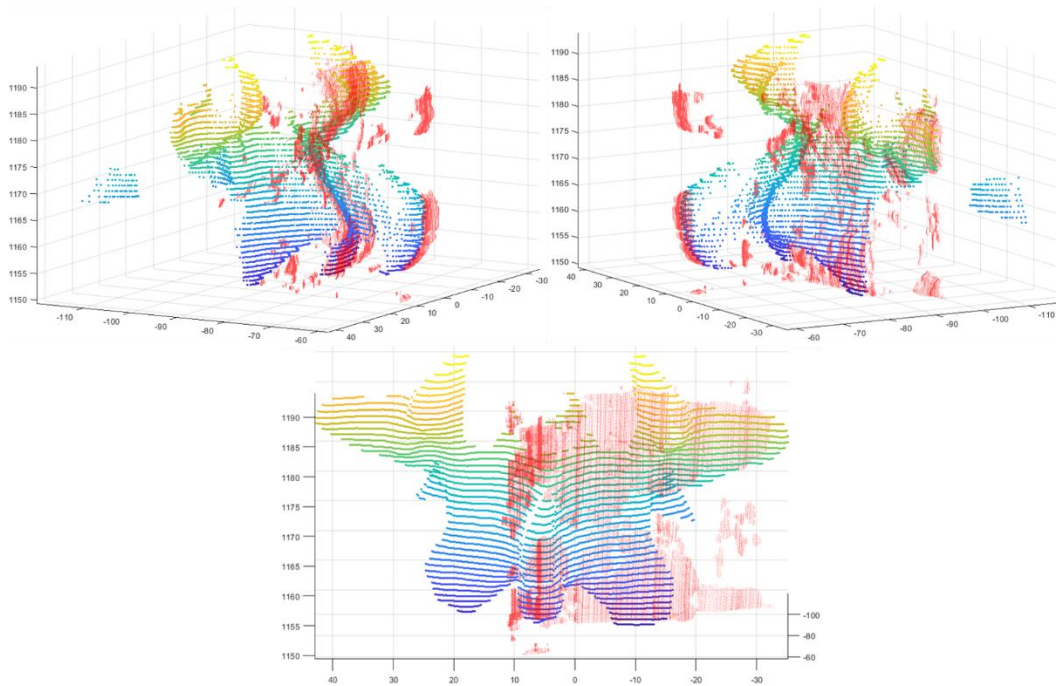


Figure 79 - Superposition of the L3 vertebra – right (1st) US PC after the final transformation (in semi-transparent red), computed with the complete CT-derived L3 PC as reference, and the CT-derived L3 PC (detail of the previous figure) (Video 25).

5.3.3.5. L3 vertebra – right (2nd)

The resulting matrix after 15 iterations of running the ICP algorithm with the L3 CT-derived PC was

$$T_{CT^*}^{CT} = \begin{bmatrix} 0.991 & 0.049 & 0.120 & -138.126 \\ -0.066 & 0.9874 & 0.144 & -172.273 \\ -0.112 & -0.1506 & 0.982 & 5.571 \\ 0 & 0 & 0 & 1 \end{bmatrix}$$

and the final RMS of the distance between each point of the transformed US-derived PC and its closest point of the CT-derived PC was

$$RMSE = 4.9151 \text{ mm}$$

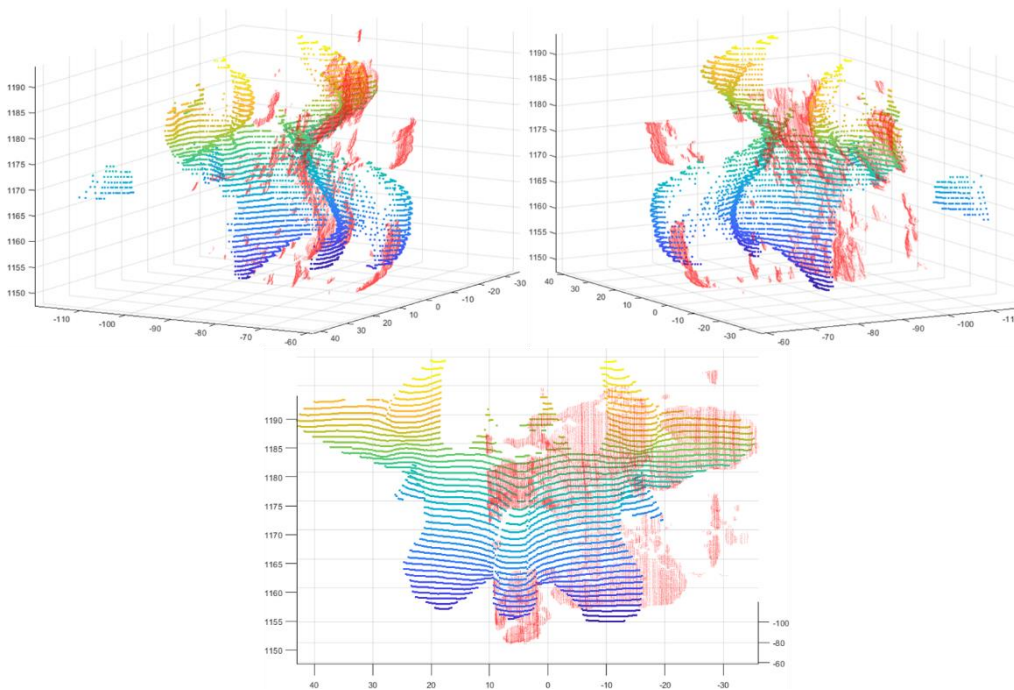


Figure 80 - Superposition of the L3 vertebra – right (2nd) US PC after the final transformation (in semi-transparent red), computed with the CT-derived L3 PC as reference, and the CT-derived L3 PC (Video 26).

The resulting matrix after 15 iterations of running the ICP algorithm with the full lumbar CT-derived PC was

$$T_{CT^*}^{CT} = \begin{bmatrix} 0.998 & 0.008 & 0.058 & -68.199 \\ -0.005 & 0.999 & -0.055 & 63.857 \\ -0.058 & 0.055 & 0.997 & 7.043 \\ 0 & 0 & 0 & 1 \end{bmatrix}$$

and the final RMS of the distance between each point of the transformed US-derived PC and its closest point of the CT-derived PC was

$$RMSE = 2.6175 \text{ mm}$$

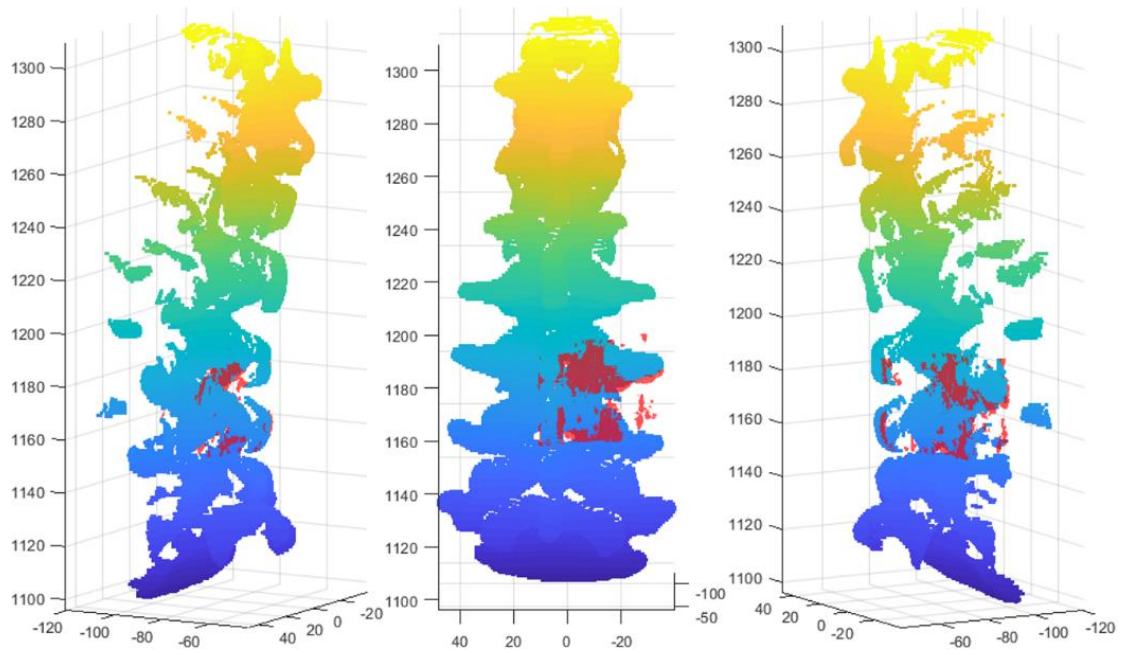


Figure 81 - Superposition of the L3 vertebra – right (2nd) US PC after the final transformation (in semi-transparent red), computed with the complete CT-derived L3 PC as reference, and the complete CT-derived PC (Video 27).

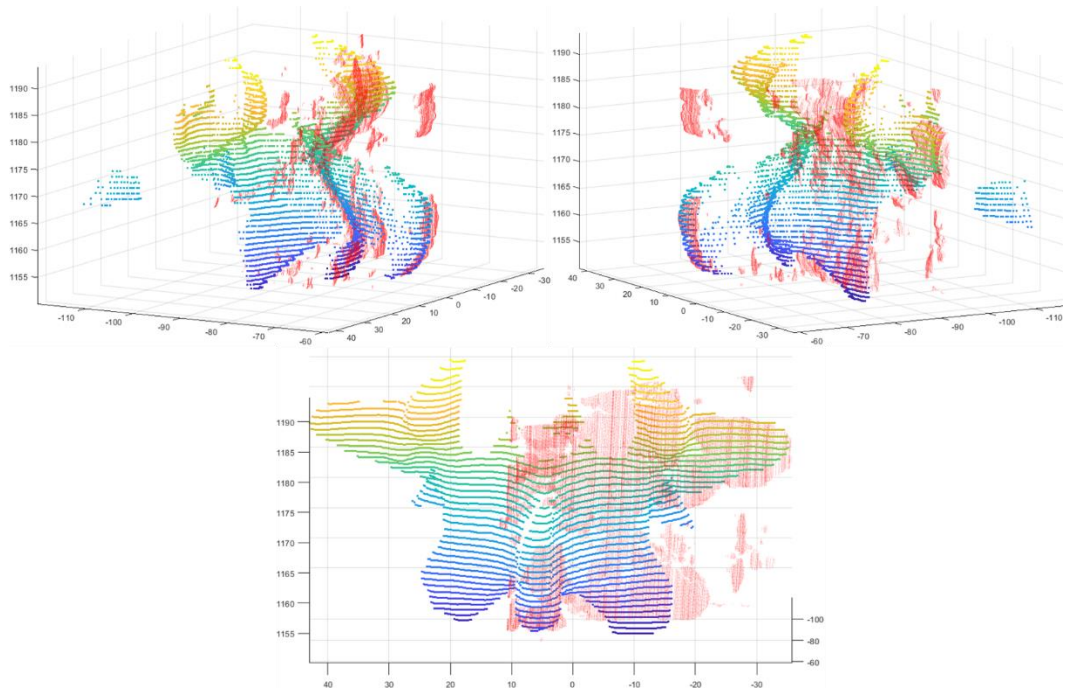


Figure 82 - Superposition of the L3 vertebra – right (2nd) US PC after the final transformation (in semi-transparent red), computed with the complete CT-derived L3 PC as reference, and the CT-derived L3 PC (detail of the previous figure) (Video 28).

5.4. Navigation System

As explained in section 4.4, after loading the CT-data and the transformation $T_{Polaris}^{CT}$, and connecting to the Polaris system, the navigation system displays the CT-derived PC and the surgical plans in the same referential as the Polaris pointer.

Figure 83 shows the CT-derived PC and the surgical plans in the navigation system's interface.



Figure 83 - Navigation system's interface with the CT-derived PC and the surgical plans.

To test the navigation system and the developed methodology in general, we inserted the Polaris Pointer in some landmarks of the lumbar spine phantom and compared its position within the navigation system. Figure 84 and Figure 85 present the position of the Polaris Pointer in the navigation system (A) and inside the lumbar spine phantom (B), in the extremity of the left transverse process of L2 and L3, respectively.

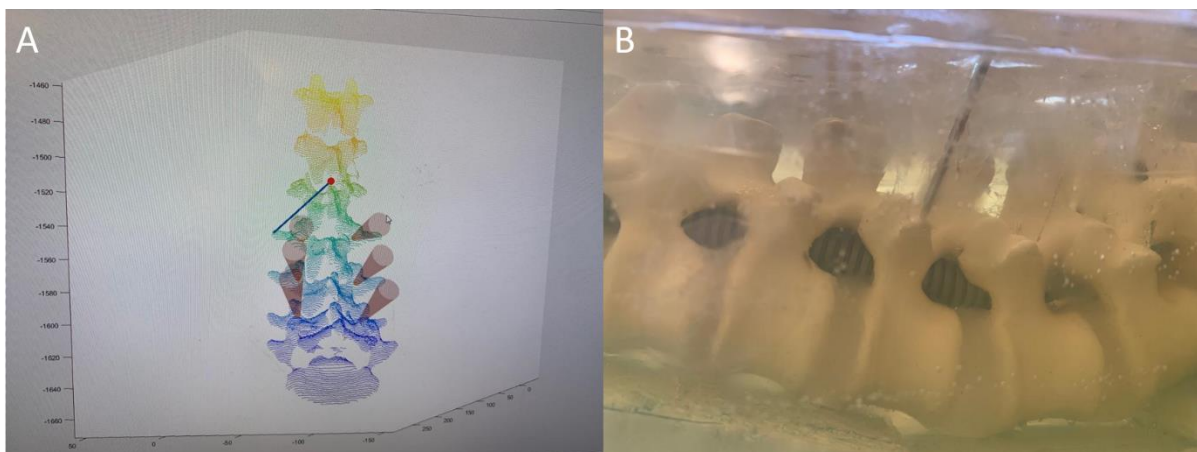


Figure 84 – Polaris Pointer in the extremity of the left transverse process of L2. A: Navigation System. B: Lumbar Spine Phantom.

Figure 86 presents the insertion of the Polaris Pointer in the surgical planning site for the L2 left pedicle screw in the navigation system (A) and inside the lumbar spine phantom (B and C).

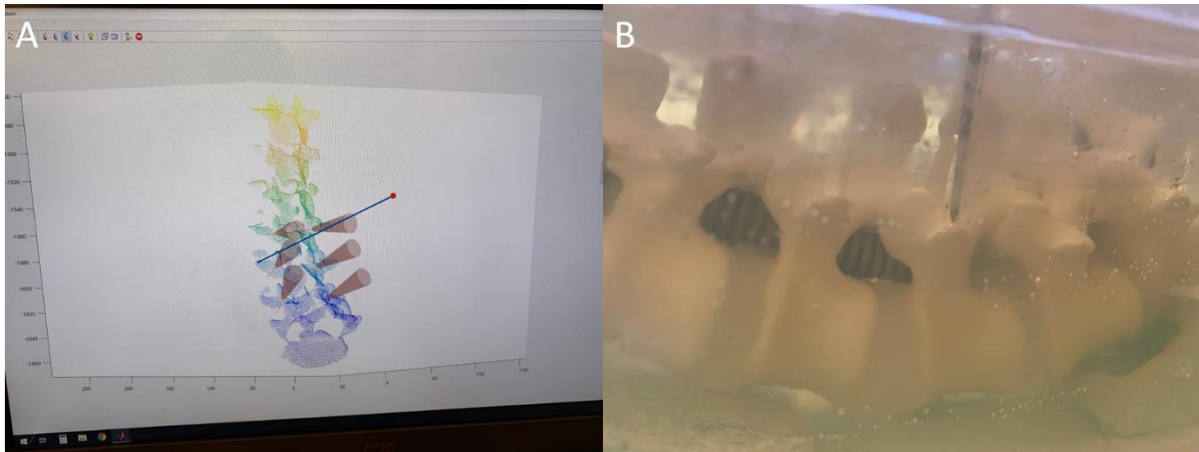


Figure 85 - Polaris Pointer in the extremity of the left transverse process of L3. A: Navigation System. B: Lumbar Spine Phantom.

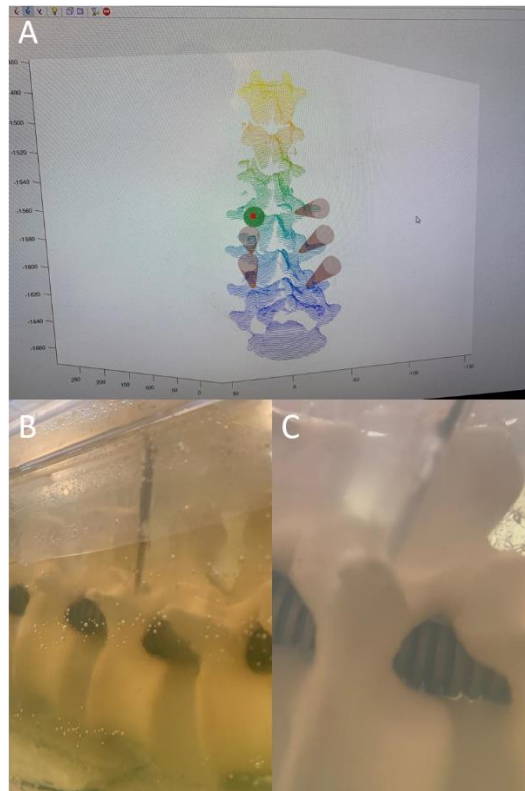


Figure 86 - Polaris Pointer surgical plan for left L2 pedicle screw. A: Navigation System. B and C: Lumbar Spine Phantom.

Video 29 shows all the process of using the navigation system. The upper half of the screen shows the screen of the computer and the bottom half shows the user with the Polaris pointer and the lumbar spine phantom (there is a slight desynchronization between the two halves of the video) [46].

Video 30 shows some testing of the Navigation System developed [46].

6. Discussion

6.1. CT-scan

This subsection presents the discussion of the results related with the acquired CT-scan, the CT-data itself, its segmentation, performed using 3D Slicer, and the surgical plans, performed using MATLAB®.

The image-guided (IG) surgery for pedicle screw placement, which was the procedure simulated in this project, started with the acquisition of preoperative images of our lumbar spine phantom, a test subject specifically built for this work. This preoperative data was acquired by performing a CT-scan to the phantom.

In the CT-data acquired, it was possible to differentiate all the interesting regions of the lumbar phantom, mainly the 3-D printed vertebrae, the ringed tube, the base of high density styrofoam and the gelatin, since there was a good contrast between the image intensity of the different materials. However, it is important to note that this data presents some differences when faced against the CT-data of a real human subject.

Comparing Figure 20 and Figure 87, it is possible to notice that in a real patient's CT-scan, the voxels corresponding to the vertebrae appear brighter than the ones of the surrounding tissue, as the bone absorbs more X-ray radiation than the muscular or ligament tissues. On the contrary, in the lumbar spine phantom, the regions corresponding to the vertebrae appear darker than the gel and the interior of the vertebrae is almost completely black with grid-like features. This happens because the vertebrae were 3-D printed with ABS polymer, which absorbs less radiation than the gelatine, and only the vertebrae surfaces were solid, being its interior full of air with a grid, which gives support to the hollow vertebrae structure. In the lumbar spine phantom CT, we could also see the ringed tube, which in some regions was difficult to differentiate from the vertebrae, as it was made from a similar material to the one used to print the model. The high density styrofoam appears completely black since it is mostly composed by air. Some regions of the model also appear as black voxels due to the imprisonment of air during the construction of the phantom, mainly inside the ringed tube, in the vertebral foramens, and inside the silicone intervertebral discs and facet capsular ligaments.

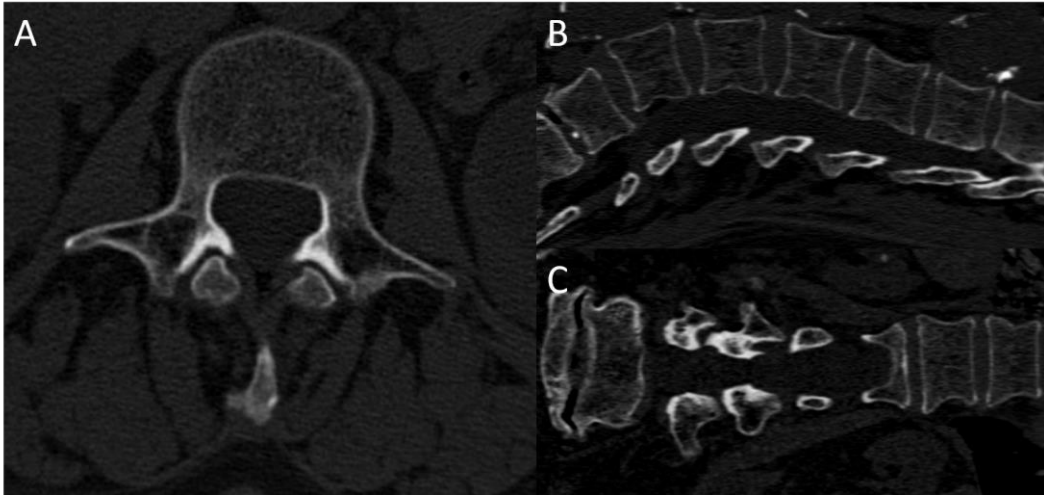


Figure 87 – CT-scan of a real patient's lumbar spine: axial (A), sagittal (B) and coronal (C) slices.

Despite the difficulties presented, which led to the necessity of an important manual step in the segmentation process, we were able to obtain a very good CT-derived 3-D model of our phantom. Evaluating qualitatively, we consider that the segmentation performed was able to highlight all the phantom features, with the resulting vertebral models (T11, T12, L1, L2, L3, L4 and L5) being almost identical to the printed models that gave them origin.

Through the CT-data and the CT-derived 3-D models, it was possible to successfully plan the insertion points for the pedicle screws at the L2, L3 and L4 level and their ideal directions. This was made using a MATLAB® GUI created for this task, using medical guidance as explained previously. The Surgical Planning GUI allowed to plan the placement of the screws and also validate its results, since the user could see the intersection of the planned screws with the different CT planes, and change their location and orientation to avoid conflicting with the vertebral surface, as shown in Figure 88.

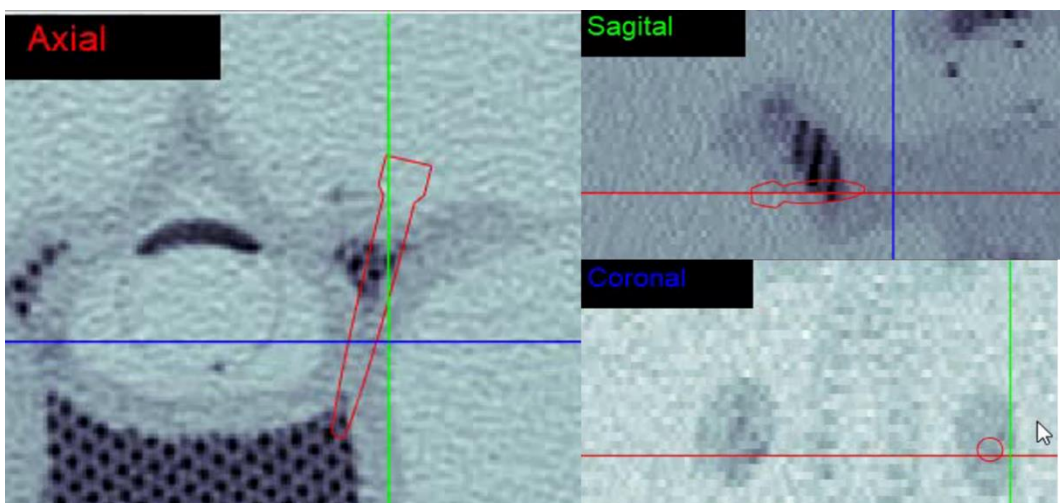


Figure 88 - Intersections of one pedicle screw with the CT slices. Detail of the Surgical Planning (Figure 25).

6.2. Freehand 3-D Ultrasound imaging

In this subsection we present the discussion of the main topics related with the US imaging modality used, namely the calibration process and the acquisitions, performed using Stradwin, and their segmentation, performed using MATLAB®.

6.2.1. Calibrations

The key step in Freehand 3-D Ultrasound imaging is the probe calibration. It is this step that allows to accurately acquire an intraoperative US-volume, by computing the real intraoperative location of a multiple set of US frames and of the internal features captured in them. The calibration method chosen made use of the Polaris pointer to set the parameters constrains to calculate the transformation between the US probe and the US frame, and so, the first step in the calibration process was to calibrate the Polaris pointer.

6.2.1.1. Pointer pivoting

Pointer pivoting allows to compute the translation between the Polaris pointer marker and the location of its tip. It was a necessary step in the probe calibration method we used, as only the pointer's tip is visible in the US image and it was extremely important to know its exact location.

This calibration step proved to be simple and accurate, since all the five calibrations were performed in less than twenty seconds and, as Table 2 shows, the error associated with each try was very small, less than 1 *mm*. Despite this simplicity, some pointer pivoting attempts had to be repeated, because any movement of the pointer's tip resulted in a convergence fail.

6.2.1.2. Probe calibration

After calibrating the pointer, it was possible to start the probe calibration process, which allows to compute the transformation between the US probe coordinate system (COS) and the US frame COS.

This step proved more complex, difficult and user-dependent than the previous one, mainly due to the difficulty in correctly aligning the tip of the pointer with the US B-mode frame. Although Stradwin computed an automatic segmentation of the pointer's tip in the US image, this segmentation was not always correct, as sometimes Stradwin segmented any air particle instead of the pointer, or the segmented point was indeed the pointer, but not its tip, when it was not correctly aligned with the US frame. So, it was up to the user to accept only the points when it was sure the pointer's tip was correctly segmented in the US image, which could be very difficult.

Analyzing Table 3, it is possible to conclude that despite the complexity of this calibration method, we managed to achieve good convergence results, with the error laying under 1 *mm* in all the coordinate axis and RMSE for the best result obtained. Unfortunately, this calibration method is not very reproducible, as different calibration attempts resulted in considerably variable errors and parameters, which result mainly from the high dependency on the user choices and skill.

Another problem related with the calibration process is the difference in the convergence between the upper part of the US frame, which stands closer to the US probe, and the bottom part of the image. This problem, which can be verified in Figure 53, results from the fact that the image of the pointer's tip in the US B-mode is more perceptible if the pointer is perpendicular to the direction of the US waves, which is only possible to achieve the closer the tip is to the water bath surface, due to the configuration of the devices used for calibration, as explained in Figure 89. This problem also explains the difference between the errors in the different coordinate axis, which is always greater in one of them than in the others.

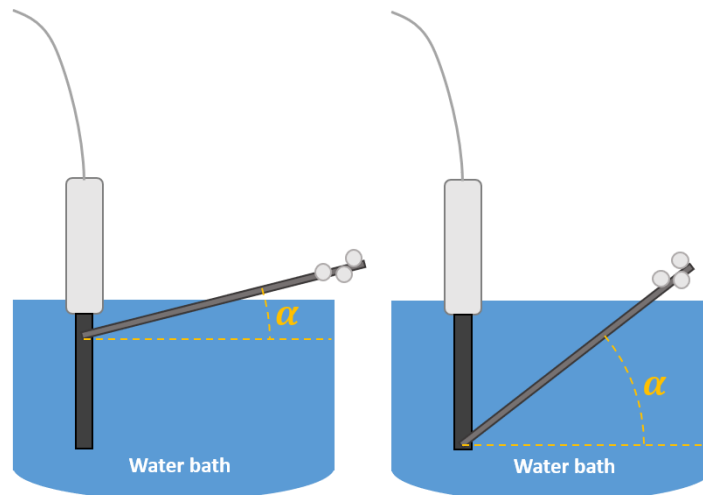


Figure 89 - Differences in the angle α between the pointer and the direction perpendicular to the US propagation. The smaller α , the more perceptible is the pointer tip in the US image.

Concluding, although this calibration method presents some disadvantages, in general it presented good results calculating the transformation $T_{frameUS}^{probeUS}$, which, combined with the Polaris data, allowed to compute the US frames in their approximately correct intraoperative locations and orientations.

6.2.2. Acquisitions and segmentation

The transformation which resulted from the probe calibration with the smallest error was used to perform the acquisitions of various US-volumes, that were posteriorly segmented. Those volumes consisted in a large set of US frames stacked in their positions in the Polaris COS, as shown in the previous chapter.

The US frames acquired by scanning the surface of the lumbar phantom allowed to differentiate the key features of the posterior regions of each vertebra, mainly their spinous and transverse processes. Their articular processes and their laminae could also be seen but were not so easily differentiated.

When compared to the CT-data acquired, it was possible to conclude that in the US-data there are considerably fewer observable details and that is harder to visually understand the images. This happens due to the amount of scattering and reflections present in the US images, mainly because of the presence of air bubbles which were imprisoned in the gelatin during the phantom construction or in

the silicone in the capsular ligaments, but also because of the scattering that the US waves suffer when they meet the plastic vertebral surface. Also, the size of the US transducer does not allow to acquire the full width of the vertebrae, fact that contributes to the difficulty in understanding the contours of the vertebrae in the US images.

It is important to note that, similarly to the CT data of the lumbar spine phantom (as discussed in section 6.1), the US frames acquired from this phantom also present some major differences from the US frames acquired from a real patient. Figure 90 shows an US frame of an acquisition from a real lumbar spine, where it is possible to see the vertebral bone translated as dark pixels, as bone is opaque for the US waves, the skin and muscular tissues are translated as different shades of gray and that the interfaces between bone and surrounding tissue that are perpendicular to the US waves propagation direction are translated as bright pixels, because this surfaces reflect more US waves to the transducer. This US acquisition of the real spine was performed using the same Ultrasound device and the same parameters as the acquisitions of the lumbar spine phantom.

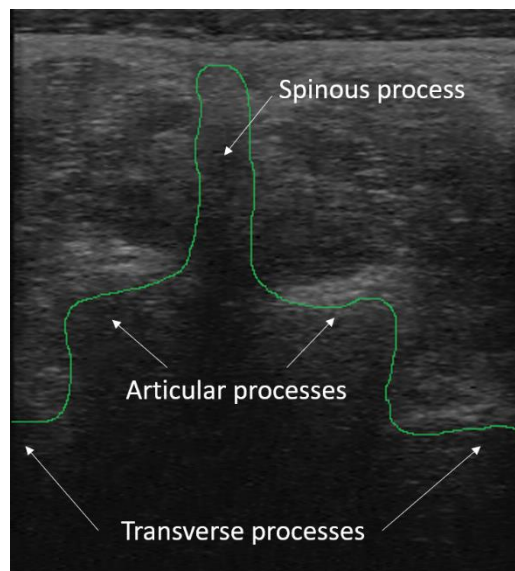


Figure 90 - US frame of a real patient's vertebra with its main features highlighted.

The application of a threshold in the segmentation process was crucial to deal with the scattering, since these sonic artifacts usually present a smaller brightness than the pixels which correspond to the vertebral surface, which allowed to perform a correct semi-automatic segmentation by choosing a threshold value high enough to highlight only the regions of the gelatin-vertebrae interface. However, some regions were misclassified and some outliers were still present.

After segmenting each US frame, the segmented points were computed in their location in the Polaris COS. The results of the segmentation, present from Figure 55 to Figure 59, are not easily understood or evaluated in a 2-D graphical representation, but by visualizing the US-derived point clouds (PC) in a graphical interface where the user can change its point of view or rotate the PC, it is possible to understand the segmented regions and differentiate all the vertebrae and their principal features.

In the segmentation process of the acquisitions with the full lumbar length, full lumbar spine – medial, left and right, the spinous processes of all the vertebrae were identifiable, with the exception of T11 and L5, which were outside the defined region of interest because they were located near the gelatin surface, where the US image presents a great amount of noise. In the full lumbar spine – left US PC, it is possible to identify the left transverse processes of all the lumbar vertebrae of the spine phantom. The same happens to the right transverse processes in the full lumbar spine – right US PC. The remaining posterior vertebral regions, although they were present, were not so easily identifiable and differentiated, mainly the interface between each different vertebra. Overall, the acquisition whose segmentation presented less outliers and allowed the easiest identification of the vertebral landmarks was the full lumbar spine – right. This occurred because the right side of the lumbar spine phantom presented fewer air bubbles imprisoned in the gelatin than the left side. For this reason, the two acquisitions that include only one side of a single vertebra were performed in the right side of the phantom.

As mentioned in chapter “Methods”, the L3 vertebra – right (1st and 2nd) scans were acquired to check if it was possible to perform registration of a single vertebra to overcome the problem of relative motion between the lumbar spine portions. The different orientation of the US probe and its slightly radial movement allowed to identify each region of L3 with more detail than in the previous acquisitions, as seen in Figure 58 and Figure 59. However, in these acquisitions we were unable to scan only the L3 vertebra, resulting in the inclusion of some parts of the adjacent vertebrae, namely the spinous and the inferior articular process of L2, the superior articular process of L4 and, in the L3 vertebra – right (1st) US PC, even the transverse process of L4. This fact had some implications in the registration process, as will be discussed in the next section.

6.3. Registration

As seen in section 5.3.1, the registration algorithms that were applied in this work presented good results finding the transformations between true identical PC. Using a good initial approximation, like shown in Figure 63, it is possible to correctly align two PC whose only difference lay in a rigid transformation. Given the different natures of the point clouds used in this project, CT-derived and US-derived, it is not possible to have a perfect match between them. Nevertheless, it is possible to achieve a good approximation, which can be used to perform image or computed guided surgeries with a minimal error. In this subsection we will be discussing the results of the two steps of the registration process, which made possible to compute the transformation between the CT COS and the intraoperative COS, also mentioned in this work as Polaris COS.

6.3.1. Kabsch algorithm

As explained previously, Kabsch algorithm allows to compute the transformation between two sets of matching points. This algorithm proved to be simple and useful to calculate the initial approximation between the different PC, as it was only necessary to select three non collinear points in each US PC and their matching pairs in the CT PC. To correctly select these matching points, also known as

fiducials, we opted to pick them in distinct vertebral features, which could be easily identified in either the CT-derived PC and the US-derived ones, has shown in section 5.3.2. Although matching pair-points were not hard to identify in the three major posterior portions of the vertebra – the spinous and the transverse processes, the selection of those points in other vertebral regions, like the articular processes, was not so easy. The main disadvantage of this method is the high dependency on the user, since the points were selected by hand based on its skill and experience.

After the fiducial selection, we ran the Kabsch algorithm for the selected points, resulting in a transformation matrix for each US data acquired. We could also compute the associated error between each matching pair-points.

Applying these initial transformations, $T_{Polaris}^{CT*}$, to each correspondent US-derived PC and plotting the result with the CT-derived PC, as show in Figure 65, Figure 67, Figure 69, Figure 71 and Figure 73, we are able to see the preliminary results of the registration. As explained in the previous section, it is not easy to evaluate the full extent of these 3-D results in 2-D representations. Despite this fact, it is possible to notice a good fit between all the different US-derived PC and the CT-derived PC, mainly when observing the major vertebral features. The existing spinous processes of each US-derived PC match the spinous processes of the CT PC, and the same is observable in the visible transverse processes. The matching between the other different portions of the vertebrae PC are not so easily evaluated. Although it is not easy to compare the different results, since some of them showed best matching in some lumbar spine portions and the others showed best matching in other portions, we can notice that the results with the full lumbar spine – left and right are better than the results with the full lumbar spine – medial, as this US PC presents more points misclassified as vertebrae. The two L3 vertebra - right US PC presented both also good matching results. In general, we can affirm that the computed initial transformations are good approximations between the different PC, allowing the next registration step to refine the transformation without converging to a wrong solution.

The discussed results were possible by a correct identification of the fiducials. This fact is supported by the errors presented, where one can note that the RMS of the distance between the transformed pair points was in the order of 2 mm or even less. However, it is important to note that this error is only associated with the fiducials selection and is not directly meaningful to the registration per se, and for that reason we could only make a qualitative evaluation.

6.3.2. ICP algorithm

6.3.2.1. Full lumbar spine – medial, left and right US PC

The last step of the registration process was to apply the Iterative Closest Point algorithm to the transformed US-derived point clouds which resulted from the initial approximation obtained using the Kabsch algorithm.

As explained previously, we ran ICP using the CT-derived PC as reference and the US-derived PC as source, since the point cloud that originated from the CT data is more complete, including more

features than each US PC, and so it must be used as reference. This way, ICP iteratively computed the transformation that minimizes the distance between each point of the US-derived PC and its closest point in the CT-derived PC.

For the full lumbar spine – medial, left and right US PC, the reference PC used was the CT-derived PC that included all the vertebrae. After running the ICP for 15 iterations, it computed the 'ideal' transformation, which refines the initial approximation. After applying the final transformation, $T_{CT^*}^{CT}$, to these US-derived PC, and plotting them against the CT-derived PC, has shown in Figure 74, Figure 75 and Figure 76, it was possible to visualize the results of the complete registration process. Comparing these figures with Figure 65, Figure 67 and Figure 69, we concluded that the transformation computed by ICP seems to have made some parts of the US-derived PC approximate to the CT-derived PC. Despite this observation, we concluded that it is not possible to visually evaluate the difference between the results neither if the result after the ICP is better than the result of only applying Kabsch, since the information given by the different plots does not allow this level of perception.

Nevertheless, analyzing the tables from Table 9 to Table 15 of Appendix B - ICP RMSE, it is possible to conclude that ICP promoted a small decrease in the mean distance between the different US PC and the CT ones on every iteration, resulting in a RMS distance of around 2mm for each full lumbar spine US PC registration. However, this does not mean that the ICP has improved registration, since some points of the US-derived PC could have been approximated to points of the CT-derived PC that do not represent the exact same location in the vertebrae. Although this RMS error values are useful to evaluate the mean distance between the two point clouds, they are highly dependent of the nature of the registered PC and their point density in different vertebral regions. Also, it is important to note that the US-derived PC include the silicone capsular ligaments in the articular processes, which are not present in the CT-derived PC. For all the appointed reasons, it is not possible to extrapolate conclusions or affirm that the error in the pedicle screw insertion will correspond to the error presented by the ICP.

Contrasting with the error presented for the Kabsch algorithm and the ICP algorithm, known as Registration Error, there is another type of error measure, known as Target Registration Error. This error measurement compares the local differences between points directly chosen in the lumbar spine phantom and their correspondent points in the CT-derived PC after the registration. This allows to assess a more quantitative error, which makes possible to predict the associated registration error when performing the pedicle screw insertion surgery. However, this type of error was not measured, since it needed the acquisition of defined targets in the lumbar spine phantom with the pointer. To get them, we would need to violate the gelatine with the pointer, which would open holes in the material allowing air to enter, making it impossible to acquire new US data.

6.3.2.2. L3 vertebra – right US PC

As explained before, the US data including only one side of one vertebra were acquired to check if it was possible to perform registration using only one vertebra in these current conditions, which has the advantage of overcoming the problem of the relative mobility between each lumbar segment.

After performing the initial approximation with the Kabsch algorithm, we ran ICP using each L3 vertebra – right US PC as source and the CT-derived L3 PC as reference, and after 15 iterations, the results were plotted, as presented in Figure 77 and Figure 80. Comparing these figures with Figure 71 and Figure 73, it is possible to conclude that ICP has converged to a wrong solution and that the final registration is worse than the initial approximation. This is especially noticeable when comparing the spinous processes of the two PC, since the spinous process of the US-derived PC moved away from the one of the CT-derived L3 PC.

After the presented results, we could conclude that there is a great decrease in the accuracy of the ICP when performing the registration of two point clouds when the source PC includes points of key vertebral regions that are not present in the reference PC. This happened because in the L3 right US acquisitions some parts of the L2 and L4 vertebra were also captured in the US images. In this case, ICP tries to minimize the distance between the points of the adjacent vertebrae with points of the CT-derived L3 PC, which are not their matching.

This registration could be improved by removing the non-L3 parts of the US-derived PC, but, although some parts of the adjacent vertebrae could be easily removed manually from each L3 vertebra – right US PC, as the spinous process of L2, some other parts like the inferior articular process of L2 or the superior articular process of L4 are not easily differentiated from the articular processes of L3. So, we concluded that it is not possible to use the presented method to accurately register a single vertebra.

When trying to perform registration using the whole CT-derived PC as reference, we obtained the results in Figure 79 and Figure 82, where it is possible to notice that the alignment between the two point clouds improved substantially, since almost all the points of the US-derived PC were included in the CT-derived. The obtained results are similar to the ones discussed in the sub-subsection 6.3.2.1.

However, and despite the good results obtained when using the complete CT-derived PC to register the L3 vertebrae right US PC, this registration will not consider the relative movement between different vertebrae.

In general, it is possible to conclude that the presented registration methods showed some disadvantages and limitations but can be used to perform a relatively good registration, with Registration Errors in the order of 2 mm . However, we concluded that the presented errors were not completely meaningful, as we would need the quantification of the Target Registration Errors to have a better understanding of the impact of these methods in the proposed surgery.

6.4. Navigation System

Our navigation system was created with the objective of presenting the potential of the developed work. With this navigation system we were able to correctly track the Polaris pointer and visually control its position relative to the lumbar spine and the surgical plans.

The results presented in Figure 84, Figure 85 and Figure 86 allow to see a good match between the position of the Polaris pointer in the navigation system and in the real lumbar spine phantom. This was possible due to the good results presented in the registration step.

There is some error associated with this method, that arises from the accumulation of errors of each individual step, mainly the Pointer Pivoting, the Probe Calibration and the Registration processes. However, using the Navigation System we were not able to numerically quantify the existing error, mainly due to the absence of targets in the lumbar spine phantom that would allow to evaluate TRE, as explained in the previous subsection.

Although we could not present more quantitative results, this system allows to draw some important qualitative conclusions regarding the performed procedure.

7. Conclusion

The goal of the project presented in this Thesis was to simulate an image-guided surgery for inserting pedicle screws in the lumbar spine, using Freehand 3-D Ultrasound imaging as the intraoperative imaging modality and performing registration between the preoperative CT data with the surgical plans and the intraoperative data. Although there was no actual pedicle screw placement, it is possible to affirm that we managed to achieve this goal, since the preoperative and intraoperative work necessary to carry this kind of image-guided procedure was concluded.

Regarding the first objective, the lumbar spine phantom was successfully created. This phantom was constructed based on a real female subject CT-data, with anatomical relevance to the study. Despite the differences it presents to a real human patient, it allowed to perform every stage of the IG procedure.

The second objective was acquiring a CT-scan of the lumbar spine phantom to perform segmentation and the surgical planning. This objective was achieved, since the CT segmentation was correctly performed, resulting in vertebrae models identical to the scanned phantom, and the surgical planning GUI allowed to successfully plan the pedicle screws according to medical orientation.

Regarding the third objective, Freehand 3-D Ultrasound imaging was successfully used to acquire US-volumes of the lumbar spine phantom in the intraoperative referential, after performing probe calibration. Segmentation of this US-data was achieved using a GUI, which enabled the creation of the US-derived point clouds (PC). These PC presented some limitations, mainly due to the US imaging noisy nature and scatter, but in general allowed to identify the most important features of the lumbar spine.

Registration, which was the fourth objective, was performed between the CT-derived (preoperative) and the US-derived (intraoperative) PC, computing the transformations between the CT coordinate system (COS) and the intraoperative COS. Despite the difficulties faced in this step, because of the differences between the preoperative PC and the intraoperative PC, it presented relatively good results, with errors in the order of 2 mm . However, this error is the registration error (RE), which only quantifies the mean distance between the two PC, and the target registration error (TRE), which is measured in specific targets and quantifies the registration error in the surgical procedure, was not evaluated. Also, the registrations performed for a single vertebra presented higher errors than with the full lumbar PC, which leads to the conclusion that this method cannot consider the relative movement between vertebrae.

Finally, the fifth objective was to develop a simple navigation system to visualize in real-time the surgical instruments and the surgical plans. This navigation system was successfully created as a MATLAB® GUI and allowed to view the spine PC, the surgical plans, and the Polaris pointer's real-time position in the intraoperative COS during a procedure. Also, this step made possible to visually verify the good results of the precedent steps. This evaluation was done qualitatively, by comparing the

matching positions of the pointer displayed in the navigation system relative to the CT-data and its positions in reality relative to the lumbar spine phantom.

In general, and despite the limitations in the main steps of this project, which arise mainly from the poor detail of US-data acquired which affect registration, its main goal was achieved. The overall results are optimistic for a laboratory practice, however, for a clinical practice, they lack quantification of the total error associated with registration process, combining RE and TRE. To overcome this aspects, further studies are needed.

7.1. Future work

The methods used in this work can be improved, leading to better results. Although the general structure of the IG surgery should remain the same, each one of its stages may be subjects to further developments. Thus, it is suggested as future work:

- Using a vacuum chamber during the construction of the lumbar spine phantom for removing the air bubbles imprisoned in the silicone and in the gelatine, improving the US images;
- The inclusion of different CT segmentation methods, based on machine learning algorithms, allowing automatic segmentation of each vertebra separately;
- Using a different shape phantom for probe calibration. This new phantom must allow perpendicular intersection with the US frame, while being tracked by the Polaris system, unlike the Polaris pointer;
- Perform the US image segmentation separating each vertebra in a different point cloud, so that each vertebra could be registered individually, overcoming the problem of intervertebral relative movement;
- Using a different method for the initial approximation for the registration, less dependent on the user's skill in identifying matching fiducials. This new initial approximation could be performed by acquiring two intraoperative X-ray images, with some markers. Although it uses ionizing radiation, its exposure dose is much smaller than in an intraoperative CT-scan or fluoroscopy.
- Inclusion of targets in the lumbar spine phantom for computing the target registration error, which makes possible to quantify the full extension of the registration errors.
- Using an orthopedic drill with a Polaris tool attached to perform the surgery for placing the pedicle screws in the lumbar spine phantom. After the surgical procedure, new CT data must be acquired to assess the true surgical errors, by comparing the preoperative CT data and the surgical plans with the postoperative CT data.

References

- [1] T. Vos *et al.*, “Years lived with disability (YLDs) for 1160 sequelae of 289 diseases and injuries 1990–2010: a systematic analysis for the Global Burden of Disease Study 2010,” *Lancet*, vol. 380, no. 9859, pp. 2163–2196, Dec. 2012.
- [2] J. Pelozza, “Surgery for Lower Back Pain.” [Online]. Available: <https://www.spine-health.com/conditions/lower-back-pain/surgery-lower-back-pain>. [Accessed: 13-Mar-2019].
- [3] J. McCormick, M. Aebi, D. Toby, and V. Arlet, “Pedicule screw instrumentation and spinal deformities: have we gone too far?,” *Eur. Spine J.*, vol. 22 Suppl 2, pp. S216-24, Mar. 2013.
- [4] D. Rixen *et al.*, “Image-guided spine surgery: state of the art and future directions,” *Eur. Spine J.*, vol. 19, no. 1, pp. 25–45, 2009.
- [5] T. Ungi, E. Moul, J. H. Schwab, and G. Fichtinger, “Tracked ultrasound snapshots in percutaneous pedicle screw placement navigation: a feasibility study,” *Clin. Orthop. Relat. Res.*, vol. 471, no. 12, pp. 4047–55, Dec. 2013.
- [6] N. Palastanga and R. W. Soames, *Anatomy and Human Movement: Structure and function*, 6th ed. 2011.
- [7] G. J. Tortora and B. Derrickson, *Introduction to the human body : the essentials of anatomy and the physiology*, 9th ed. 2012.
- [8] K. Bridwell, “Ligaments,” 2018. [Online]. Available: <https://www.spineuniverse.com/anatomy/ligaments>. [Accessed: 15-Mar-2019].
- [9] B. Duthey, “Background paper 6.24: low back pain . In: World Health Organisation (WHO) (ed.) Priority medicines for Europe and the world ‘A public health approach to innovation’,” 2013. [Online]. Available: https://www.who.int/medicines/areas/priority_medicines/BP6_24LBP.pdf. [Accessed: 13-Mar-2019].
- [10] D. Hoy *et al.*, “The global burden of low back pain: estimates from the Global Burden of Disease 2010 study,” *Ann. Rheum. Dis.*, vol. 73, no. 6, pp. 968–974, Jun. 2014.
- [11] J. Pelozza, “Causes of Lower Back Pain,” 2017. [Online]. Available: <https://www.spine-health.com/conditions/lower-back-pain/causes-lower-back-pain>. [Accessed: 13-Mar-2019].
- [12] K. Hamilton, “Pulled Back Muscle Treatment,” 2017. [Online]. Available: <https://www.spine-health.com/conditions/lower-back-pain/pulled-back-muscle-treatment>. [Accessed: 13-Mar-2017].
- [13] C. Ray, “Facet Joint Disorders and Back Pain,” 2002. [Online]. Available: <https://www.spine-health.com/conditions/arthritis/facet-joint-disorders-and-back-pain>. [Accessed: 15-Mar-2019].
- [14] J. K. Lang and H. Kolenda, “First appearance and sense of the term ‘spinal column’ in ancient

- Egypt," *J. Neurosurg. Spine*, pp. 152–155, 2009.
- [15] S. G. Marketos and P. Skiadas, "Hippocrates the father of spine surgery," *Spine (Phila. Pa. 1976)*., vol. 24, no. 13, pp. 1381–1387, 1999.
- [16] S. C. Knoeller SM, "Historical perspective: history of spinal surgery," *Spine (Phila Pa 1976)*., vol. Nov 1;25, no. 21, pp. 2838–43, 2000.
- [17] M. Turgut, "Illustrations of neurosurgical techniques in early period of Ottoman Empire by Şerefeddin Sabuncuoğlu," *Acta Neurochir. (Wien)*., vol. 149, no. 10, pp. 1063–1069, 2007.
- [18] H. Oppenheim and F. Krause, "Ueber Einklemmung bzw. Strangulation der Cauda equina," *Dtsch. Medizinische Wochenschrift*, vol. 35, no. 16, pp. 697–700, 1909.
- [19] J. G. LOVE, "PROTRUDED INTERVERTEBRAL DISKS: with a note regarding hypertrophy of ligamenta flava," *J. Am. Med. Assoc.*, vol. 113, no. 23, pp. 2029–2034, Dec. 1939.
- [20] S. Hijikata, M. Yamagishi, T. Nakayama, and K. Oomori, "Percutaneous discectomy: a new treatment method for lumbar disc herniation," *J Toden Hosp*, vol. 39, pp. 5–13, 1975.
- [21] M. G. Yasargil, "Microsurgical Operation of Herniated Lumbar Disc," 1977, pp. 81–81.
- [22] W. Caspar, "A New Surgical Procedure for Lumbar Disc Herniation Causing Less Tissue Damage Through a Microsurgical Approach," 1977, pp. 74–80.
- [23] R. B. Cloward, "The Treatment of Ruptured Lumbar Intervertebral Discs by Vertebral Body Fusion," *J. Neurosurg.*, vol. 10, no. 2, pp. 154–168, Mar. 1953.
- [24] H. H. Mathews, M. T. Evans, H. J. Molligan, and B. H. Long, "Laparoscopic discectomy with anterior lumbar interbody fusion. A preliminary review.," *Spine (Phila. Pa. 1976)*., vol. 20, no. 16, pp. 1797–802, Aug. 1995.
- [25] G. L. Lowery and S. S. Kulkarni, "Posterior percutaneous spine instrumentation," *Eur. Spine J.*, vol. 9, no. S1, pp. S126–S130, 2000.
- [26] K. T. Foley and S. K. Gupta, "Percutaneous pedicle screw fixation of the lumbar spine: preliminary clinical results.," *J. Neurosurg.*, vol. 97, no. 1 Suppl, pp. 7–12, Jul. 2002.
- [27] L. Khoo, "Rationale for minimally invasive spine surgery," in *An anatomic approach to Minimally Invasive Spine Surgery*, M. Perez-Cruet, Ed. St.Louis, Missouri: Quality Medical Publishing Inc., 2006, pp. 89–102.
- [28] L.-P. Nolte, H. Visarius, E. Arm, F. Langlotz, O. Schwarzenbach, and L. Zamorano, "Computer-aided fixation of spinal implants," *J. Image Guid. Surg.*, vol. 1, no. 2, pp. 88–93, 1995.
- [29] N. D. Glossop, R. W. Hu, and J. A. Randle, "Computer-Aided Pedicle Screw Placement Using Frameless Stereotaxis," *Spine (Phila. Pa. 1976)*., vol. 21, no. 17, pp. 2026–2034, Sep. 1996.
- [30] A. L. Carl *et al.*, "In Vitro Simulation. Early results of stereotaxy for pedicle screw placement,"

- Spine (Phila. Pa. 1976)*., vol. 22, no. 10, pp. 1160–1164, May 1997.
- [31] M. Mac Millan, “Computer-Guided Percutaneous Interbody Fixation and Fusion of the L5-S1 Disc,” *J. Spinal Disord. Tech.*, vol. 18, no. Supplement 1, pp. S90–S95, Feb. 2005.
- [32] R. C. Sasso, N. M. Best, and E. A. Potts, “Percutaneous computer-assisted translaminar facet screw: an initial human cadaveric study,” *Spine J.*, vol. 5, no. 5, pp. 515–519, Sep. 2005.
- [33] K. T. Foley, D. A. Simon, and Y. R. Rampersaud, “Virtual Fluoroscopy: Computer-Assisted Fluoroscopic Navigation,” *Spine (Phila. Pa. 1976)*., vol. 26, no. 4, pp. 347–351, Feb. 2001.
- [34] F. L. Acosta, T. L. Thompson, S. Campbell, P. R. Weinstein, and C. P. Ames, “Use of intraoperative isocentric C-arm 3D fluoroscopy for sextant percutaneous pedicle screw placement: case report and review of the literature,” *Spine J.*, vol. 5, no. 3, pp. 339–343, May 2005.
- [35] L. T. Holly and K. T. Foley, “Intraoperative Spinal Navigation,” *Spine (Phila. Pa. 1976)*., vol. 28, no. supplement, pp. S54–S61, Aug. 2003.
- [36] J. L. Laratta, R. A. Lehman, J. M. Lombardi, R. B. Kochanski, and J. E. O’Toole, “Image-Guided Navigation and Robotics in Spine Surgery,” *Neurosurgery*, vol. 0, no. 0, pp. 1–11, 2018.
- [37] X. Lian *et al.*, “Total 3D Airo® Navigation for Minimally Invasive Transforaminal Lumbar Interbody Fusion,” *Biomed Res. Int.*, vol. 2016, pp. 1–8, 2016.
- [38] A. Nooh *et al.*, “Differences between Manufacturers of Computed Tomography-Based Computer-Assisted Surgery Systems Do Exist: A Systematic Literature Review.,” *Glob. spine J.*, vol. 7, no. 1, pp. 83–94, Feb. 2017.
- [39] L. T. Holly, O. Bloch, and J. P. Johnson, “Evaluation of registration techniques for spinal image guidance.,” *J. Neurosurg. Spine*, vol. 4, no. 4, pp. 323–8, Apr. 2006.
- [40] FDA, “Ultrasound Imaging,” 2018. [Online]. Available: <https://www.fda.gov/radiation-emittingproducts/radiationemittingproductsandprocedures/medicalimaging/ucm115357.htm>. [Accessed: 22-Mar-2019].
- [41] M. Ganau, N. Syrmos, A. R. Martin, F. Jiang, and M. G. Fehlings, “Intraoperative ultrasound in spine surgery: history, current applications, future developments.,” *Quant. Imaging Med. Surg.*, vol. 8, no. 3, pp. 261–267, Apr. 2018.
- [42] G. J. Dohrmann and J. M. Rubin, “Intraoperative ultrasound imaging of the spinal cord: syringomyelia, cysts, and tumors--a preliminary report.,” *Surg. Neurol.*, vol. 18, no. 6, pp. 395–9, Dec. 1982.
- [43] A. Fenster, D. B. Downey, and H. N. Cardinal, “Three-dimensional ultrasound imaging.,” *Phys. Med. Biol.*, vol. 46, no. 5, pp. R67-99, May 2001.
- [44] B. Brendel, S. Winter, A. Rick, M. Stockheim, and H. Ermert, “Registration of 3D CT and

- ultrasound datasets of the spine using bone structures.," *Comput. Aided Surg.*, vol. 7, no. 3, pp. 146–55, 2002.
- [45] A. Fedorov *et al.*, "3D Slicer as an image computing platform for the Quantitative Imaging Network.," *Magn. Reson. Imaging*, vol. 30, no. 9, pp. 1323–41, Nov. 2012.
- [46] J. M. Ferreira, "João Filipe Fernandes Mocho Ferreira 78750 Biomedical Engineering Master Thesis." [Online]. Available: http://web.tecnico.ulisboa.pt/ist178750/master_thesis.html.
- [47] NDI Medical, "Polaris Spectra and Vicra." [Online]. Available: <https://www.ndigital.com/medical/products/polaris-family/>. [Accessed: 28-Mar-2019].
- [48] G. Treece, A. Gee, and R. Prager, "Stradwin." [Online]. Available: <http://mi.eng.cam.ac.uk/~rwp/stradwin/docs/intro.htm>. [Accessed: 28-Mar-2019].
- [49] P.-W. Hsu, G. M. Treece, R. W. Prager, N. E. Houghton, and A. H. Gee, "Comparison of Freehand 3-D Ultrasound Calibration Techniques Using a Stylus," *Ultrasound Med. Biol.*, vol. 34, no. 10, pp. 1610–1621, Oct. 2008.
- [50] F. Rousseau, P. Hellier, and C. Barillot, "Confhusius: A robust and fully automatic calibration method for 3D freehand ultrasound," *Med. Image Anal.*, vol. 9, no. 1, pp. 25–38, Feb. 2005.
- [51] A. H. Gee, N. E. Houghton, G. M. Treece, and R. W. Prager, "A mechanical instrument for 3D ultrasound probe calibration," *Ultrasound Med. Biol.*, vol. 31, no. 4, pp. 505–518, Apr. 2005.
- [52] X. Y. Wang, D. M. Wu, and Z. J. Du, "Freehand 3D Ultrasound Calibration Based on Two-Layer Z-Fiducial Phantom," *Adv. Mater. Res.*, vol. 317–319, pp. 638–642, Aug. 2011.
- [53] S. Dandekar, Y. Li, J. Molloy, and J. Hossack, "A phantom with reduced complexity for spatial 3-D ultrasound calibration," *Ultrasound Med. Biol.*, vol. 31, no. 8, pp. 1083–1093, Aug. 2005.
- [54] J. J. Moré, "The Levenberg-Marquardt algorithm: Implementation and theory," in *Numerical Analysis (Lecture Notes in Mathematics)*, Springer-Verlag, 1977, pp. 105–116.
- [55] J. S. Lim, *Two-Dimensional Signal and Image Processing*, vol. 6, no. 2. Englewood Cliffs, NJ: Prentice Hall, 1990.
- [56] E. Schreiber, "Kabsch algorithm - File Exchange - MathWorks." [Online]. Available: <https://www.mathworks.com/matlabcentral/fileexchange/25746-kabsch-algorithm>. [Accessed: 16-Feb-2019].
- [57] W. Kabsch, "A solution for the best rotation to relate two sets of vectors," *Acta Crystallogr. Sect. A*, vol. 32, no. 5, pp. 922–923, Sep. 1976.
- [58] P. J. Besl and N. D. McKay, "A method for registration of 3-D shapes," *IEEE Trans. Pattern Anal. Mach. Intell.*, vol. 14, no. 2, pp. 239–256, Feb. 1992.

8. Appendix

8.1. Appendix A - Gelatine recipe

The gelatine used in the lumbar spine phantom was prepared as follows:

- Bring 3 L of water to a boil;
- After boiling, turn off the heat and let it rest for 1 minute;
- Gradually add and dilute 420gr of neutral gelatin to the water, stirring constantly;
- Gradually add and dilute 1.6L of glycerin to the resulting solution by stirring constantly;
- Add the gelatine solution to the box with the lumbar spine model fixed in the bottom;
- Gently shake the box to release the imprisoned air bubbles;
- Leave the set in the refrigerator overnight to solidify the gelatine.

8.2. Appendix B - ICP RMSE

The ICP RMSE is computed as the Root Mean Square (RMS) of the distance between each point of the transformed US-derived PC and its closest point of the CT-derived PC used as reference. The ICP algorithm calculated this Registration Error for each iteration, which are presented in the following tables.

8.2.1. Full lumbar spine – medial

Table 9 - RMSE for each ICP iteration in the registration between the full lumbar spine - medial PC and the CT-derived PC.

ICP iteration	RMSE (mm)	ICP iteration	RMSE (mm)
0	2,82743851127136	8	2,21418426804041
1	2,58184941352612	9	2,21167235913722
2	2,36135519840462	10	2,20998248461347
3	2,28239096276451	11	2,20880317209472
4	2,24934040715461	12	2,20799131341806
5	2,23303482843563	13	2,20742054976898
6	2,22372835346715	14	2,20702233718296
7	2,21793228398489	15	2,20674234244310

8.2.2. Full lumbar spine – left

Table 10 - RMSE for each ICP iteration in the registration between the full lumbar spine - left PC and the CT-derived PC.

ICP iteration	RMSE (mm)	ICP iteration	RMSE (mm)
0	2,78678253393487	8	2,00653674245046
1	2,37295732871221	9	2,00200701661391
2	2,11374187245028	10	1,99821543966622
3	2,05864518695353	11	1,99500581684033
4	2,03894209259450	12	1,99230721217521
5	2,02742650103699	13	1,99005284135063
6	2,01886441412745	14	1,98820369649356
7	2,01204309966560	15	1,98668092089090

8.2.3. Full lumbar spine – right

Table 11 - RMSE for each ICP iteration in the registration between the full lumbar spine - right PC and the CT-derived PC.

ICP iteration	RMSE (mm)		
0	2,13925989345241	8	1,91763761341740
1	2,00512463974132	9	1,91760911621935
2	1,93121219703791	10	1,91758604876406
3	1,92023683943225	11	1,91756766265453
4	1,91833318291874	12	1,91755624598769
5	1,91789811873664	13	1,91754878800835
6	1,91775033900842	14	1,91754393161079
7	1,91767999590319	15	1,91754021145447

8.2.4.L3 vertebra – right (1st)

Table 12 - RMSE for each ICP iteration in the registration between the L3 vertebra – right (1st) PC and the CT-derived L3 PC.

ICP iteration	RMSE (mm)	ICP iteration	RMSE (mm)
0	5,92022702573025	8	5,29094658691625
1	5,69575250620359	9	5,28916782965510
2	5,47724369669526	10	5,28817504025767
3	5,38233598174361	11	5,28762504360121
4	5,33425916504909	12	5,28729964592004
5	5,31039501556061	13	5,28711359773477
6	5,29970010905514	14	5,28701566827529
7	5,29409870451007	15	5,28695768534091

Table 13 - RMSE for each ICP iteration in the registration between the L3 vertebra – right (1st) PC and the complete CT-derived PC.

ICP iteration	RMSE (mm)	ICP iteration	RMSE (mm)
0	3,07248506464179	8	2,53608108667523
1	2,86814615743684	9	2,53288506556884
2	2,67949944729515	10	2,53089660427979
3	2,61163622455375	11	2,52971445564776
4	2,57701050788252	12	2,52897632062990
5	2,55769001390825	13	2,52846214171460
6	2,54709633554549	14	2,52810905863765
7	2,54080843528426	15	2,52787252874159

8.2.5.L3 vertebra – right (2nd)

Table 14 - RMSE for each ICP iteration in the registration between the L3 vertebra – right (2nd) PC and the CT-derived L3 PC.

ICP iteration	RMSE (mm)	ICP iteration	RMSE (mm)
0	5,53452796854001	8	4,92514267047569
1	5,33937781608137	9	4,92153945376544
2	5,13538122564809	10	4,91912902940906
3	5,04503601120254	11	4,91755319649889
4	4,99528335152826	12	4,91649040166059
5	4,96278972584268	13	4,91581175577991
6	4,94291546295772	14	4,91537311751718
7	4,93140064751142	15	4,91509062249693

Table 15 - RMSE for each ICP iteration in the registration between the L3 vertebra – right (2nd) PC and the complete CT-derived PC.

ICP iteration	RMSE (mm)	ICP iteration	RMSE (mm)
0	2,75049944372063	8	2,62278736231143
1	2,73241224281798	9	2,62091524664899
2	2,70013211706746	10	2,61976390444004
3	2,67288624318447	11	2,61898497459041
4	2,65171588300904	12	2,61845366286858
5	2,63800518063410	13	2,61808464458054
6	2,63032037406211	14	2,61779657665410
7	2,62567627259717	15	2,61754455358825